POLITECNICO
MILANO 1863

SCUOLA DI INGEGNERIA INDUSTRIALE
E DELL'INFORMAZIONE

Executive Summary of the Thesis

Attitude Estimation of Space Objects from Combined Multispectral Measurements

Laurea Magistrale in Space Engineering - Ingegneria spaziale

Author: Sergio Bonaccorsi

Advisor: Prof. Pierluigi Di Lizia

Co-advisors: Prof. Mauro Massari, Javier Carro, Ivan Llamas

Academic year: 2020-2021

1. Introduction and Context

In the context of Space Situational Awareness (SSA), knowledge of the trajectory and attitude of a Space Object (SO) is critical to ensure the safety of current and future space missions. This information about the state of an SO is retrieved through measurements acquired from ground-based instruments, which are processed using specific estimation algorithms.
Generally, the instruments used for this purpose are radar, laser, and optical telescopes. This work focuses on the estimation of attitude variables and the material properties of an observed target starting from measurements acquired through a ground-based sensor. In particular, the main interest is to analyse the potential of sensors working in wavelength bands different from the visible one, i.e. the infrared band.
The infrared radiation emitted by a body carries specific information about its materials, its recent history, and its configuration [1]. The different working wavelength bands of some sensors leads to an important consideration about the nature of the measured radiation coming from the observed target. In fact, the closer is the wavelength working region of the sensor to the visible band, the higher is the contribution of the reflected component of the incoming radiation compared to the emitted one. Moving towards longer wavelengths, this last component becomes more and more important for SO in the LEO region due to their typical temperature values that is around 300 K. At these values, the magnitude of the radiation coming from the sun, that is reflected by the object, is negligible compared to the emitted one. This statement is a consequence of simple calculations performed thanks to the Planck law, which relates the radiation emitted by a body to its temperature and a specific wavelength range of interest.
This difference generates advantages and disadvantages that can be investigated to understand the potential of this class of instruments in dealing with the above-mentioned problems. The most important constraint to underline regarding the optical telescopes is the dependence of the measurement process on the illumination condition of the target. An infrared-based system could grant the acquisition of measurements even in unfavourable illumination conditions, as in the eclipse phase, thus mitigating this optical telescopes' disadvantage. Among the disadvantages, it has to be verified if the infrared measurements are still able to carry the same kind

of information as the typical light curves, because of the sensitivity to a different component of the incoming radiation. In addition, infrared wavelengths could be strongly affected by smoke, dust, fog, sunlight, and therefore the atmosphere would play an important role.
The current knowledge about light curves, a measure of the light reflected by a target towards an observer, and the methods to apply for extracting the information of interest is a very relevant topic nowadays. They can be used to estimate attributes of SOs as the spacecraft's attitude state. Traditional estimation methods such as Kalman filtering have been used to estimate attitude from light curve measurements [5]. However, such an approach requires knowledge of the object's shape, as well as an assumed reflectance model. This is necessary for attitude observability [2]. In reality, the shape of the object may not be known. Simultaneous shape and attitude estimation has been demonstrated using filtering methods, but such methods require assumptions about the model. If these assumptions do not describe the actual system, such methods are unlikely to perform well. Additionally, in some cases, light curves may not provide sufficient information to enable precise attitude determination using these methods. Therefore, there is a desire to employ non-model-based methods in determining attitude information from light curves.
This knowledge related to light curves can be exploited to investigate the potential of the use of measurements acquired in the infrared band. There are a lot of similarities that one can use as a starting point to perform the same kind of analyses and retrieve an attitude estimate of interest.

2. Overview and Objective

The first goal of this work is to simulate a measure acquired by a ground-based instrument working in a selected wavelength band that points an SO in the LEO region, and then to investigate the potential of an observation strategy that uses these measurements to recover information about the satellite state.
To pursue this goal, many aspects have to be considered and a precise procedure has to be followed, as shown in the diagram in Figure 1. In blue rounded blocks there are the variables of the problem that the user can set at the beginning of the simulations, while the tools and the models used to calculate the quantities of interest are represented by the red circles.
The first blue block is the orbit in which the target is placed, which has to be provided in the Two Line Elements (TLE) form. The observation point has to be described in terms of latitude, longitude and altitude, together with some important visibility constraints concerning the limiting azimuth and elevation. The geometry of the observed target has to be defined to know some fundamental characteristics like the inertia tensor, the size of the different surfaces and their orientation in a body-fixed reference frame. Then, the attitude motion of the object has to be described in terms of initial conditions of the angular velocity and quaternions, together with the external moments that could affect the dynamics of the target. Lastly, the sensor model will be used to derive the simulated signal-to-noise ratio based on specific characteristics.
For what concerns the red blocks, the first calculated quantities are position and velocity of an object in the specified orbit and the relative configuration with respect to one or more observation points on the surface of the earth. This operations are performed by the Virtual Observatory (VO), which is an advanced tool developed for precise simulations of ground-based measurements. Then, the simulation of the measured incoming radiation of a satellite needs the combination of a Thermal Model (TM) and a Radiometric Model (RM). The first performs a thermal analysis of an object orbiting around the Earth, so that its temperature evolution over time can be predicted. This is done thanks to the SO state coming from the VO and the information about the geometry and the attitude of the target. Once this information is available, the radiometric equations are used to calculate the SNR and therefore simulate the acquisition of a measure from a ground-based station, taking into account the characteristic of the specified sensor.
Then, mathematical tools are applied in order to exploit the available information contained in the simulated measurements and try to recover an estimate of the attitude variables, i.e. the satellite angular velocity vector and the Euler angles (or the quaternion). To do this, a

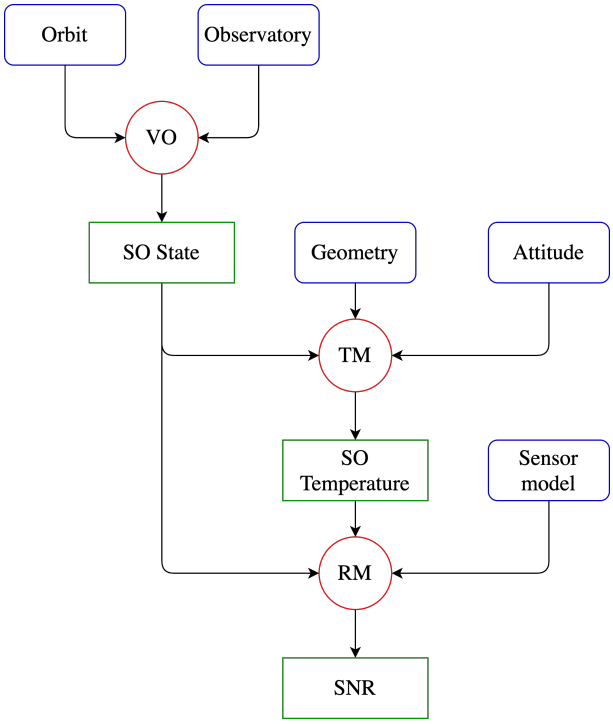

Figure 1: Flow diagram

good match between the measured and estimated curves will be sought. In particular, the non-linear least-squares (LS) method and the MATLAB MultiStart algorithm will be used. The LS method will make use of an initial guess that will be refined in order to find the best fit with the provided measurements. The second method will be exploited to recreate a more realistic situation in which a valid initial guess cannot be found and therefore a large number of possible initial solutions are used as a start point for an optimization algorithm that will try to minimize the difference between the measured curve and the estimated one.

2.1. Problem Statement

For the simulations performed in this work, the sun-synchronous orbit of Soil Moisture and Ocean Salinity (SMOS) and the orbit that experiences an eclipse region of the International Space Station (ISS) have been selected.
The geometry defined are a cubic microsatellite and a 3U CubeSat. For both, the body-mounted configuration and the one with two deployable solar panels can be simulated. Therefore, a six-faces geometry will be considered in the first case and a ten-faces for the second (the six of the main body plus two for each solar panel). Given this geometry, a 3-nodes thermal model is used for describing the main body plus the two solar panels, which will be considered to have the same temperature. Each surface of the satellite will be covered by material whose thermo-optical properties have been selected starting from the description in [4].
Three different attitude motion will be defined in order to simulate different conditions of an observed SO: an earth-pointing (EP), a sun-pointing (SP) and a tumbling motion (T). The target characterized by these types of motion will be observed by three different observatories and with three different sensors that works in different wavelength bands. In this way, a complete picture of an observation strategy can be given and interesting comparison can be made.

3. Thermal Model

The aim is to develop a reliable and simplified thermal model such that all the most important constraints are considered and that a quite accurate temperature profile over the simulation time can be found.
Satellite thermal analysis is concerned with predicting the temperature of a satellite in a known or assumed heating environment [3]. The first step is therefore to know which are the main

heat fluxes present in the space environment and to model them reliably. For the relevant targets of this work, three main heat fluxes affect the satellite surfaces: solar radiation, earth flux and earth albedo.
The mathematical model underlying this analysis is the heat equation. For the main body and for each solar panel one can refers to (1), where the variables has to be selected according to the considered thermal node. An effective area can be recovered to consider the different thermo-optical properties of the N different surfaces as in equation (2).

$$C\frac{dT(t)}{dt} = -A_{eff}\,\sigma\,T(t)^4 + Q_{tot}(t) + Q_{int} \quad (1)$$

$$A_{eff} = \sum_{n=1}^{N} A_i\,\varepsilon_i \quad (2)$$

The problem just described is solved taking into account that, without external perturbations, all the variables that affect the computation of the satellite temperature are supposed to be very similar at the beginning and at the end of an orbital period. For this reason, a cyclic transient model is used. To mathematically enforce the cyclic condition, two criteria have to be respected: the temperatures and the temperature slopes at the end and beginning of the orbit must be the same.
As an example of the behavior of this variable, here are reported the temperature evolution of both the main body and a solar panel of a target in tumbling motion placed on the ISS orbit. The dashed red lines denote the beginning and the end of the eclipse phase.

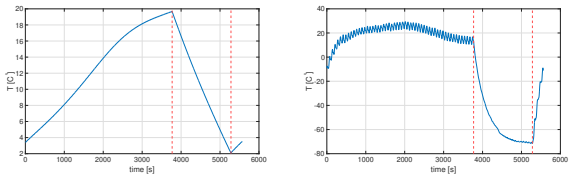

(a) T_{body} ISS (b) T_{panel} ISS

Figure 2: Temperature profiles

4. Radiometric Model

The ensemble of phenomena that accompany the emission of radiation by a source, the environment in which it is found, the medium through which the radiation propagates, until it is absorbed by a detector, is called the radiometric chain [1].
The radiometric equations here presented will be used to quantify the magnitude of radiation that reaches the sensor. This incoming electromagnetic radiation will be composed by a reflected component generated by the radiation coming from the sun and by an emitted component given by the temperature of the observed target that is higher than 0 K. At the end of the calculations, the quantity of interest will be the signal-to-noise ratio (SNR), which will be defined in two different ways depending on the nature of the sensor.
The radiance emitted by the target is given by Planck's law integrated over a specified spectral range, which can be identified once the spectral band of the detector is selected. The radiant flux is then calculated by considering other coefficient such as the area of the pupil S_p, the effective area of the target seen by the sensor S_t, and the square of the distance between the target and the detector d^2 that is put at the denominator.
The radiation coming from the sun is then reflected by the object towards the observer when the relative configuration between these three actors is favorable. It is always calculated through the Planck law by using the temperature of the sun and a scaling factor given by the square of the ratio between the radius of the sun and the distance from the sun to the earth. Then, the other coefficients, earlier described for the emitted component, are also used to calculate this component.
In this process, many other sources give their contribution to the measured flux, like the atmospheric emission and reflections and the background radiation, which is the contribution of the ambient around the object. For this reason, the presence of external noise has to be considered in the quantity registered by the instrument.

4.1. Sensors

Based on the working principle of the sensor, detectors can be split into two broad categories. These are the photodetectors and thermal detectors. The main difference in the operational principle of photodetectors and thermal detec-

tors is given by the Focal Plane Array (FPA) sensitive part. In the case of photodetectors, the sensitive part converts an incoming signal of photons into a current of electrons, to be later processed in the electronic module. On the other hand, the FPA of thermal detectors reacts changing its temperature when it enters in contact with a flux of infrared radiation, therefore they do not convert the incoming flux of photons into electrons, as in the case of photodetectors. Then, these changes in temperature will be measured in a different way depending on the type of thermal detector.
For the purposes of this work, three instruments working in different wavelength ranges will be considered. They will be used as a reference to simulate an acquired measurement to then make a comparison of their performances based on their SNR.

4.2. Signal-to-Noise Ratio

A commonly used quantity in the context of astronomic observations is the signal-to-noise ratio, which is a measure that compares the level of a desired signal to the level of noise. SNR is defined as the ratio of signal power P_s to the noise power P_n, often expressed in decibels.
In the case of photodetectors, the incoming photon flux is the quantity to use for the definition of the SNR. In fact, successful detection of an SO typically requires the number of photons emitted by the SO to be several times greater than the number of photons emitted by noise sources. Among the sources of noise the are the photon flux coming from the background, the dark current and the readout noise. Finally the SNR for a photodetectors is given by equation (3), where G is the multiplicative gain of the instrument, F is the excess noise factor, whose value has been set to $\sqrt{2}$, and q_{SO} is the sum of $q_{SO,ref}$ and $q_{SO,em}$.

$$SNR = \frac{G\, q_{SO}}{\sqrt{F^2\, G\, (q_{SO} + q_{sky} + q_{DC}) + \sigma_{RO}^2}} \tag{3}$$

For thermal detectors the SNR is defined as the ratio between the power of the incoming signal in Watt, multiplied by a responsivity R (defined as the output voltage/current per unit of received power in [A/W] or [V/W]), and the noise voltage. The ratio of the responsivity by the noise voltage is equivalent to the detectivity D. Therefore the SNR can be also calculated with equation (4).

$$SNR = P\, D \tag{4}$$

5. Estimation Strategies

To understand the potential of this observation strategy, the acquired data are used to estimate the attitude variables and the thermo-optical properties of the observed object. The non-linear least-squares method (LS) and the Multi-Start algorithm (MS) implemented in MATLAB have been used for this purpose. Satellite position and velocity are considered as known variables of the problem, even if affected by uncertainties compared to their actual values, while the unknowns are the attitude variables, i.e. the angular velocity and the Euler angles, the emissivity and reflectivity of the materials and a temperature for each thermal node considered constant for the observation time.
The independent variable that will be optimized to find the best fit with the provided measurements is the composition of a six-element vector containing the initial conditions of the six attitude variables, together with 2 temperatures for the two thermal nodes for each observation time considered, the 8 emissivity values and the 8 reflectivity values (6 faces of the main body plus 2 faces of one solar panel). The terms "initial" refers to the first time instant of the first observation.
Three observatories were placed such that the target was visible from all of them during one orbital period. Then, two strategies have been tested. The first involves the use of multiple observation sites (MO) in order to combine the information coming from different time intervals. The second uses of a single observation point where all the three instruments have been placed (MI) in order to combine measurements coming from sensors that work in different wavelength bands. For each strategy there will be a comparison with the case of a single observatory that uses a single instrument (SO/SI). These applications have been tested to try to drive the algorithm towards a more precise solution.
An example of the results obtained through the

different techniques is reported in the following. In the caption, it is written the strategy that has been followed and in brackets there is the reference to the method exploited.

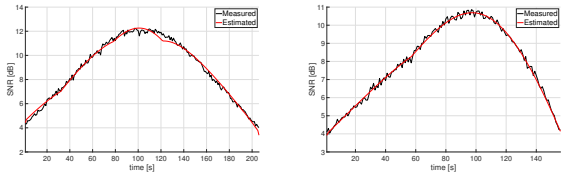

(a) SO - EP (LS) (b) MO - SP (LS)

Figure 3: Matching with measured data

Satisfying results for the EP and SP cases were obtained through the LS method, especially with the MO and MI applications, thanks to an accurate initial solution used as a first guess for the algorithm. The LS routine was able to refine it providing good estimates of the unknowns. In the tumbling case, a precise initial solution was not available and so the MS procedure, able to run in parallel optimization algorithms using a large number of different starting points, was exploited to better explore the solution space and find a valid solution.

6. Conclusion and Future Work

A great interest in infrared sensors has been developing in recent years for their advantages and the information contained in the measurements they acquire. Thanks to the VO tool and the TM and RM models developed in this work, simulations of the SNR of three different sensors working in different wavelength bands have been possible. This first step allowed to perform a comparison of the detectability performances and then to move to estimation procedures to recover the attitude of the target and its thermo-optical properties.

This work analysed two ground-based observation strategies that showed the potential of the combination of different measurements. Data acquired from multiple observation sites, as well as data acquired from multiple instruments placed in the same observatory, have been exploited to drive the applied methods towards more precise solutions.

It has been shown that thermal detectors still have lower performance in therms of detectability compared to photodetectors, but they are projected to be real competitors in the near future. In addition, they can be used to detect targets also in unfavorable illumination conditions due to their sensitivity to the emitted component of radiation.

The search of a matching with the simulated measurements to retrieve some variables of interest have shown the presence of comparable local minima. This means that certain combinations of these variables allow to obtain curves with similar shape thus resulting in an incorrect estimate of the target's attitude.

For future developments, one can combine these measurements with the ones acquired by radar and laser to increase the data for a post-processing phase involving some estimation techniques. The interest of combining measurements is increasing in the last years for the advantage of disposing of a larger number of data that could lead to more precise results. On the other hand, one has to consider the difficulties related to a practical application of such a strategy, since there is the need to link different facilities or different instruments for the same goal.

References

[1] Gilbert Gaussorgues and Seweryn Chomet. *Infrared thermography*, volume 5. Springer Science & Business Media, 1993.

[2] Joanna C Hinks, Richard Linares, and John L Crassidis. Attitude observability from light curve measurements. In *AIAA Guidance, Navigation, and Control (GNC) Conference*, page 5005, 2013.

[3] Robert Karam. *Satellite thermal control for systems engineers*. American Institute of Aeronautics and Astronautics, 1998.

[4] Anthony Kellens. *Thermal design of the OUFTI-Next mission*. PhD thesis, MA thesis. University of Liege, 2018.

[5] Charles J Wetterer and Moriba Jah. Attitude determination from light curves. *Journal of Guidance, Control, and Dynamics*, 32(5):1648–1651, 2009.

POLITECNICO
MILANO 1863

SCUOLA DI INGEGNERIA INDUSTRIALE
E DELL'INFORMAZIONE

Attitude Estimation of Space Objects from Combined Multispectral Measurements

Tesi di Laurea Magistrale in
Space Engineering - Ingegneria Spaziale

Author: **Sergio Bonaccorsi**

Student ID: 928145
Advisor: Prof. Pierluigi Di Lizia
Co-advisors: Prof. Mauro Massari, Javier Carro, Ivan Llamas
Academic Year: 2020-21

Abstract

In the context of space surveillance and tracking, determining the attitude of a target observed from a ground station is a critical step. This work focuses on the estimation of attitude variables and material properties of a space object starting from measurements acquired by ground-based sensors working in different wavelength bands. The closer the working region of the sensor wavelength is to the visible band, the greater the contribution of the reflected component of the incoming radiation compared to the emitted one. Moving towards infrared wavelengths, the latter component becomes more and more important for space objects in the LEO region due to their typical temperature values around 300 K.

The first part of this research is devoted to the generation of simulated measurements through the use of a tool called Virtual Observatory and a thermal and radiometric model. These are used to retrieve the state and the temperature of a space object together with relative geometry considerations with respect to an observer on the earth's surface. Then, the signal-to-noise ratio defined specifically for a photodetector and a thermal detector is calculated for performance comparison.

The simulated measurements are then exploited to use the non-linear least-squares method and the MATLAB MultiStart algorithm to get an estimate of the variables of interest. For this, two observation strategies are analysed that showed the potential of combining several measurements. Data acquired from multiple observation sites, as well as data acquired from multiple instruments located in the same observatory, were exploited to guide the applied methods towards more precise solutions.

Satisfactory results were obtained through the least squares method when an accurate first guess was given to the algorithm. When the latter was not available, the MultiStart procedure, capable of running optimisation algorithms in parallel using a large number of different starting points, was exploited to better explore the solution space and find a valid solution.

Keywords: Space Surveillance, Infrared Remote Sensing, Measurement Simulation, At-

titude Estimation

Abstract in lingua italiana

Nell'ambito della sorveglianza spaziale, determinare l'assetto di un corpo osservato da una stazione di terra è un aspetto critico. Questo lavoro si concentra sulla stima delle variabili di assetto e delle proprietà materiali di un oggetto spaziale a partire da misure acquisite da sensori che lavorano in diverse bande di lunghezza d'onda. Più la banda di lunghezza d'onda del sensore è vicina a quella del visibile, maggiore è il contributo della componente riflessa della radiazione in entrata rispetto a quella emessa. Spostandosi verso il regime infrarosso, quest'ultima componente diventa sempre più importante per gli oggetti in orbite LEO a causa dei loro tipici valori di temperatura intorno ai 300 K.

La prima parte di questa ricerca è dedicata alla generazione di misure simulate attraverso l'uso di uno strumento chiamato Virtual Observatory e un modello termico e radiometrico. Questi vengono utilizzati per recuperare lo stato e la temperatura di un oggetto spaziale insieme a considerazioni sulla geometria relativa rispetto a un osservatore sulla superficie terrestre. In seguito, il rapporto segnale-rumore definito specificamente per un photodetector e un thermal detector sono calcolati per un confronto delle prestazioni.

Le misure simulate sono poi sfruttate tramite il metodo dei minimi quadrati non lineari e l'algoritmo MultiStart di MATLAB per ottenere una stima delle variabili di interesse. Per questo, vengono analizzate due strategie di osservazione che hanno permesso di mettere in evidenza il potenziale della combinazione di diverse misurazioni. I dati acquisiti da più siti di osservazione, così come i dati acquisiti da più strumenti situati nello stesso osservatorio, sono stati sfruttati per guidare i metodi applicati verso soluzioni più precise.

Risultati soddisfacenti sono stati ottenuti con il metodo dei minimi quadrati quando una prima ipotesi accurata è stata data all'algoritmo. Quando quest'ultima non era disponibile, la procedura MultiStart, capace di eseguire algoritmi di ottimizzazione in parallelo usando un gran numero di punti di partenza diversi, è stata sfruttata per esplorare meglio lo spazio delle soluzioni e trovare una stima valida.

Parole chiave: Sorveglianza Spaziale, Infrared Remote Sensing, Simulazione di Misure, Stima d'assetto

Contents

1 | Introduction

1.1. Context of the Internship

This work has been developed during an internship period at GMV Innovating Solutions, in the Toulouse office. GMV was born in 1984 and was centered on the space and defense sectors, taking its initial steps in fields like mission analysis, flight dynamics, control centers, simulation or earth-observation and satellite-navigation. Starting out as a small group of engineers who won a contract from ESA's European Space Operations Centre (ESOC) in an open international tender, GMV then went from strength to strength, quickly growing into a solid firm running a 100-strong staff by the late eighties. It played a key role in ESA's first space missions and defense programs and provided highly specialized services for the major international satellite manufacturers and operators.

The work carried out is related to the activities of the FUSMEAS group of GMV that is in charge of analysing the potential of combining measurements acquired by different instruments in order to improve the quality of the orbit and attitude determination and, therefore, improve the knowledge of the space environment. In particular, the FUSMEAS group already had a deep knowledge of the advantages of radar, laser and optical telescopes. They were already at a very advanced point for what concerns the simulations of measurements taken from these instruments and the possible analysis to perform to estimate the roto-translational state of the observed object. For this reason, they have shown an interest in exploring another family of instrument, the infrared one, in order to increase the knowledge of the possible means available today for ground-based observations. The goal was therefore to reconstruct the context of thermal remote sensing, the physical principles at the basis of the working principle of these sensors and then to develop models in order to simulate the infrared signature of a specific target.

1.2. Space Situational Awareness

The exploitation of space over the last fifty years has led to an increase in the population of both space debris and operational satellites orbiting around the Earth. Space Situational

Awareness (SSA) refers to the knowledge of the space environment, including location and function of space objects and space weather phenomena. SSA is generally understood as covering three main areas [30]:

- Space Surveillance and Tracking (SST) of man-made objects.
- Space WEather (SWE) monitoring and forecast.
- Near-Earth Objects (NEO) monitoring (only natural space objects).

In this context, the Space Situational Awareness Programme, founded by the European Space Agency (ESA), is an initiative designed to support Europe's independent space access and utilization through the timely and accurate information delivery regarding the space environment, and particularly hazards to both in orbit and ground infrastructure [41]. This initiative of the ESA has the objective of providing Europe with complete and accurate information on objects orbiting the Earth, on the space environment and on threats coming from space. It also aims at protecting the safety and security of European economies, societies and citizens, which rely on space-based applications such as communication, navigation and Earth observation.

This work is focused on the SST segment, which refers to the capacity to detect, catalogue and predict the movements of Space Objects (SOs) orbiting the Earth. To improve Space Surveillance, and thus avoid dangerous collisions, this great amount of SOs must in fact be classified. In particular, the knowledge of the trajectory and the attitude of a Resident Space Object (RSO) is fundamental to ensure the safety of current and future space missions. RSO acquisition, tracking, and data collection can be extremely challenging due to many factors. The SST relies on a series of radar and optical instruments on ground to perform these operations. Some of these are mainly devoted to surveillance, while others serve the tracking portion.

1.3. Context of Infrared Measurements

In the context of SSA, the knowledge of the attitude state of satellites is of interest for many purposes. One could be interested to know if a spacecraft is still in an acceptable configuration concerning the mission's requirements or to know if a specific target is changing its state to fulfill a different task, like pointing to a different region on the Earth's surface. Detecting changes in rotational states is useful for detecting anomalies and potential activities of an SO. Determining the attitude of an SO is an area of interest in SSA. Many techniques have been developed to recover this information and they all start from the knowledge of some data. In particular, ground-based facilities are nowadays

exploited to get measurements that can be later used for identifying the state of the observed RSO. Generally, the instruments used for this purpose are radar, laser, and optical telescopes. They provide different information through the measure of different quantities related to the pointed RSO. Low Earth Orbit (LEO) tracking is generally operated by military radars which present different problems such as high costs, private facilities, confidentiality of the data and low precision in initial orbit determination due to raw angular measures. Optical sensors can be used to monitor other orbital regions as the geostationary (GEO) that is too far for radar observation. Using these instruments for the LEO region is not an easy task due to the high angular speed of the objects and the illumination constraints (the RSO must be illuminated and the ground station must not be illuminated). Another family of instruments that can be exploited in this context is composed by the sensors working in the infrared part of the wavelength spectrum. This means that this kind of detectors present some components that are able to filter the incident electromagnetic radiation within the infrared band. The infrared radiation emitted by a body carries specific information about its materials, its recent thermal history, and its configuration [7]. An infrared sensor is therefore capable of extracting information starting from the infrared flux emitted by the RSO that could be then used to solve the problem described above.

The parallelism between the latter two instruments, the optical and infrared telescope, is of great interest for the purpose of this work. An infrared system has a very similar working principle of an optical system, taking an image with an instrument that is sensitive to different wavelengths. This small difference generates a variety of advantages and disadvantages that can be investigated to understand the potential of this class of instrument, which could be then included among the instruments used today for the above-mentioned purposes.

In particular, optical telescopes are used to acquire the so-called light curves, which represent the evolution of the intensity of the reflected light of an SO. An infrared instrument would not record the same type of measurement, but it is able to acquire the time evolution of the emitted component of the radiation coming from the observed target. In other words, they both acquire the history of a quantity but the physical principles at the basis of the processes are different. The current knowledge about light curves and the method to apply for extracting the information of interest is a very relevant topic nowadays. Light curves can be used to estimate attributes of RSOs. One such attribute of interest is the spacecraft's attitude state. Traditional estimation methods such as Kalman Filtering have been used to estimate attitude from light curve measurements [38]. However, such an approach requires knowledge of the object's shape, as well as an assumed reflectance model.

This is necessary for attitude observability [11]. In reality, the shape of the object may not be known. Simultaneous shape and attitude estimation has been demonstrated using filtering methods [39], but such methods require assumptions about the model. If these assumptions do not describe the actual system, such methods are unlikely to perform well. Additionally, in some cases, light curves may not provide sufficient information to enable precise attitude determination using these methods [5]. Therefore, there is a desire to employ non-model-based methods in determining attitude information from light curves. The light curve is well-suited to determining the rotation rate of the spacecraft, as such rotation produces a periodic light curve. All this information related to the measurements acquired by an optical telescope can be exploited to investigate the potential of the use measurements acquired in the infrared region. There are a lot of similarities that one can use as a starting point to perform the same kind of analyses and retrieve the knowledge of interest.

The use of an optical or an infrared telescope has some advantages and disadvantages. Among them, the most important constraint to underline regarding the optical telescopes is the dependence of the measurement process on the illumination condition of the target. An infrared-based system could grant the acquisition of measurements even in unfavourable illumination conditions, thus mitigating this optical telescopes' disadvantage. Another interesting point is the possibility of acquiring measurements during the eclipse phase of the target, even if it is fundamental to well understand the constraints acting in that condition.

Among the disadvantages, it has to be verified if the infrared measurements are still able to carry the same kind of information as the typical light curves, since the two sensors are sensitive to a different component of the incoming radiation. In fact, the closer is the wavelength working band of the sensor to the visible one, the higher is the importance of the reflected component of the incoming radiation compared to the emitted one. This is given by the typical temperature values of an RSO in the LEO region, which is related to the magnitude of the emitted radiation by the Planck law. These notions will be later detailed.

In addition, infrared wavelengths are affected by smoke, dust, fog, sunlight, and therefore the atmosphere would play an important role, as explained later. Finally, this technology cannot distinguish between objects that are near to or obscuring each other when they are of similar heats.

1.4. Overview and Objective

The first goal of this work is to simulate a measurement acquired by a ground-based instrument working in a selected wavelength band that points an RSO in the LEO region, and then to investigate the potential of an observation strategy that uses these measurements to recover information about the satellite state. In general, when the attitude determination of satellites is studied, the following three main parts need to be addressed: attitude representation, acquisition of measurements and estimation algorithms.

To pursue this goal, many aspects have to be considered and a precise procedure has to be followed, as shown in the diagram in Figure 1.1. In blue rounded blocks there are the variables of the problem that the user can set at the beginning of the simulations, while the tools and the models used to calculate the quantities of interest are represented by the red circles.

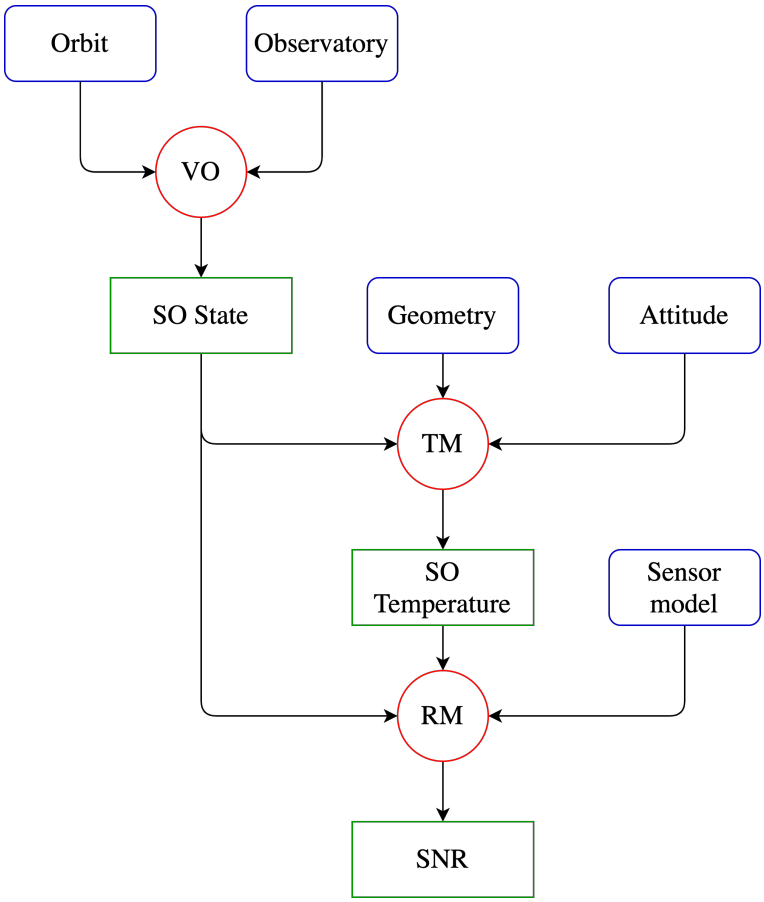

Figure 1.1: Flow diagram

The first blue block is the orbit in which the target is placed, which has to be provided in the Two Line Elements (TLE) form. The observation point has to be decribed in terms

of latitude, longitude and altitude, together with some important visibility constraints concerning the limiting azimuth and elevation. The geometry of the observed target has to be defined to know some fundamental characteristics like the inertia tensor, the size of the different surfaces and their orientation in a body-fixed reference frame. Then, the attitude motion of the object has to be described in terms of initial conditions of the angular velocity and quaternions, together with the external moments that could affect the dynamics of the target. Lastly, the sensor model will be used to derive the simulated signal-to-noise ratio based on specific characteristics.

For what concerns the red blocks, the first calculated quantities are position and velocity of an object in the specified orbit and the relative configuration with respect to one or more observation points on the surface of the earth. This operations are performed by the Virtual Observatory (VO), which will be described more in detail in a later section, being that it is an advanced tool developed for precise simulations of ground-based measurements. Then, the simulation of the measured incoming radiation of a satellite needs the combination of a Thermal Model (TM) and a Radiometric Model (RM). The first step is therefore to perform a thermal analysis of an object orbiting around the Earth, as detailed in Chapter 4, so that its temperature evolution over time can be predicted. This is done thanks to the SO state coming from the VO and the information about the geometry and the attitude of the target. Once this information is available, thanks to the considerations explained in Chapter 3, the radiometric equations are used to calculate the SNR and therefore simulate the acquisition of a measure from a ground-based station, taking into account the characteristic of the specified sensor.

Then, mathematical tools are applied in order to exploit the available information contained in the simulated measurements and try to recover an estimate of the attitude variables, i.e. the satellite angular velocity vector and the Euler angles (or the quaternion). To do this, a good match between the measured and estimated curves will be sought. In particular, the non-linear least-squares (LS) method and the MATLAB MultiStart algorithm will be used. The LS method will make use of an initial guess that will be refined in order to find the best fit with the provided measurements. The second method (MATLAB MultiStart) will be exploited to recreate a more realistic situation in which a valid initial guess cannot be found and therefore a large number of possible initial solutions are used as a start point for an optimization algorithm that will try to minimize the difference between the measured curve and the estimated one. This method will be detailed in Chapter 2 to give a better understanding of its working principle.

In addition, the different aspects of the analysed problem will be presented in detailed in Chapter 5 but a brief introduction is here given.

The International Space Station (ISS) orbit and the Soil Moisture and Ocean Salinity (SMOS) one will be considered as the trajectories of the observed target. In this way, an orbit that experiences an eclipse region and a sun-synchronous orbit are considered.

The geometry defined during this work are a cubic microsatellite and a 3U CubeSat. For both, the body-mounted configuration and the one with two deployable solar panels can be simulated. Therefore, a six-faces geometry will be considered in the first case and a ten-faces for the second (the six of the main body plus two for each solar panel). Each surface will give its contribution to the measured flux, as better explained in Chapter 3.

Three different attitude motion will be defined in order to simulate different conditions of an observed RSO. The target characterized by these types of motion will be observed by three different observatories and with three different sensors that works in different wavelength bands. In this way, a complete picture of an observation strategy can be given and interesting comparison can be made.

2 | Fundamentals and Tools

2.1. Reference Frames

A reference frame is specified by an ordered set of three mutually orthogonal, possibly time dependent, unit-length direction vectors. All reference frames used within this work are right-handed: this means $Z = X \times Y$. The use of a reference frame is mandatory to describe vectors related, for instance, to the satellite position and velocity. A first distinction can be made between the inertial and non-inertial reference frames. The inertial ones are non-rotating with respect to the stars considered as a reference and they also have a non-accelerating origin.

In this work, some reference frames, all Cartesian, needs to be detailed since they will be used to define some quantities of interest.

- Earth Centered Inertial (ECI) (Figure 2.1): an inertial frame with origin in the center of the Earth and fixed with respect to the stars. The z axis corresponds to the angular momentum of the revolution of the Earth around the Sun, so it is perpendicular to the orbital plane (ecliptic), the x axis points towards the vernal equinox, which is the direction of the Earth-sun vector during the equinox that happens during March (the first day of spring in the northern hemisphere), and the y axis forms a right-handed triad with the other two axes.
- Earth-Centered Earth-Fixed (ECEF) (Figure 2.2): this frame has its origin in the center of mass of the Earth, the z axis is aligned with the direction of the north pole, the x axis points towards the Greenwich reference meridian and lies onto the equator, and the y axis forms a right-handed triad with the other two axes. Since these directions are fixed with respect to the Earth's surface, this reference system rotates with the Earth. The spherical coordinates to describe the position of an object are:
  - Geocentric radius: the distance of the object from the center of the Earth.
  - Latitude (ϕ or Lat): the angle between the equatorial plane and the vector

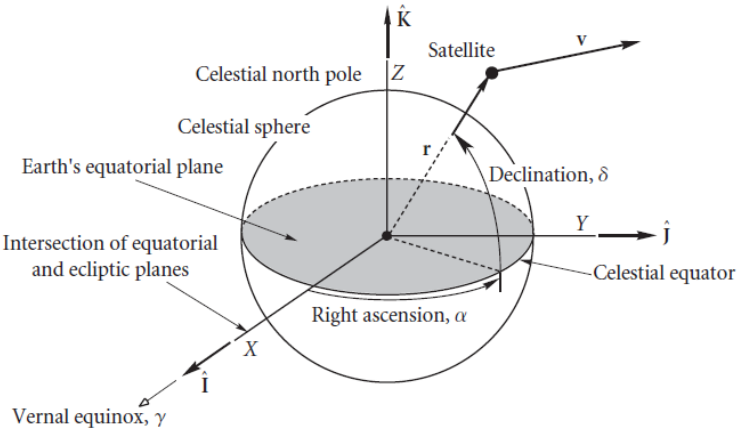

Figure 2.1: ECI reference frame

connecting the origin to the object, positive towards the north.

– Longitude (λ or Lon): the angle between the x axis (Greenwich meridian) and the projection of the position vector of the object onto the equatorial plane, positive counterclockwise.

- Local Vertical Local Horizontal (LVLH) (Figure 2.3): a non-inertial frame with the origin on the satellite gravity center. The z axis is a unit vector collinear and opposite sign of gravimetric satellite position. The y axis is a unit vector collinear and opposite sign of the orbital kinetic momentum. Consequently, the x axis is given by $y \times z$. This reference frame will be used in this work as a reference for the earth-pointing configuration, since the z axis is constantly pointing towards the center of the earth.

- Tangential Normal "Omega" (TNW) (Figure 2.4): as the LVLH, it is a non-inertial reference frame with the origin on the satellite gravity center. The letter "W" stands for the Greek letter ω denoting the axis of angular momentum. The x axis is a unit vector collinear to absolute orbital velocity. The z axis is a unit vector collinear to orbital kinetic momentum. Consequently, the y axis is given by $z \times x$.

- Body-fixed frame: this frame is fixed with respect to the considered body, the origin is the center of mass, and the axes are usually aligned with its principal axes of inertia or its axes of symmetry. This frame is useful to describe the dynamics and kinematics of the body. The normal of the surfaces composing the satellite will be considered aligned with the axes of this reference frame.

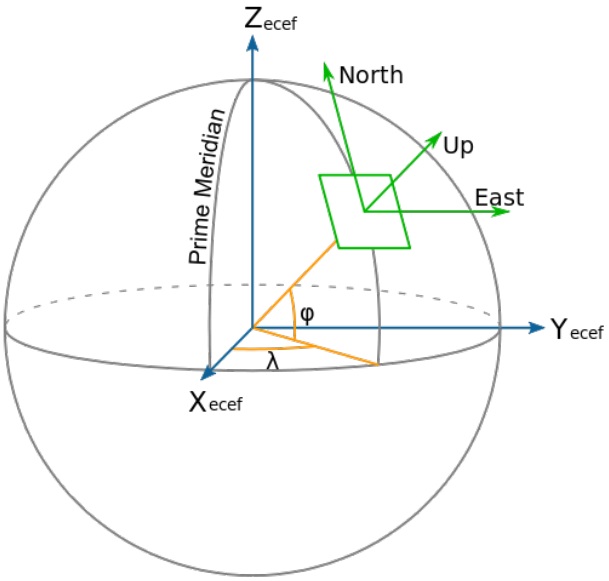

Figure 2.2: ECEF reference frame

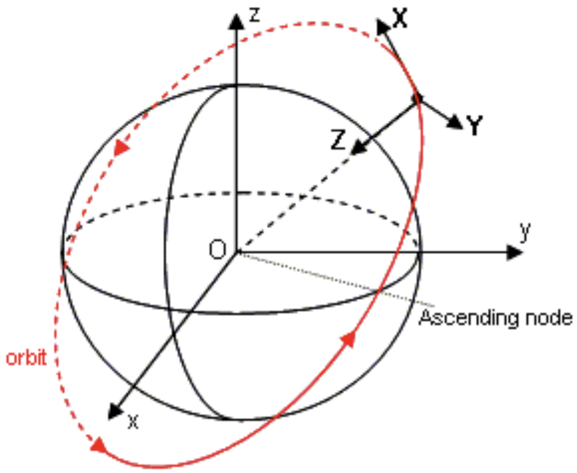

Figure 2.3: LVLH reference frame

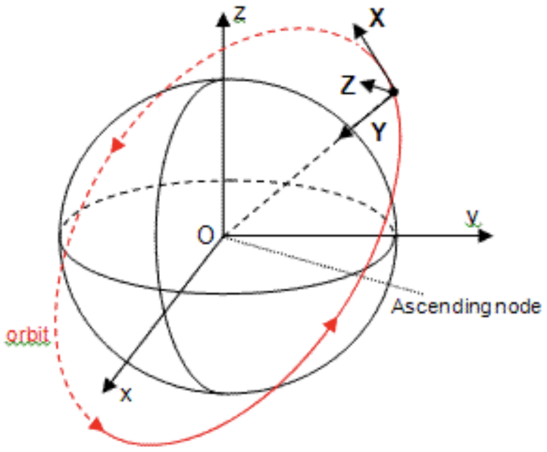

Figure 2.4: TNW reference frame

2.2. Satellite Attitude

A spacecraft has its own three-dimensional orientation, known as body coordinates. The three orthogonal, right-handed unit vectors, defining the body-fixed reference frame, are typically selected in some meaningful way, such as along the principal axes of inertia. This coordinate system of the body is then usually compared with some inertial reference system so that changes can be measured. For this reason, a definition of quantities allowing for a description of satellite attitude has to be introduced.

2.2.1. Dynamics

Euler's rotation equations are a vectorial set of first-order ordinary differential equations. They describe the time evolution of the angular velocity of a rigid body, by using a rotating reference frame with its axes fixed to the body. The dynamics of the attitude motion of a satellite can be described by these equations. They are reported in the vectorial form in (2.1).

$$\boldsymbol{J}\,\dot{\boldsymbol{\omega}} = \boldsymbol{J}\,\boldsymbol{\omega} \times \boldsymbol{\omega} + \boldsymbol{M} \tag{2.1}$$

The term $\boldsymbol{J}$ represents the inertia matrix of the body, $\boldsymbol{\omega}$ is the body angular velocity vector, $\boldsymbol{M}$ is a vector containing all the external torques acting on the body.

In the case the body frame is aligned with the principal axes of inertia, the inertia matrix becomes diagonal and the equations can be written in a simplified way, as shown in (2.2).

$$\begin{cases} I_x\,\dot{\omega_x} + (I_z - I_y)\,\omega_z\,\omega_y = M_x \\ I_y\,\dot{\omega_y} + (I_x - I_z)\,\omega_x\,\omega_z = M_y \\ I_z\,\dot{\omega_z} + (I_y - I_x)\,\omega_y\,\omega_x = M_z \end{cases} \tag{2.2}$$

2.2.2. Kinematics

As already stated, it is always necessary to be able to switch from a reference frame to another one that could be of interest to represent the attitude motion of a body. This is relevant for the purpose of this work that deals with remote sensing, and so there is an observer placed on the Earth's surface that points to a moving target orbiting around it. To define the orientation of one frame with respect to another, three parameters are the minimal set required. Often redundant parameters are used, i.e. more than three, either in order to improve the physical insight into the transformation or to simplify some numerical analysis.

There exist many ways of expressing the kinematic equations of a body, based on the use of different types of parameters. Euler's rotation theorem states that, in three-dimensional space, any displacement of a rigid body such that a point on the rigid body remains fixed, is equivalent to a single rotation about some axis that runs through the fixed point; this axis is called the Euler axis ($\boldsymbol{e}$) and the rotation angle is called Euler angle (Φ). It is possible to represent the attitude of an object with respect to an inertial frame by using the Euler axis and angle, which can be seen as a rotation of the inertial frame that aligns it to the body frame. From these concepts, it is then possible to introduce the notion of the quaternion. It is a vector of four parameters, linked to the Euler axis/angle through the relation expressed in (2.3).

$$\begin{cases} q_1 = e_1\,sin\,\dfrac{\phi}{2} \\ q_2 = e_2\,sin\,\dfrac{\phi}{2} \\ q_3 = e_3\,sin\,\dfrac{\phi}{2} \\ q_4 = cos\,\dfrac{\phi}{2} \end{cases} \tag{2.3}$$

These four parameters obey to the following constraint equation:

$$q_1^2 + q_2^2 + q_3^2 + q_4^2 = 1 \tag{2.4}$$

This representation also has a physical meaning, although not as obvious as Euler's angles. A quaternion contains information on the axis and angle of rotation required to move from one reference frame to another. However, when using Euler angle sequences, a phenomenon which is called Gimbal Lock (singularity) occurs when two axes align and a degree of freedom is lost. This is avoided when quaternions are used. They also have the advantage in size with respect to a 3×3 rotation matrix (4 scalars vs. 9) and speed (quaternion multiplication is much faster than 3×3 matrix multiplication).

Finally, the quaternion kinematics can be expressed through the equation (2.5), where the matrix $\boldsymbol{\Omega}$, described in (2.6), contains the angular velocity components in the body-fixed reference frame. This relation is integrated to obtain the time evolution of the quaternions, and so the attitude of the body with respect to the desired reference frame.

$$\dot{\boldsymbol{q}} = \frac{1}{2}\boldsymbol{\Omega}\,\boldsymbol{q} \tag{2.5}$$

$$\boldsymbol{\Omega} = \begin{pmatrix} 0 & \omega_z & -\omega_y & \omega_x \\ -\omega_z & 0 & \omega_x & \omega_y \\ \omega_y & -\omega_x & 0 & \omega_z \\ -\omega_x & -\omega_y & -\omega_z & 0 \end{pmatrix} \tag{2.6}$$

2.3. Non-linear Weighted Least Squares

Given a set of N measurements affected by errors and a parametric function, the least-squares method aims to determine those parameters which minimize an objective function J. The following description of this method is derived from [34]. Let $f(t, \boldsymbol{x})$ be a parametric function with t as independent variable and $\boldsymbol{x}$ as the M-dimensional parameters vector. If y_i represents the i-th measurements of a physical event at time t_i associated with the weight w_i, the least-squares criterion foresees the minimization of the so-called residual equation

$$J = \sum_{i=1}^{N} w_i^2 \bar{r}_i^2 = \bar{\boldsymbol{r}}^{\boldsymbol{T}} \boldsymbol{W} \bar{\boldsymbol{r}} \tag{2.7}$$

where

$$\bar{r}_i = y_i - f(t_i, \boldsymbol{x}) \tag{2.8}$$

is only dependent on the unknown parameters, and the weighting matrix is

$$\boldsymbol{W} = diag(\overline{\boldsymbol{w}}) \tag{2.9}$$

where

$$\overline{\boldsymbol{w}} = \left[\; w_1^2, \ldots, w_N^2 \; \right] \tag{2.10}$$

The goal is to find a minimum for J, so the problem to solve is

$$\frac{dJ}{d\boldsymbol{x}} = 0 \tag{2.11}$$

so the objective function is derived with respect to the M parameters x_j to find the following expression

$$\sum_{i=1}^{N} \bar{r}_i w_i^2 \frac{\partial \bar{r}_i}{\partial x_j} = -\sum_{i=1}^{N} w_i^2 \bar{r}_i \frac{\partial f(t_i, x)}{\partial x_j} = 0 \tag{2.12}$$

which can be written in the following matrix form

$$-\boldsymbol{W} \begin{bmatrix} \frac{\partial f(t_1,x)}{\partial x_1} & \cdots & \frac{\partial f(t_N,x)}{\partial x_1} \\ \vdots & & \vdots \\ \frac{\partial f(t_1,x)}{\partial x_M} & \cdots & \frac{\partial f(t_N,x)}{\partial x_M} \end{bmatrix} \begin{bmatrix} \bar{r}_1 \\ \vdots \\ \bar{r}_N \end{bmatrix} = \begin{bmatrix} 0 \\ 0 \end{bmatrix} \tag{2.13}$$

Let $\boldsymbol{A}^T$ be the partial derivatives $N \times M$ matrix, so the last equation can be written in a simpler manner by using (2.8)

$$\boldsymbol{W}\boldsymbol{A}^T \begin{bmatrix} y_1 \\ \vdots \\ y_N \end{bmatrix} - \boldsymbol{W}\boldsymbol{A}^T \begin{bmatrix} f(t_1, x) \\ \vdots \\ f(t_N, x) \end{bmatrix} = \begin{bmatrix} 0 \\ 0 \end{bmatrix} \tag{2.14}$$

This non-linear system of equation is difficult to solve, so the Taylor expansion around a known state x^n until the first term can be exploited

$$\boldsymbol{W}\boldsymbol{A}^T \begin{bmatrix} y_1 \\ \vdots \\ y_N \end{bmatrix} =$$

$$\boldsymbol{W}\boldsymbol{A}^T \begin{bmatrix} f(t_1) + \Delta x_1 \frac{\partial f(t_1)}{\partial x_1} + \ldots + \Delta x_M \frac{\partial f(t_1)}{\partial x_M} \\ \vdots \\ f(t_N) + \Delta x_1 \frac{\partial f(t_N)}{\partial x_1} + \ldots + \Delta x_M \frac{\partial f(t_N)}{\partial x_M} \end{bmatrix} \tag{2.15}$$

At the end, by assigning

$$\boldsymbol{b} = \begin{bmatrix} y_1 - f(t_1) \\ \vdots \\ y_N - f(t_N) \end{bmatrix} \quad \text{and} \quad \boldsymbol{\delta\hat{x}} = \begin{bmatrix} \Delta x_1 \\ \vdots \\ \Delta x_M \end{bmatrix}$$

the following form is obtained

$$\boldsymbol{\delta\hat{x}} = \left(\boldsymbol{A^T W A}\right)^{-1} \boldsymbol{A^T W b} \tag{2.16}$$

Concerning the algorithm, only an initial estimation of $\boldsymbol{x}$, the so-called guess state $\boldsymbol{x}_0$, is necessary to create an iterative process that, under convergence conditions, provides the solution. At the end, the iterative process returns the least-squares refined state vector. Another important output of the function *lsqnonlin* is the Jacobian matrix $\boldsymbol{A}$ which, for Gauss-Newton or Levenberg-Marquardt assumptions, can be used to estimate the Hessian matrix in order to calculate an approximate covariance matrix given by

$$\boldsymbol{C} = \left(\boldsymbol{A^T W A}\right)^{-1} MSE \tag{2.17}$$

where

$$MSE = \frac{\sum_{i=1}^{N} \bar{r}_i^2}{N - M} \tag{2.18}$$

This multiplicative term is used to reduce the errors generated by Hessian estimation, which is non-negligible if the residuals are large (see [37] for more details). The covariance matrix can be used for error propagation analysis as well as for calculating the state transition matrix.

2.4. MATLAB MultiStart Algorithm

The MATLAB *MultiStart* algorithm is a tool available in this software that could be useful for the problems faced in this work.

A MultiStart object in MATLAB contains properties that affect how the command "run" repeatedly runs a solver to find global or local minima; in particular, this object starts a local solver, such as "fmincon", starting from a previously generated set of points. MultiStart uses uniformly distributed starting points within the bounds, or the user can set the starting points manually.

MultiStart starts the local solver from all the starting points (that respect the bounds and the inequality constraints specified by the user, if present) and finds the corresponding local minima. Moreover, the local solver runs can be executed in parallel on multiple processors, which greatly reduces the computational time required.

When a MultiStart object is run, the algorithm performs the following steps [20]:

- Inputs validation: MultiStart checks input arguments for validity. Checks include running the local solver once on problem inputs. Even when run in parallel, MultiStart performs these checks serially.
- Start points generation: if a custom set of starting points is not provided, Multistart generates the specified number of starting points, randomly and uniformly distributed within the domain specified in the problem structure.
- Starting points filtering (optional): if specified, Multistart checks if the starting points respect the bounds and/or the inequality constraints of the problem; if these are not satisfied by some points, they are discarded from the rest of the calculations.
- Runs of the local solver: MultiStart runs the local solver starting from the points that passed the filtering phase; this process can be done in parallel computing. When the local solver runs stop, the result is stored.
- Check stopping conditions: MultiStart stops either if all the points have been analyzed, or if the running time exceeds the specified value.
- Create solution object: when the algorithm reached a stopping condition, MultiStart checks if there are multiple instances of the same local minima, according to a set tolerance for both their location in the domain and their objective function value; duplicates is not recorded in the final solution object. The resulting vector of GlobalOptimSolution objects is in order of their objective function value, from

lowest (best) to highest (worst).

The global minimum is assumed to be the lowest among the local ones found by the algorithm, but the knowledge of other possible local minima might be useful.

For the application of a minimization procedure, a metric has to be defined such that the algorithm can look for a minimum. For this reason, the mean squared error (MSE) has been selected. Its definition is expressed in (2.19), where Y_i is the *i-th* measured value and $\hat{Y}_i$ is the *i-th* estimated value.

$$MSE = \frac{1}{n}\sum_{i=1}^{n}(Y_i - \hat{Y}_i)^2 \tag{2.19}$$

2.5. Virtual Observatory

A fundamental part of this work involves the creation of synthetic measurements to test and validate algorithms and study their sensitivity to different observation schedules. For this reason a Virtual Observatory (VO) was used. This software is able to recreate optical and radar survey scenarios from any point on Earth, thanks to the use of Spacecraft Planet Instrument C-matrix Events (SPICE), a powerful tool developed by the Navigation and Ancillary Information Facility (NAIF) group at NASA [22]. In order to create simulations, two-line elements (TLEs) of the space object of interest are fed into the software. These files contain data that represent the ephemerides of the objects for a certain time interval. Thanks to this information, the states of the object and the desired observatory are created. The relative geometry analysis and the application of different constraints enable the definition of the so-called tracklets, which are sequences of N observations collected in a certain amount of time. The constraints used in the simulation are related to sky background luminosity, object elevation, object relative position with respect to Sun and Moon. Lastly, the observations are simulated by defining the sensor type and by adding user-defined measurement noises. For the purposes of this work, this tool has been exploited to recover the state of the observed RSO and the relative geometry considerations between the latter and the observatories placed on the surface of the earth. Many other uses of this tool are possible but were not relevant for the activities here presented. More details about the VO are given in [23].

3 | Thermal Remote Sensing

Remote sensing is the process of detecting and monitoring the physical features of a target by exploiting different kinds of instruments. The variety of instrumentation used today for this purpose is justified by the different physical principles on which they are based, allowing us to measure different types of quantity. A first important distinction in the field of remote sensing is the difference between ground-based and space-based applications, which are distinguished by the position on which the instrument is placed. They both present many advantages and disadvantages, and for this reason, they are both widely exploited today. For what concerns ground-based remote sensing, which is the focus of this work, can be highlighted the possibility of using very large and heavy instruments that cannot be placed on a spacecraft and that allow reaching higher performances without evident constraints. For instance, they offer an advantage over space-based observations by achieving unrivaled spatial and spectral resolution. For the advantageous possibilities related to the exploitation of ground-based instruments, a large number of ground stations are present on the Earth's surface that is managed both by public and private companies. The increasing number of RSO in different orbit environments, and the need for a deep knowledge of their current state in terms of trajectory and attitude, made the development of these facilities more and more essential. In particular, among the instruments used for remote sensing applications, this work aims to focus on ground-based infrared sensors because of the increasing interest developed in recent years.

3.1. Basic Principles of Radiation

All objects above absolute zero emit infrared radiation. This is the fundamental physical principle that guided the exploration of infrared technologies over the years. For this reason, the first step in approaching this kind of sensor is to recover the fundamentals of radiation. It is the emission or transmission of energy in the form of waves or particles through space or a material medium and it is also the most important way of transferring heat in the space environment. It is the most complex of heat transfer modes, and its mathematical treatment must invoke many simplifying assumptions to make it treatable

[14].

A first important notion is that of a black body, which, according to Kirchhoff, denotes a body that has the property of allowing all incident rays to enter without surface reflection and not allowing them to leave again. For this reason, it is characterized by an emissivity, that is its effectiveness in emitting energy as thermal radiation, quantified as unitary. For practical applications, one must consider that the objects of interest cannot be classified as perfect black bodies. The model of grey-body is instead exploited, which includes an emissivity coefficient lower than one and constant for each wavelength, temperature, and direction. By assuming these characteristics for an object of interest, to later qualify its emitted thermal radiation, Planck's law is fundamental. It describes the spectral density of electromagnetic radiation emitted by a black body in thermal equilibrium at a given temperature T when there is no net flow of matter or energy between the body and its environment [24]. This equation is therefore a function of the actual temperature of a body and allows for the calculation of the emitted radiation in a wavelength range of interest. This is a very important tool to quantify the emitted infrared flux of the target of interest.

$$B(\lambda, T) = \varepsilon \frac{2\pi h c^2}{\lambda^5} \frac{1}{e^{\frac{hc}{\lambda k_{\mathrm{B}} T}} - 1} \tag{3.1}$$

In (3.1) Planck's law for a grey-body is reported. The Planck constant is denoted as h, the speed in the medium as c, the Boltzmann constant as k_B, the emissivity as ε, the wavelength as λ and the temperature as T.

The integration of Planck's law over the whole spectrum leads to the Stefan-Boltzmann law, which states that the total energy radiated per unit surface area of a body across all wavelengths per unit time is directly proportional to the fourth power of the body's thermodynamic temperature T. This is described in (3.2), where the Stefan-Boltzmann constant σ is present.

$$Q = \varepsilon \, \sigma \, T^4 \tag{3.2}$$

In this way, one can calculate the total radiation emitted by the body of interest without filtering a specific wavelength of interest. This quantity will play a fundamental role in the thermal energy balance that one has to perform to calculate the body's temperature at a given time instant. Moreover, always referring to the body's emitted radiation, Wien's displacement law states that the black-body radiation curve for different temperatures will

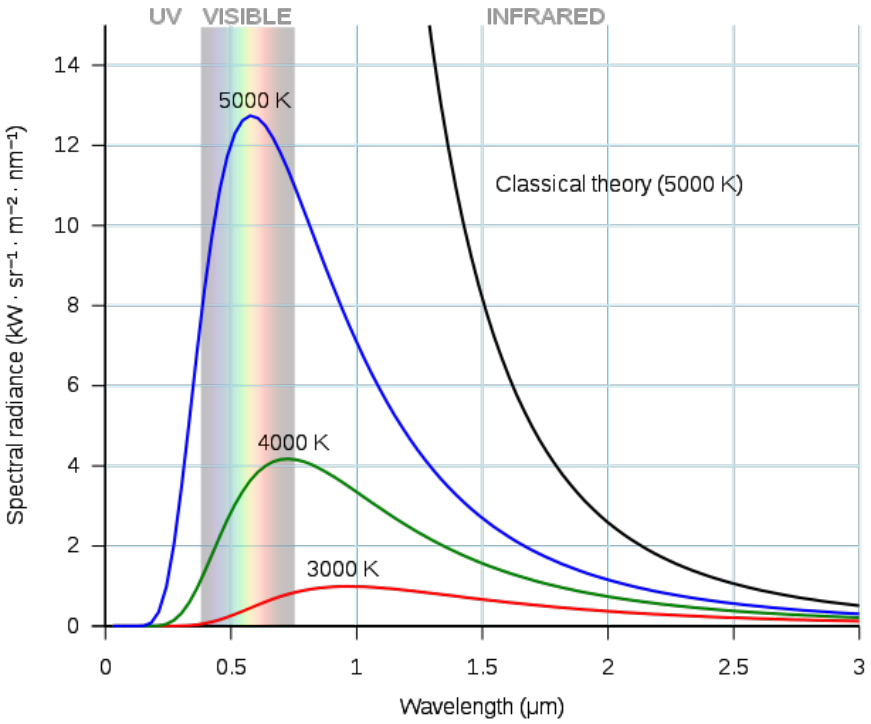

Figure 3.1: Black body spectral radiance

peak at different wavelengths that are inversely proportional to the temperature. This is expressed by the relation (3.3).

$$\lambda_{peak} = \frac{2898\,\mu m\,K}{T} \tag{3.3}$$

A graphical representation allowing us to better understand these basic concepts is reported in Figure 3.1, which shows the spectral radiance for a black body.

Figure 3.1 also allows us to visualize the separation between the visible realm and the infrared one. Typically, the infrared domain is generally understood to encompass wavelengths from the nominal red edge of the visible spectrum around $0.7\,\mu m$, to $100\,\mu m$. A relevant consideration that can be made by noticing the behavior of the spectral curves is that for lower temperatures (lower than 3000 K) the peak is moving towards the infrared region. This means that detectors operating in this wavelength range could provide useful information for bodies whose temperature is within a certain range and that therefore do not emit a large amount of radiation in the visible band. In fact, this is the typical case for RSOs that are the interesting targets for our investigation.

3.2. Transmission by the Atmosphere

Earth's atmosphere plays an important role in the infrared detection process because of its interaction with the body's emitted radiation and because it is itself a source of radiation. Basic concepts about this phenomenon are given in [16], where the author states that the terrestrial atmosphere has a substantial opacity in the infrared spectrum due to rotational-vibrational transitions of trace molecules (e.g. CO_2, H_2O, CH_4, O_3). In some spectral regions, these molecular transitions blend creating a practically opaque sky. The region close to the visible one, from 0.7 to around 2 μm, is a part of the spectrum with small absorption of radiation. Also, the region between 8 and 13 μm, however, is reasonably free of interfering molecular transitions. Depending on the site and local weather, limited astronomical observations are possible up to 30-35 μm. Beyond 35 μm the atmosphere remains opaque until the sub-millimeter region is reached. The most important concept to convey about the role of the atmosphere in the measurement process is the presence of the so-called atmospheric windows. These are regions in which both sky transparency and sky emission present acceptable values and where therefore ground-based instruments can operate. In practice, different infrared windows are defined, with different levels of atmospheric conditions. In Table 3.1 this information is reported according to [13].

Wavelength range	Band	Sky Transparency	Sky Brightness
1.1 - 1.4 μm	J	high	low
1.5 - 1.8 μm	H	high	low
2.0 - 2.4 μm	K	high	low
3.0 - 4.0 μm	L	high	medium
4.6 - 5.0 μm	M	low	high
8.0 - 14 μm	N	medium	high
17 - 25 μm	Q	very low	high

Table 3.1: Infrared Windows in the Atmosphere

In this work, the role of the atmosphere will be taken into consideration by means of a corrective factor that will be mentioned in the radiometric equations. However, it has to be considered that atmospheric conditions play an important role and can thus relevantly affect observation surveys. More specifically, as already stated, the atmosphere transmittance is a function of the wavelength λ and, therefore, this aspect should be considered inside the calculations performed in the radiometric chain when the simulated measurement is recovered. On the other hand, within the atmospheric windows, the

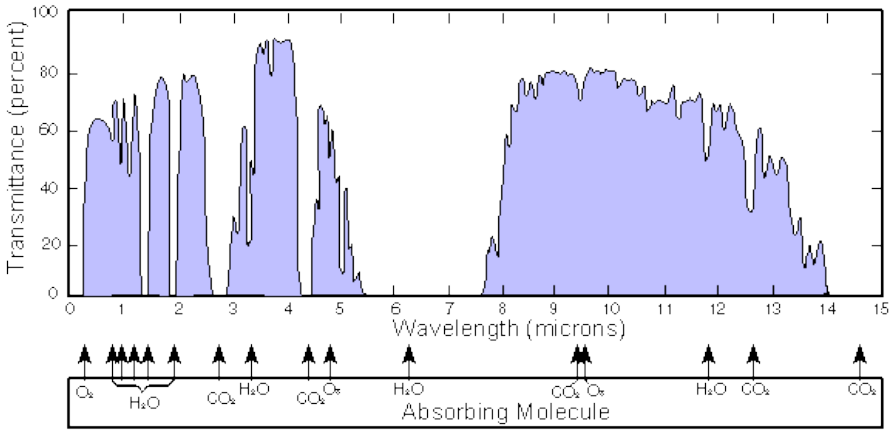

Figure 3.2: Atmospheric windows

behavior of this quantity does not vary relevantly and therefore an approximation of it as a constant can be accepted. This concept is shown in Figure 3.2, where the slight variation of this quantity within the infrared bands is clear. In addition, the value of the atmospheric transmittance is also dependent on the position of the observatory on the surface of the earth and on the instrument pointing angle θ. All these aspects should be considered when choosing the value to assign to $\tau_{atm}(\lambda, \theta)$.

For a more precise handling of this parameter, in his work [31] Shell proposes a model that links the atmospheric transmittance to the instrument pointing angle, as reported in (3.4), where τ_{atm0} has to be selected according to the observation site and the instrument used.

$$\tau_{atm}(\lambda, \theta) \simeq \tau_{atm}(\theta) = \tau_{atm0}{}^{\sec(\pi/2-\theta)} \tag{3.4}$$

3.3. Infrared Detectors

Since the discovery of infrared radiation by Herschel in 1800 and that of the ultraviolet by Ritter in 1801, there has been an increasing interest in the quantitative detection of radiation in the spectral region outside the visible one. This because of the low sensitivity of visual photometric methods and the interesting potential of these new techniques. The possibility to overcome the limitations shown by observation techniques in the typical visible spectral range, like the dependence on the target's illumination conditions, was crucial for the development of this technology.

Based on what explained by Gaussorgues [7], a radiation detector transforms an incident

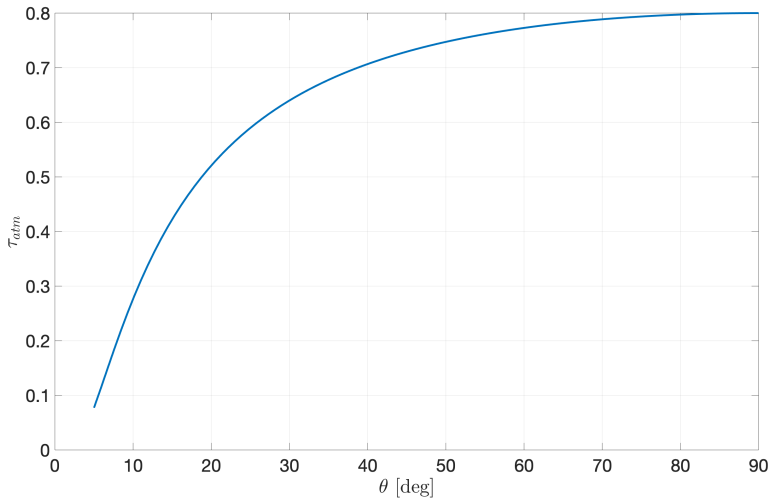

Figure 3.3: Atmospheric transmittance as a function of the elevation angle

optical signal that is a function of position x, y and time t (it can be a flux, an irradiance, or any other quantity corresponding to luminous energy) into an electrical signal or response (which can be voltage, current or power). There are two basic types of detectors:

- There are detectors of images that integrate over time so that the response is a function of the space variables. For astronomical applications, this kind of instrument produces images with the sky in the background and a lighter line representing the space object passing inside the field of view.
- There are detectors of flux that integrate the optical signal over the space variables and produce a response that is a function of time. In other words, through this instrument one can recover the temporal evolution of the incident signal. This is the type of instrument on which this work focuses, since the purpose is to simulate the infrared emission of a space object over the visibility interval with respect to a ground station.

An optical instrument has two main parts: the sensor is located in the focal plane of an optical system, the detector array is then referred to as the Focal Plane Array (FPA), while the circuit module, which is in charge of the conversion of the signal detected by the detector into a signal that can be electrically measured and read. Therefore is possible to differentiate two concepts, detection and readout. According to this, it is then possible to classify infrared detectors according to the way in which the measure is acquired, the material of the sensitive element, the circuit used for the processing of the signal, among other parameters as the infrared operating wavelength for the detector.

Based on the working principle of the sensor, infrared detectors can be split into two broad categories. These are the photodetectors and thermal detectors. The first are also known as photon detectors or quantum detectors. The main difference in the operational principle of photodetectors and thermal detectors is given by the FPA sensitive part. The differences in the electronic module are not so significant. In the case of photodetectors, the sensitive part converts an incoming signal of photons into a current of electrons, to be later processed in the electronic module. On the other hand, the FPA of thermal detectors reacts changing its temperature when it enters in contact with a flux of infrared radiation, therefore they do not convert the incoming flux of photons into electrons, as in the case of photodetectors. Then, these changes in temperature will be measured in a different way depending on the type of thermal detector. For example, in bolometer detectors, a type of thermal detectors, what it is measured is the change in the electrical resistance of the FPA after the detection of the photon signal [27].

At the moment, the research in infrared detectors is directed towards photodetectors operating at high temperature (larger than 130 K). On the other hand, thermal detectors have reached also a very important relevance due to its low cost and small size. Their performance are still lower than photodetectors, but they are projected to be real competitors of the photodetectors in the near future [36].

In general, the performance and development of thermal detectors, in terms of sensitivity, signal-to-noise ratio and wavelength tunability, is considerably lower than photodetectors. It is important to consider that the first commercial bolometer detector appeared at the beginning of the 1990s, 40 years later than the first HgCdTe photodetectors, therefore there was a big gap in the technology [28]. In spite of this, nowadays the interest in thermal detectors has soared as it has been reported by the companies providing software for the development of infrared detectors.

3.3.1. Characterisation of Infrared Systems

There are several useful criteria for the characterization of the measuring infrared system performance. Their definitions are important to then understand if a sensor is suitable for the context in which it will be used. The following summary is extracted from Gaussorgues [7].

- **Detectivity:** It is the inverse of the Noise Equivalent Power (NEP), which is defined as the amount of absorbed power in the detector that generates on it an output signal equal to the detector noise.
- **Specific detectivity:** The specific detectivity, D^* , is defined as the photosensi-

tivity per unit of active area and unit of bandwidth of a detector, and is reported in (3.5). In this expression, A is the pixel pitch and Δf is the frequency bandwidth of the sensor, defined as the inverse of the double of the time constant t_c.

$$D^* = \frac{\sqrt{A\,\Delta f}}{NEP} \tag{3.5}$$

It represents one of the main figures of merit of infrared detectors to describe its performance, most commonly used than the NEP. In addition to this, it is a very useful parameter in the comparison of different detectors, because it is defined per unit of area and unit of frequency bandwidth.

- **Thermal resolution:** This is the minimum detectable difference between the apparent temperatures of the object and its environment. The definition of thermal resolution takes different forms, depending on the nature of the object.
- **Spatial Resolution:** This is defined as the smallest separation between details on the object, expressed as a solid angle, for which the details are still seen as separate. It is usually the elementary solid angle of analysis by the system that results from a combination of factors such as the transfer functions of the optics, detector, electronics, visualization system, and the eye of the observer.
- **Spectral Response:** This is the optical pass band of the system, usually specified as the wavelength interval $\Delta\lambda = \lambda_b - \lambda_a$ approximately centered on the mean wavelength λ_0 lying between λ_b and λ_a. The limits of the spectral interval are determined by the combined response of the optics, filter, and detector.
- **Quantum efficiency:** This parameter defines the number of incident photons converted to electrons in a photodetector, i.e. the capability of a detector to convert light energy to electrical energy, expressed as a percentage. Quantum efficiency varies with wavelength and can be extended across these wavelengths through innovations such as backthinning, back-illumination, anti-reflective coatings and high resistivity silicon.

If the angular size of the object is greater than the size corresponding to the spatial resolution of the system, and if it produces a power on the entrance pupil that is greater than the noise equivalent power of the system, it will be correctly reproduced provided the apparent temperature difference between the object and its environment is greater than the thermal resolution.

3.3.2. Sensors

Given the earlier explained concepts about the wavelength spectrum and the role of the atmosphere, it is then possible to identify the instruments best suited to acquiring measurements in different wavelength bands. An important notion to remark is that the overall incoming flux reaching the sensor is the sum of emitted and reflected components. As stated before, the temperature of an RSO in the LEO environment is around 300 K and therefore its emitted radiation has its peak close to 10 μm. This means that measurements acquired in a band close to the visible one would be solely influenced by the reflected component of radiation, while a band close to 10 μm would allow us to be more sensitive to the emitted component. The infrared region can in fact be divided into two categories based on these radiation properties. Within the reflected IR category there is the Near-Infrared (NIR) band, from 0.7 to 1.3 μm, and Short Wave Infrared (SWIR) band, from 1.3 to 3 μm, while in the emissive IR category there is the Long-Wave-Infrared (LWIR) band, from 8 to 14 μm. These bands correspond to an atmospheric window, leading to favorable values of atmospheric transmittace. Regarding the sky brightness, which is a source of noise in the measurement process, NIR presents values around 16 mag/arcsec^2, while the LWIR background is overwhelming and astronomical sources have the challenge of standing out against the atmosphere with values of brightness of about -3 mag/arcsec^2 [19]. This is coupled with the high spatial and temporal variability of atmospheric emission which varies unpredictably at a frequency $>$ 1 Hz due to air turbulence in the optical path, and telescope emissions which vary at frequencies of $>$ 0.02 Hz [25]. Working in the LWIR band leads to the great advantage of being independent on the illumination conditions of the target, which is always a challenging aspect for telescopes working in the reflected category. This means that the eclipse phase of a target orbiting around the Earth could be available to the acquisition of infrared measurements in LWIR. Therefore, in NIR and SWIR there is the need of a favorable relative configuration between the sun and the observed object to have enough reflected flux to be measured, while in LWIR the elevation angle of the sun strongly influences the background noise that affects the measure.

Lastly, some considerations can be made regarding the comparison with the widely used visible band for astronomical observations. Nowadays, optical telescope working in the visible range are largely used thanks to their reliability and the deep knowledge about their performance and the quality of the acquired measurements that contain useful information to make estimate of the state of the observed object. Despite this, as already stated in the introduction, there has been an increasing interest in the use of infrared technology, mainly for the reasons explained in the earlier paragraph, like the typical temperature

range of RSO in both LEO and GEO environments. In fact, both infrared bands are larger in terms of wavelength range compared to the visibile one and, therefore, there is the possibility to acquire more energy associated to the incident electromagnetic radiation.

Three instruments working in different wavelength ranges will be presented in the following. They will be used as a reference to simulate an acquired measurement to then make a comparison of their performance based on their signal-to-noise ratio. They will be referred to as System 1, 2 and 3.

System 1: visible

This instrument works in the visible range, from 0.4 to 0.7 μm, and is based on the charge coupled device (CCD) technology. The following technical description of the sensor is extracted from the datasheet available on the *Teledyne* website. As well explained in [32], the CCD is divided up into a large number of light-sensitive small areas (known as pixels) which can be used to build up an image of the scene of interest. A photon of light which falls within the area defined by one of the pixels will be converted into one (or more) electrons and the number of electrons collected will be directly proportional to the intensity of the scene at each pixel. When the CCD is clocked out, the number of electrons in each pixel are measured and the scene can be reconstructed.

The CCD201-20 is a frame transfer, electron multiplying CCD sensor designed for extreme performance in high frame rate ultra-low light applications. The Teledyne e2v back-thinning process ensures high quantum efficiency over a wide range of wavelengths.

The device functions by converting photons to charge in the image area during the integration time period, then transferring this charge through the image and store sections into the readout register. Following transfer through the readout register, the charge is multiplied in the gain register prior to conversion to a voltage by the Large Signal Output amplifier (OSL).

An important aspect to consider when dealing with sensors, is the intrinsic presence of noise that will affect the acquired measure. There are a number of contributions to the noise performance of a CCD and that will be used to define the signal-to-noise ratio.

Dark current is thermally generated noise. At room temperature, the noise performance of a CCD can be thousands of electrons per pixel per second. In this situation, the full well capacity of each pixel will be reached in a few seconds and the CCD will be saturated. Dark current can be reduced by cooling the detector with a system such as a Peltier cooler or even a cryo-cooler which can reduce the noise performance of the CCD to only tens of

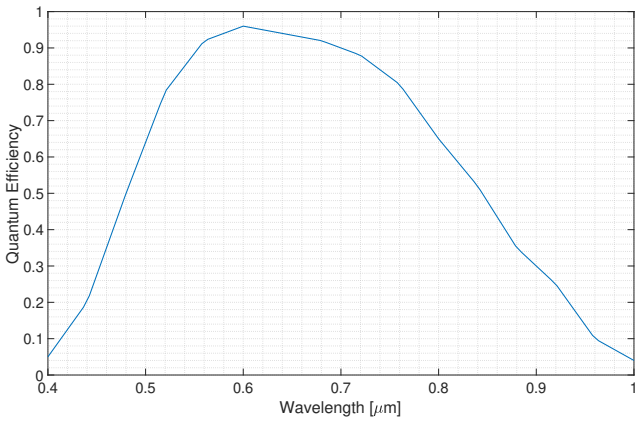

Figure 3.4: Quantum efficiency CCD201-20

electrons per pixel per second at -40° C.

The readout noise originates from the conversion of the electrons in each pixel to a voltage on the CCD output node. The magnitude of this noise depends on the size of the output node. Advances have been made in reducing CCD readout noise and continues to be an important part of current and future CCD development. Readout noise determines the dynamic range and should be as low as possible, especially for detecting very faint energy sources.

Typical quantum efficiency values of this sensor, for a temperature around -20° C, are reported in Figure 3.4.

System 2: NIR / SWIR

The second instrument, the NIRvana 640 from Teledyne Princeton Instruments, has a spectral response in the NIR/SWIR bands, going from 0.9 to 1.7 μm. From the datasheet of the instrument it can be seen that the NIRvana range uses large pixels, high quantum efficiencies and unbeaten low dark current noise to provide industry-leading signal to noise ratios. Combined with this is the incredible image quality achieved through advanced pixel correction algorithms, overcoming the inherent challenges of InGaAs sensors. Regarding camera noise sources, thermal photons from the scene and from the camera housing are ever-present, conveying background noise. The NIRvana series uses integrated cold shielding to keep these photons, and hence this unwanted background noise out of images.

Even for this instrument, the main sources of noise are the background flux, the dark current and the readout noise. Some studies has been conducted with this sensor, showing

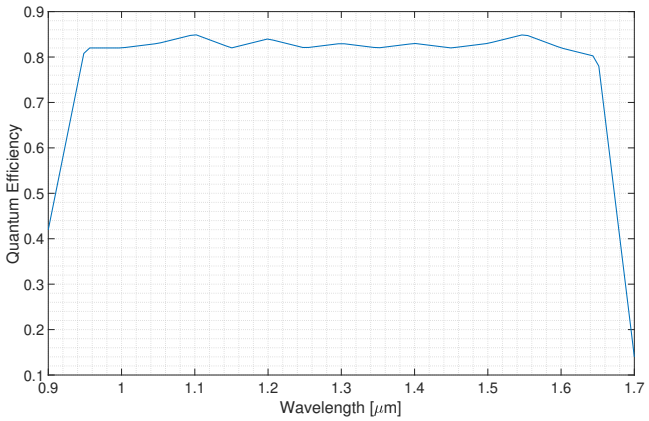

Figure 3.5: Quantum efficiency NIRvana 640

that the dominance of low dark current and large pixel sizes is evident; the NIRvana camera range offers superior sensitivity in practically every case. For the alternative cameras, due to their higher dark current, saturation of the pixel is frequently seen before an adequate signal to noise ratio can be achieved.

Concerning the quantum efficiency, the NIRvana 640 achieves >80% QE across an incredibly broad range, from 0.95 to 1.6 μm, enabling low light imaging across the NIR-II / SWIR region.

System 3: LWIR

Moving towards longer wavelengths, the energy associated to a photon significantly decreases and, therefore, CCD technology is not suitable for performing astronomical observations in this band. For this reason, the microbolometer technology is used in this IR region because of its ability to detect incident electromagnetic radiation associated with lower energy levels. Infrared radiation with wavelengths between 8–14 μm strikes the detector material, heating it, and thus changing its electrical resistance. This resistance change is measured and processed into temperatures which can be used to create an image. Unlike other types of infrared detecting equipment, a microbolometer is an uncooled thermal sensor. Previous high resolution thermal sensors required exotic and expensive cooling methods including stirling cycle coolers and liquid nitrogen coolers. These methods of cooling made early thermal imagers expensive to operate and unwieldy to move.

In particular, the third instrument used in this work is the Bird 640, a VOx microbolometer in a ceramic package by SemiConductor Devices. As explained in [26], there are several sources of noise in a microbolometer setup of which the most important are the

thermal noise and the flicker noise in resistances. For an object to be detectable, it is necessary that the incident electromagnetic radiation produces a power higher than the characteristic NEP of the sensor.

This microbolometer is characterized by a time constant t_c equal to 14 ms, a pixel pitch of $17 \times 17\,\mu m$ and a specific detectivity of $2.99 \times 10^7\, m\, Hz^{1/2}\, /W$. Therefore, the detectivity D is $2.94 \times 10^{11}\, W^{-1}$.

The three instruments are summed up in 3.2, and their performance will be analysed to identify the most suitable configuration for a ground-based infrared observation system. They will be referred to as Sys1, Sys2 and Sys3.

System ID	λ range [μm]	F#	Diameter [cm]	Pixel pitch [μm^2]	SNR threshold
Sys1	0.4-0.7	1.4	30	13×13	4
Sys2	0.9-1.7	2.2	50	20×20	4
Sys3	8-14	2.2	50	17×17	4

Table 3.2: System parameters

3.4. The Radiometric Chain

The previously explained notions about radiation are fundamentals to provide the knowledge on how a body, that will be the target of the measurement process, will behave in terms of emitted flux. Then, one has to consider the interaction between the target and the detector. It is fundamental to look at the global picture and understand the way the emitted radiation will interact with a ground-based sensor. The ensemble of phenomena that accompany the emission of radiation by a source, the environment in which it is found, the medium through which the radiation propagates, until it is absorbed by a detector, is called the radiometric chain [7]. It is fundamental to examine in detail each part of this chain and to evaluate its performance so that the possibilities and the limitations of a strategy could be highlighted. It would be hazardous to take measurements with equipment that is poorly suited to the phenomena under investigation, and the results thus obtained would not reflect the true possibilities of a judiciously chosen strategy [7].

Radiation detectors are the components that transform the received radiation into another form of energy. The radiance emitted by the target can be described by Planck's law integrated over a specified spectral range. Once the spectral working region of the detector is selected, the radiance, expressed in $W\, m^{-2}\, sr^{-1}$, can be therefore obtained with equation (3.6), which is the definite integral of the Planck law.

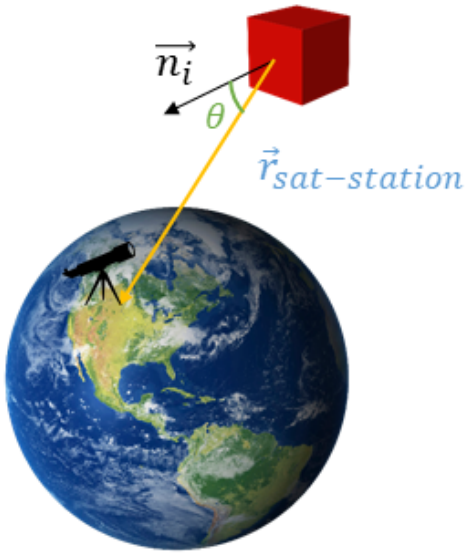

Figure 3.6: Relative angle between the surface and the observer

$$L = \int_{\lambda_L}^{\lambda_U} \varepsilon \frac{2\pi hc^2}{\lambda^5} \frac{1}{e^{\frac{hc}{\lambda k_B T}} - 1} d\lambda \tag{3.6}$$

Radiant flux is often used to describe the radiation power output of a radiation source, or the radiation power received by an optical instrument. It is a radiant power and obeys the laws of propagation in homogeneous non-absorbing media, and its unit is the watt. It is linked to the radiance through the following relation.

$$F = L \frac{A_{eff}\, A_p}{d^2} \tag{3.7}$$

Where A_p is the area of the optics entrance (pupil), d the distance between the target and the detector, and A_{eff} the effective area of the target seen by the sensor. This is calculated as in equation (3.8) by exploiting the angle between the normal vector of the surface and the relative position vector of the satellite with respect to the ground station (see Figure 3.6).

$$A_{eff} = A_t \cos\theta \tag{3.8}$$

In this process, it has to be considered that not only the radiation emitted by the target reaches the detector. Many other sources give their contribution to the measured flux. The most relevant is the flux due to atmospheric emission and reflections and the background radiation, which is the contribution of the ambient around the object. For this reason, the presence of external noise has to be considered in the quantity registered by the instrument. Many models can be adopted to describe this aspect of the radiometric chain; Gaussorgues [7] proposes the following. At the entrance optics of the detector, the flux coming from the target (F), the atmosphere, and the background (both considered in the term F_p) are received and their sum is referred to as the *incident flux* F_{inc}.

$$F_{inc} = \tau_{atm} F + F_p \tag{3.9}$$

Then, this incident flux is attenuated by the optics, but the emissivity of the optical surfaces gives rise to a further stray flux F_c that depends on the mean temperature T_c of the infrared camera. For this reason, the *detected flux* F_{det} received by the sensitive area of the detector is given by the following equation.

$$F_{det} = \tau_{opt} F_{inc} + F_c \tag{3.10}$$

The detected flux is therefore converted into an electrical signal by the detector. This conversion is guided by the sensitivity of the system. For the purposes of this work, F_{det} is the quantity of interest that will be used to recover the signal-to-noise ratio. The aim is to simulate the time evolution of this quantity, which can carry interesting information about some specific characteristic of the target.

These notions about the radiometric chain can then be applied to extract the quantity of interest for a particular geometry. As it will be better explained later, this work deals with 6-faces geometries. Each surface gives its contribution to generate the final infrared signature of the observed target.

Application to a study case

The notions of the radiometric chain can then be applied to extract the quantity of interest for a particular geometry. As it will be better explained in section 5.1.3, this work deals with 6-faces geometries. Each surface is considered as different object to which the previous equations are applied, therefore resulting in six different fluxes $F_{det,i}$. At the end, each surface gives its contribution to generate the final infrared signature of

the observed target as the sum of all the detected infrared fluxes.

Once the temperature evolution of the satellite, which is supposed to be the same for each surface for the geometry used in this work, is obtained, one can proceed with the calculations of the radiance through the equation (3.6) by applying the specific i-th emissivity of each surface. In this way, the six contributions named L_i, are obtained and the procedure can go on with the calculation of quantities extracted through relative geometry considerations. At each instant, the satellite position vector, velocity vector, and attitude in terms of angular velocity vector and quaternions, are extracted from previous calculations and they are used to calculate the distance d, which is therefore a scalar quantity, and the relative angles θ_i between each surface normal vector and the satellite position vector expressed with respect to the ground station. Then, the effective area seen by the observer for each surface of the target is computed, and this is then used to compute the i-th radiant flux F_i.

Finally, the six radiant fluxes can be summed to obtain the infrared signature of the target F in equation (3.11), which is then modified to obtain the detected one through the previously described equations.

$$F = \sum_{i=1}^{N} F_i \tag{3.11}$$

This flux is obtained thanks to the contribution given only by the surfaces that, at each instant, are visible to the observer. This means that, if the relative angle between the normal vector of the surface and the position vector of the surface with respect to the observer is higher than or equal to 90 degrees, then that surface does not contribute to the final infrared signature (therefore that specific F_i contribution is zero for that instant).

3.5. Signal to Noise Ratio

Concerning the process of the acquisition of a measure, one has to consider the presence of different sources that give their own contribution to the effective signal received by an instrument. It is unrealistic to have a measure without noise, and this is also the case in the context of astronomic observations. As always, the instrument itself is a source of noise. In addition, other external actors can contribute to the final measured signal, like the background and the atmosphere. For this reason, a commonly used quantity is the Signal-to-Noise Ratio (SNR), which is a measure used in science and engineering that compares the level of a desired signal to the level of noise [40]. SNR is defined as the ratio

of signal power P_s to the noise power P_n, as in (3.12), often expressed in decibels. Of particular interest to the designer of SSA systems is the rate of photons emitted by the SO and the background sky. Together, these two quantities are the greatest contributors to the SNR, which is frequently used to define the quality of a measure acquired with a digital sensor.

$$SNR = \frac{P_s}{P_n} \tag{3.12}$$

Generally, in the context of SST, the SNR of an image is the ratio of the total number of photons from the target to the number of photons generated by various noise sources, such as background sky pollution, CCD dark current, and CCD read noise. A higher SNR ratio is a result of a brighter SO in the image plane. This implies a greater probability of successful detection, and more accurate photometry results [12]. Consequently, the power of the noise at the denominator of SNR, can be defined as the sum of all these contributions.

This thesis uses the signal to noise ratio as the foundation for the limiting infrared flux performance metric and also as the basis for analyses performed on the acquired data. This quantity should be therefore used to determine whether a simulated measure is detectable or not based on a certain threshold, which is usually selected around 5. In addition, the evolution over time of the SNR contribution related to the attitude motion can be used to perform analysis on the simulated measurements in order to recover an information of interest.

3.5.1. SNR for photodetectors

In the case of photodetectors, the incoming photon flux is the quantity to use for the definition of the SNR. In fact, successful detection of an SO typically requires the number of photons emitted by the SO to be several times greater than the number of photons emitted by noise sources. The SNR of a measurement is typically defined as the quotient of the mean number of photons from the SO, μ_{SO}, by the standard deviation of photons from all noise sources, σ_n. The latter is given by the sum of all the contributions, according to equation (3.13). The arrival process of photons incident on the CCD plane can be accurately modeled by a Poisson process, therefore, given a signal s_i, its variance is given by the signal itself and $\sigma_i = \sqrt{s_i}$.

$$\sigma_n = \sqrt{\sum_{i=1}^{N} \sigma_i^2} \tag{3.13}$$

The overall signal received by the observed target is given by the sum of the emitted and reflected contributions, which are defined in (3.14) and (3.15). In the IR category of Sys1 and Sys2, the reflected component is predominant.

$$q_{SO,em} = \Delta t_{exp}\, \tau_{opt}\, \tau_{atm}\, A_{eff}\, \frac{A_p}{d^2} \int_{\lambda_L}^{\lambda_U} \varepsilon_{SO}\, \frac{2\pi c}{\lambda^4} \frac{1}{e^{\frac{hc}{\lambda k_B T_{SO}}} - 1}\, QE(\lambda)\, d\lambda \tag{3.14}$$

$$q_{SO,ref} = \Delta t_{exp}\, \tau_{opt}\, \tau_{atm}\, A_{eff}\, \frac{A_p}{d^2} \int_{\lambda_L}^{\lambda_U} \rho_{SO}\, \frac{2\pi c}{\lambda^4} \frac{1}{e^{\frac{hc}{\lambda k_B T_{sun}}} - 1}\, QE(\lambda)\, d\lambda \left(\frac{R_{sun}}{1AU}\right)^2 \tag{3.15}$$

In these equations, Δt_{exp} is the exposure time, τ_{opt} and τ_{atm} are the coefficients of the optics and of the atmosphere, A_{eff} is the effective area of the target seen by the observer, A_p is the pupil area of the instrument, d is the distance between the target and the observer, λ_L and λ_U are the lower and upper limits of the wavelength range of the sensor, ε and ρ are the emissivity and the reflectivity of the material. Finally, R_{sun} is the radius of the sun and 1AU is one astronomical unit.

Among the sources of noise there are the photon flux coming from the background, the dark current and the readout noise. The first contribution is described by (3.16), where N is the F-number, E_{sky} is a mean value of the sky irradiance, considered as a constant for a specific wavelength range, and A_{pxl} is the pixel pitch. The dark current contribution is given by the simple multiplication of the value called DC, expressed in $e^-/pixel/s$ and the exposure time, as in (3.17). The readout noise is given by the σ_{RO}^2 value, expressed in $e^-/pixel$.

$$q_{sky} = \Delta t_{exp}\, \tau_{opt}\, \tau_{atm}\, A_{pxl}\, \frac{\pi}{4N^2} \int_{\lambda_L}^{\lambda_U} \pi\, E_{sky}\, \frac{\lambda}{hc}\, QE(\lambda)\, d\lambda \tag{3.16}$$

$$q_{DC} = \Delta t_{exp}\, DC \tag{3.17}$$

Finally the SNR in dB for a photodetectors is given by equation (3.18), where G is the multiplicative gain of the instrument, F is the excess noise factor, whose value has been

set to $\sqrt{2}$, and q_{SO} is the sum of $q_{SO,ref}$ and $q_{SO,em}$.

$$SNR = 10 \log \frac{G\, q_{SO}}{\sqrt{F^2\, G\, (q_{SO} + q_{sky} + q_{DC}) + \sigma_{RO}^2}} \tag{3.18}$$

3.5.2. SNR for thermal detectors

As well explained in [36], in the case of thermal detectors, they do not convert the incoming flux of photons into electrons, and therefore SNR will be defined thanks to the power of the incoming signal in [W]. Then, the detector is characterised by a responsivity R defined as the output voltage/current per unit of received power in [A/W] or [V/W] respectively. This responsivity has to be multiplied by the incoming power in [W]. Therefore, the final signal used in the computation of the SNR is the output voltage or output current, which is divided by the noise voltage (the voltage generated by the instrinsic noise in the instrument). This principle is described in equation (3.19). Then, the ratio of the responsivity by the noise voltage is equivalent to the detectivity D. Therefore the SNR can be also calculated with equation (3.20).

$$SNR = 10 \log \frac{P\, R}{v_n} \tag{3.19}$$

$$SNR = 10 \log P\, D \tag{3.20}$$

Also here, the power received by the observed target is given by the sum of the emitted and reflected contributions. In the wavelength range of Sys3 the emitted contribution is much larger than the reflected one.

$$P_{SO,em} = \tau_{opt}\, \tau_{atm}\, A_{eff}\, \frac{A_p}{d^2} \int_{\lambda_L}^{\lambda_U} \varepsilon_{SO}\, \frac{2\pi h c^2}{\lambda^5} \frac{1}{e^{\frac{hc}{\lambda k_B T_{SO}}} - 1}\, d\lambda \tag{3.21}$$

$$P_{SO,ref} = \tau_{opt}\, \tau_{atm}\, A_{eff}\, \frac{A_p}{d^2} \int_{\lambda_L}^{\lambda_U} \rho_{SO}\, \frac{2\pi h c^2}{\lambda^5} \frac{1}{e^{\frac{hc}{\lambda k_B T_{sun}}} - 1}\, d\lambda \left(\frac{R_{sun}}{1AU}\right)^2 \tag{3.22}$$

3.5.3. SNR preliminary analysis

Once the three instruments have been characterized through some of their main parameters and the SNR for both types of sensors, it is possible to perform a preliminary analysis

of their performance through the comparison of the SNR calculated for different cases. In particular, a spherical space object will be considered, and the values of SNR for the three instruments will be compared according to different values of the diameter and elevation of the object, distance of the object from the observer. When one of this quantity is varying, the rest are fixed according the values reported in Table 3.3.

Parameter	Value	Units
Distance	400	km
Diameter	0.5	m
Elevation	60	deg
Temperature	300	K
Emissivity	0.7	-
Reflectivity	0.3	-

Table 3.3: Spherical space object parameters

In Figure 3.7, SNR is evaluated with a varying value of the object diameter, in 3.8 with a varying value of distance between the object and the observer, and in 3.9 with a varying value of object elevation with respect to the ground station. It could be noticed that Sys1 and Sys2 are almost always above the selected threshold of 4, while Sys3 is below this value for certain conditions.

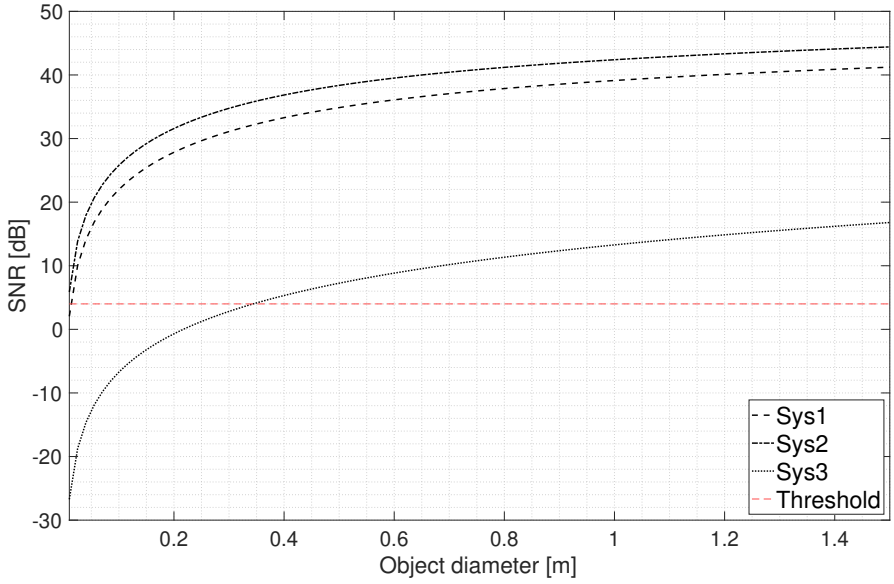

Figure 3.7: Dependence on SO diameter

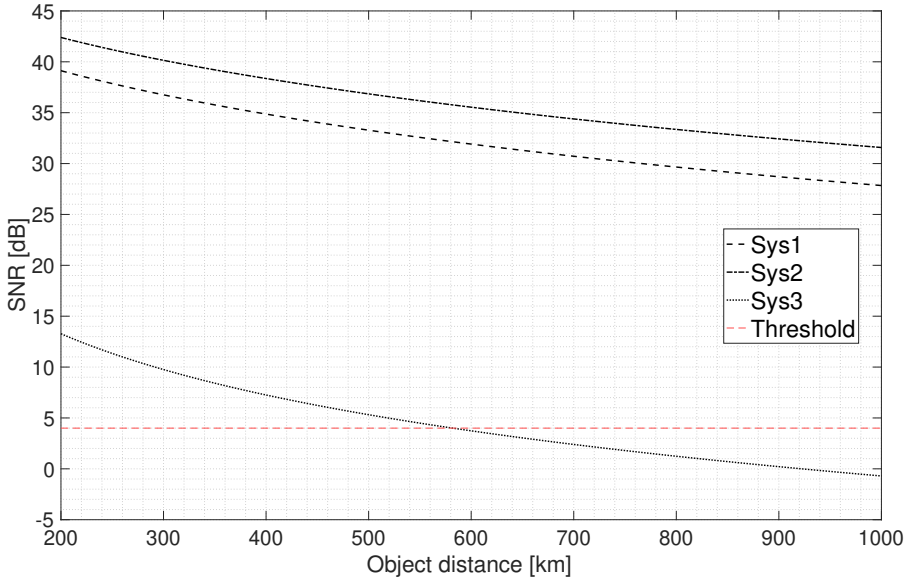

Figure 3.8: Dependence on SO distance

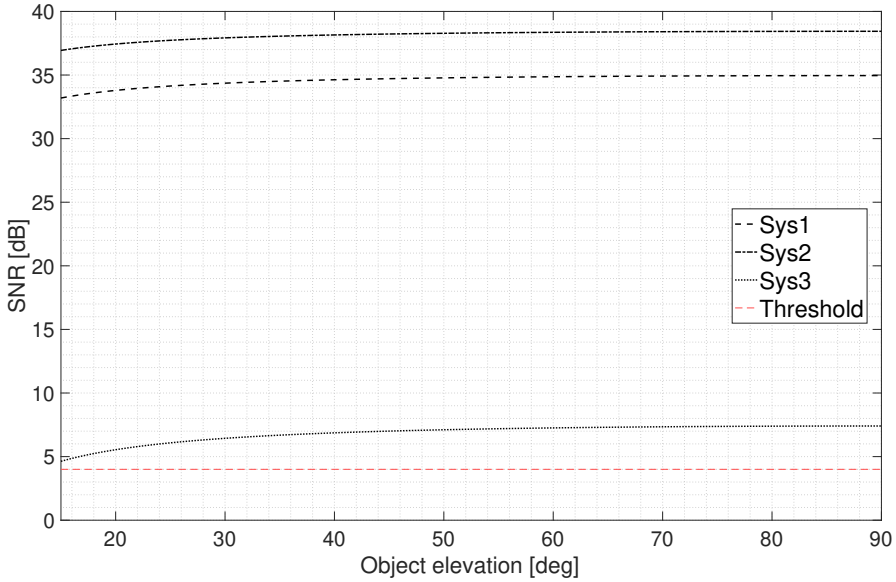

Figure 3.9: Dependence on SO elevation

In conclusion, it can be remarked that the performance of Sys3 are always lower compared to Sys1 and Sys2. This was expected since, as already stated during the description of photodetectors and thermal detectors, the first usually present higher performance in terms of SNR. Despite this, it has to be highlighted that these three instruments are based on different working principles and that Sys3 works in a wavelength range in which the emitted contribution of the incoming electromagnetic radiation is dominating. This

means that it could mitigate the problem of the illumination condition of the target and therefore acquire measurements even in different conditions, like during the eclipse phase of the orbit.

Regarding Sys1 and Sys2, the second shows better performance. This because of lower noise contribution of this instrument, but mainly because of the larger spectral reponse. In fact, one of the interesting aspects of infrared sensors is the possibility of acquiring measurements exploiting a larger band, which leads to more incoming radiation to be registered by the sensor.

4 | Satellite Thermal Analysis

The relation between the emitted infrared radiation and the temperature of a body has already been stated. It is thus fundamental to know the temperature evolution of the target to then extract the emitted flux over time. For this reason, a model for predicting the temperature of a satellite is examined. The aim is to develop a reliable and simplified predictive model such that all the most important constraints are considered and that a quite accurate temperature profile over the simulation time can be found. Firstly, basic notions necessary for the treatment of the thermal problem will be given. Then the thermal energy balance will be exploited to recover the temperature profile that is needed to draw some considerations about the variations of the satellite's state.

4.1. Orbit Environment Heating Fluxes

Satellite thermal analysis is concerned with predicting the temperature of a satellite in a known or assumed heating environment [14]. The first step to perform this analysis is therefore to know which are the main heat fluxes present in the space environment and to model them reliably for the case of interest. For the relevant targets of this work, three main heat fluxes affect the satellite surfaces.

4.1.1. Solar Radiation

Impinging radiation from the sun on a surface is characterized by the solar flux S (W/m^2), commonly known as the solar constant, and by its orientation with respect to the sun. Most measurements above the Earth's atmosphere have expressed a solar radiation flux value between 1365 and 1373 W/m^2 for LEO satellites. The great distance from the sun justifies the assumption that radiation is in parallel rays, which gives rise to the term solar vector, defining a vector of magnitude S with the direction along with the rays. Solar impingement is, therefore, reduced by the cosine of the incident angle with respect to the surface normal. Solar radiation exists within a broad range of the electromagnetic spectrum that includes about 7 % in the ultraviolet wavelength, 46 % visible, and 47 % infrared (IR) radiation. Since solar IR has a shorter wavelength against the satellite

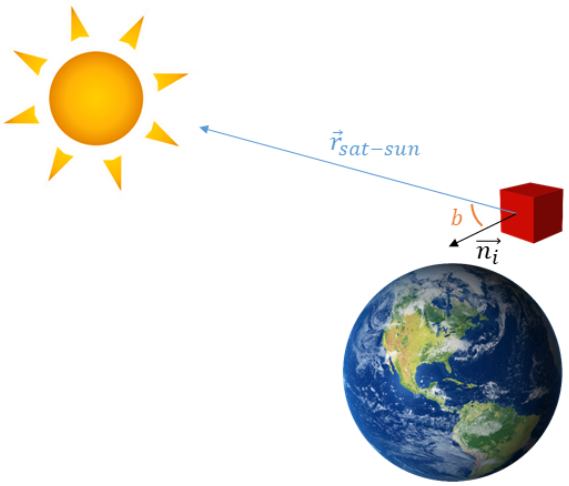

Figure 4.1: Solar radiation and relative angle

emitted IR at normal satellite temperatures, it can be utilized for conditioning a surface to have high reflectivity in the solar spectrum with high emissivity in IR at the same time. This property is reflected in solar absorptivity, α_S, which is the fraction of straight solar energy absorbed by a surface. Therefore, the absorbed solar energy Q_S (W) for a surface of area A, whose normal vector forms an angle b with Sun direction, can be computed using (4.1).

$$Q_S = \alpha_S \, S \, \cos\beta \, A \tag{4.1}$$

Relative geometry between the surface normal and the sun is thus fundamental to obtain the effective value of the impinging flux. In fact, when $cos\, b \leq 0$, the sun rays do not reach the surface, and the actual flux is zero. Also, inside the eclipse zone of the orbit, the solar radiation on a surface will be zero and therefore this has to be taken into account.

4.1.2. Earth Flux

Emitted radiation from the Earth is considered diffuse and equivalent in intensity and wavelength to the heat transferred from a black surface at $-20\,°C$, which gives a nominal value of Earth flux G approximately equal to 236 W/m^2. For this value, a tolerance of $\pm 38\, W/m^2$ is usually imposed in the satellite thermal analysis [14]. Since the Earth radiation is in the same band as that normally emitted by satellite surfaces, the fraction of impinging Earth flux absorbed by the satellite surfaces is given by its emissivity ε. Hence, a surface treatment intended to reflect the Earth's radiation will also reduce the emitted radiation through the same proportion as the surface's emission ability. Besides,

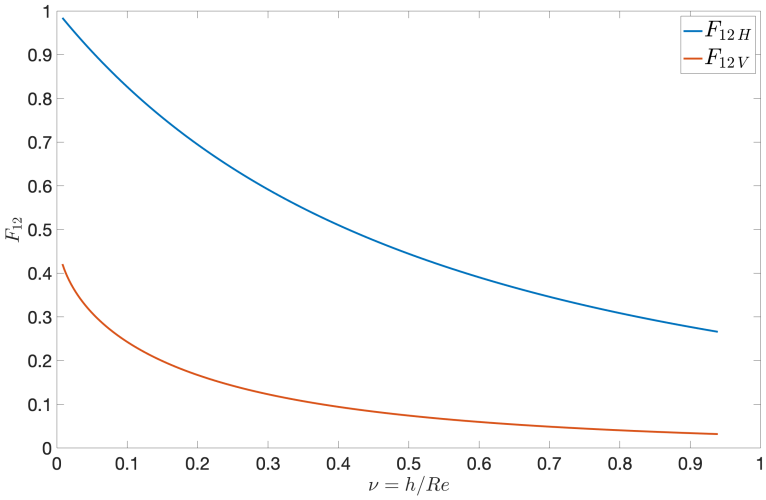

Figure 4.2: Shape factor from a surface element to a sphere

when considering the radiative heat exchange between the Earth and a surface located in space, it is essential to introduce the concept of view factor F_{12}, that is the proportion of the radiation which leaves surface 1 that strikes surface 2. For the specific case of a flat surface in space receiving heat from the Earth, the view factor formulation also called *plate-to-sphere* is usually applied [14]. The latter takes into account the distance, called h, between the plate and the surface of the Earth considered as a sphere and the angle between the surface normal and the vector from the center of the sphere to the plate. In practice, the mathematical formulation of the shape factor for a *horizontal* and a *vertical* element is described in [14], and also reported in (4.2) and (4.4) in their original form, and in (4.3) and (4.5) in the approximated form, which give the trends shown in Figure 4.2 as a function of the ratio between the surface altitude and the radius of the Earth.

The global shape factor is therefore given by (4.6), where δ is the angle between the surface normal and the vector that connects it to the center of the Earth.

$$F_{12\,H} = \int_0^{\arccos(1/(1+\nu))} \frac{\sqrt{1+(1+\nu)^2-2\,(1+\nu)\,\cos\delta-\sin^2\delta}\,(\sin\delta\,\cos\delta-\sin^3\delta)}{(1+(1+\nu)^2-2(1+\nu)\cos\delta)^2} \tag{4.2}$$

$$F_{12\,H} \simeq \frac{1}{(1+\nu)^2} \tag{4.3}$$

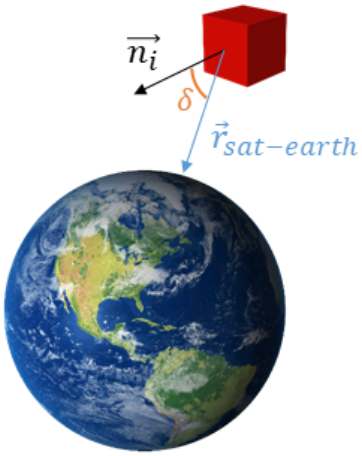

Figure 4.3: Earth flux and relative angle

$$F_{12\,V} = \int_0^{\arccos(1/(1+\nu))} \frac{\sqrt{1+(1+\nu)^2-2\,(1+\nu)\,\cos\delta-\sin^2\delta}\,(\sin^2\delta\,\cos\delta-\sin^4\delta)}{(1+(1+\nu)^2-2(1+\nu)\cos\delta)^2} \tag{4.4}$$

$$F_{12\,V} \simeq \frac{1}{\pi}\left(\arctan\left(\frac{1}{\sqrt{(1+\nu)^2-1}}\right)-\frac{\sqrt{(1+\nu)^2-1}}{(1+\nu)^2}\right) \tag{4.5}$$

$$F_{12} = F_{12\,H}\,\cos\delta + F_{12\,V}\,\sin\delta \tag{4.6}$$

Finally, the actual Earth radiation flux received by a surface in space is given in (4.7).

$$Q_E = \varepsilon\, G\, F_{12}\, A \tag{4.7}$$

4.1.3. Albedo

The reflected heating sunlight from the Earth's surface is called albedo. It is usually considered to be in the same spectrum as solar radiation, so the solar absorptivity is used, and often quoted as a fraction of the solar constant further reduced by geometrical considerations between the satellite surface and the Earth, including the view factor previously described and the so-called albedo reflection angle θ_A. Generally, it is supposed that a

patch on the surface of the Earth reflects light diffusely and equally in all directions. More accurate models use the bidirectional reflectance distribution function employed, for instance, in processing the data provided by NASA's MODIS instruments onboard the Aqua and Terra satellites [6]. The albedo varies considerably across the globe: it is usually higher over areas covered with ice and snow, deserts, and cloudy regions, and generally lower over the oceans, in the absence of clouds [1]. For these reasons, the albedo depends on place and time, but, for simplicity, it is modeled as if it were uniform. NASA has occasionally required using tabulated values for the albedo coefficient f, which were described as a function of the orbit inclination [14]. To model this reflected flux, albedo reflection angle θ_A is used and it is approximated as the angle between the satellite and Sun position vectors with respect to the Earth. Finally, the formulation for this flux is given in (4.8).

$$Q_A = f\,\alpha_S\,S\,F_{12}\,\cos^{1.5}(0.9\,\theta_A)\,A \tag{4.8}$$

In this relation, the angle θ_A is multiplied by 0.9 in order to represent the reality more accurately, according to [17]. When the satellite has passed the line corresponding to the condition $\theta_A > 90°$, it still receives albedo flux from the bright side of the Earth. The albedo flux stops reaching the spacecraft only when $\theta_A > 100°$.

4.2. Thermal Energy Balance

The variation of the satellite temperature T is governed by the first law of thermodynamics for the case in which no work is performed by (or over) the system. Accordingly, the instantaneous rate of change of the satellite's internal energy is equal to the difference between the heat fluxes entering and those leaving it. This results in the differential equation for T reported in (4.9).

$$C\frac{dT(t)}{dt} = -A_{eff}\,\sigma\,T(t)^4 + Q_{tot}(t) + Q_{int} \tag{4.9}$$

Referring to (4.9), the total temperature of the satellite can be recovered by considering all the contributions coming from its faces plus the internal dissipation generated by the presence of electrical components inside the satellite body that will be considered constant. For the radiated heat, i.e. the negative contribution on the right-hand side of the equation, an effective area can be recovered to consider the different thermo-optical properties of the N different surfaces as in (4.10).

$$A_{eff} = \sum_{i=1}^{N} A_i \, \varepsilon_i \tag{4.10}$$

Also, the total heat flux received by the satellite is the sum of all the incoming fluxes previously described received by each surface at each time instant. Then, for each surface the total heat is expressed as in (4.11), and the one to be used in the differential equation is expressed in (4.12).

$$Q_{tot,i}(t) = Q_{S,i}(t) + Q_{E,i}(t) + Q_{A,i}(t) \tag{4.11}$$

$$Q_{tot}(t) = \sum_{i=1}^{N} Q_{tot,i}(t) \tag{4.12}$$

For the resolution of equation (4.9) it is necessary to consider the evolution over time of the satellite position and its attitude configuration to then calculate the relative geometry between the surfaces and the heat sources. Therefore, at each time instant, all the previously described differential equations, now reported in (4.13) without making explicit the time dependence, will be solved.

$$\begin{cases} \dot{\boldsymbol{r}} = \boldsymbol{v} \\ \dot{\boldsymbol{v}} = -\dfrac{\mu}{r^3}\,\boldsymbol{r} \\ \boldsymbol{J}\,\dot{\boldsymbol{\omega}} = \boldsymbol{J}\,\boldsymbol{\omega} \times \boldsymbol{\omega} + \boldsymbol{M} \\ \dot{\boldsymbol{q}} = \dfrac{1}{2}\boldsymbol{\Omega}\, q \\ C\dfrac{dT}{dt} = -A_{eff}\,\sigma\,T^4 + Q_{tot} + Q_{int} \end{cases} \tag{4.13}$$

4.2.1. Thermal Model with Solar Panels

For the resolution of the thermal problem, a *1-node* model has been considered when the analyzed satellite has the solar panels attached to the main body, while a *3-nodes* model is exploited when considering deployable solar panels. More details about these configurations are given in the next chapter. These assumptions are justified by the simple geometries considered in this work, which present very reduced sizes. In fact, the

satellite has dimensions that make it possible to consider that its faces all have the same temperature thanks to heat exchanged by conduction that should homogenize the global temperature of this single thermal node. Clearly, this is an assumption that leads to an important simplification of the analyzed problem. In other words, the transient part of the conductive heat exchange between the satellite surfaces is neglected with a 1-node model. On the other hand, if one wants to neglect the conduction between the surfaces, it is possible to consider each surface as a separate body, thus resulting in a 6-node model. An intermediate case in which the conduction is taken into account with a more reliable model is not analyzed in this work since an accurate thermal analysis of the target is not the main purpose. In fact, a reliable trend of the temperature profile, with reasonable values for a LEO object, is sufficient to proceed with the simulations. This is not the case when two deployable solar panels are considered. In a first estimation, it is assumed that the deployable panels are conductively isolated from the rest of the spacecraft. This simplification is motivated by the fact that we assume a very low thermal conductance for the hinge mechanism linking the solar panels to the structure. This assumption will lead to three different temperature profiles that will be used to calculate three separate infrared signatures that will be then summed up to obtain the overall emission of the target considered as a single entity.

Mathematically, the case with the deployable solar panels is treated in accordance to the equations presented in the following. The main body and the solar panel have to be considered separately and, consequently, the heat equation has to be solved twice. For the main body one can refers to (4.14), while the (4.15) is used for the solar panels.

$$C_{body}\frac{dT_{body}(t)}{dt} = -A_{eff,body}\,\sigma\,T_{body}(t)^4 + Q_{tot,body}(t) + Q_{int} \tag{4.14}$$

$$C_{panel}\frac{dT_{panel}(t)}{dt} = -A_{eff,panel}\,\sigma\,T_{panel}(t)^4 + Q_{tot,panel}(t) \tag{4.15}$$

It has to be considered that, in the case of a geometry like the one just described with deployable solar panels, the notion of shadowing and indirect fluxes should be considered. On the other hand, given that the thermal analysis of the target is not the main purpose of this work and that this phenomena could be negligible under certain conditions, they will not be taken into account for the calculations of the heat flux received by each surface.

Regarding the infrared signature of the target thus defined, one infrared flux will be calculated for the main body and one for each solar panel. At the end, the sum of these contributions will give the total infrared signature of the target (F_{tot}) expressed in (4.16),

where n_{panels} indicates the number of solar panels.

$$F_{tot} = F_{body} + n_{panels} \times F_{panel} \tag{4.16}$$

4.2.2. Cyclic Transient Thermal model

The differential problem described in (4.13) is solved taking into account that, without external perturbations, all the variables that affect the computation of the satellite temperature are supposed to be very similar at the beginning and the end of one orbital period, and consequently so does the temperature. For this reason, we speak about cyclic transient model. It assumes therefore that the conditions encountered at the end of the orbit are the same as at the beginning of this orbit. This hypothesis is especially justified for low Earth orbits (LEO) since the orbital period (T_{orb}) is short compared to external variables like the variation of the Sun's position with respect to the Earth. This is why the majority of the thermal results presented in this thesis are shown for only one orbit.

To mathematically enforce the cyclic condition, two criteria have to be respected:

- The temperatures at the end and beginning of the orbit must be the same:

$$|T(t + T_{orb}) - T(t)| < tol1 \tag{4.17}$$

- The temperature slopes at the end and beginning of the orbit must be the same:

$$\left| \left.\frac{dT}{dt}\right|_{t+T_{orb}} - \left.\frac{dT}{dt}\right|_{t} \right| < tol2 \tag{4.18}$$

This brief algorithm is explained through the scheme presented in Figure 4.4

In this way one can finally extract the temperature evolution within a single orbital period without considering a transient part.

4.2.3. Eclipse

A satellite orbiting earth passes through a shadow region where the solar arrays are deprived of solar illumination. Depending upon the type of orbit, the time duration in the shadow region, called eclipse, varies mainly as a function of altitude, size of the earth, and the orbital beta angle. During this time, satellite surfaces are not reached by sunlight and albedo, therefore, computation of eclipse time becomes very important for

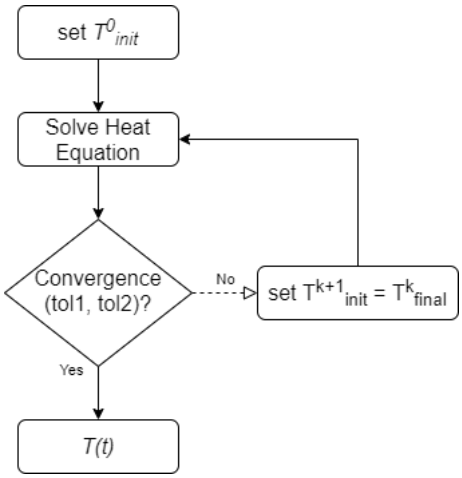

Figure 4.4: Convergence process

precise computation of the temperature profile over time. This region is characterized by two types of shadow conditions called umbra and penumbra. In umbra conditions, the sunlight is considered null, while it is not the case in the penumbra. From previous researches, it was evident that for Low-Earth circular orbits, penumbral duration is very less compared to the umbral duration. However, for high altitude or highly elliptical orbits, the penumbral region cannot be ignored.

For the simulations presented in this work, the algorithm described in [33] has been exploited to recover the eclipse factor. This is zero in the umbra region and between zero and one in the penumbra. This multiplicative factor has then been used to modify the value of solar flux and albedo received by satellite surfaces.

5 | Generation of Simulated Measurements

The first aim of this work is to simulate the acquisition of the incoming electromagnetic radiation of a space target by a ground-based observatory. For this purpose, a study case to deal with has to be defined. Once the data needed to run the simulation are given, the thermal and the radiometric models can be used to get the quantities of interest. The goal of this chapter is therefore to present the context from which the simulated data have been obtained.

5.1. Problem Statement

Many factors play a role in the solution of both the thermal and the radiometric problem. The orbital elements are fundamental to choose relevant constants such as the albedo fraction and to calculate the distance to the observer on the earth's surface. In its motion in the LEO environment, the satellite will also be characterized by a specific attitude that will influence the visibility of the different surfaces with respect to the heat sources and the observer. Then, the geometry of the satellite defines the orientation of each surface in a body-fixed reference frame. Relatively simple geometries will be used for the simulations, but the considerations that will be done can be extended also to more complex geometries because the temperature profile of satellites in the same orbit region is very similar to the one obtained. This is justified by the fact that the materials considered are the typical ones used for satellites in LEO. About this, thermo-optical properties such as the emissivity and the solar absorptivity for each part of the satellite have to be defined.

Some test cases are here considered to simulate the time evolution of the satellite temperature in its motion around the Earth and its consequent infrared signature. Orbits of existing and currently operational spacecraft have been used, while simplified geometries have been considered. A Sun-synchronous orbit, widely used nowadays for earth observation purposes, and an orbit that includes an eclipse region will be treated.

5.1.1. Orbits

For the definition of the test cases at hand, orbits of existing and currently operational satellites have been used. A sun-synchronous orbit has been selected starting from the Two-Line Elements (TLE) of Soil Moisture and Ocean Salinity (SMOS) satellite. An orbit that experiences an eclipse region has been selected by exploiting the TLE of the International Space Station (ISS). Simulations have been performed with the initial time set as the one in which the orbits have been retrieved from [29], that is May 11, 2021. For this date, the orbital elements are reported in Table 5.1.

Simulations will be performed under keplerian assumptions; the simple two-body problem, expressed in (5.1) with $\boldsymbol{r}$ indicating the satellite position and μ the earth standard gravitational parameter, will therefore be solved to recover satellite positions and velocities over time.

$$\ddot{\boldsymbol{r}}(t) = -\frac{\mu}{r(t)^3}\,\boldsymbol{r}(t) \tag{5.1}$$

Orbital element	SMOS	ISS
a [km]	7137.41	6797.97
e [-]	0.0001425	0.0003391
i [deg]	98.44	51.65
Ω [deg]	319.86	69.64
ω [deg]	98.07	47.46

Table 5.1: SMOS and ISS orbital elements

5.1.2. Attitude Modes

Two operational modes have been considered such that the thermal profile and the consequent simulated measurement will refer to a more realistic configuration of the spacecraft. The first mode is the *acquisition* one, and it consists of pointing the face of the satellite that presents the payload opening hole towards the Earth to acquire images or other measurements. The second one is the *idle* mode, during which the satellite points to the Sun to charge its batteries. Finally, a third attitude state has been considered, that is the *tumbling* one. Since a satellite after its operating life is most likely undergoing this type of motion, it is relevant for this work to see the evolution of its temperature profile for

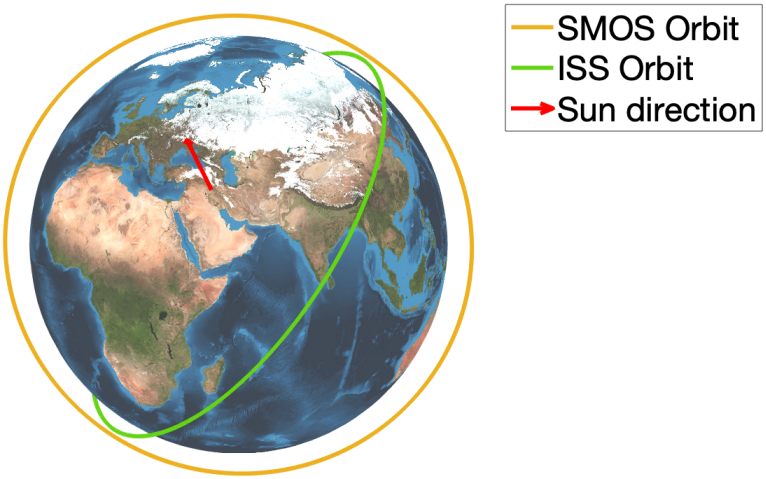

Figure 5.1: SMOS and ISS orbits

that case.

The *acquisition* mode is a simple earth-pointing attitude that is easily defined by pointing one axis of the body-fixed reference frame towards the center of the earth, and therefore along the direction of the position vector at each time instant. The *idle* mode needs a more detailed description. When considering deployable solar panels, this operational mode is simply obtained by giving the satellite an orientation where the Sun rays are perpendicular to the solar panels, which are considered to be co-planar. For a body-mounted configuration, in which three surfaces have been considered as covered with solar cells, the situation is more complex because the solar cells are not all on the same plane. Since the purpose of the sun-pointing mode is to charge the batteries, the spacecraft's attitude has to maximize the power produced by the solar cells. In the case of the cubic geometry, all the three faces with the solar cells have the same size, therefore this configuration is achieved with both an azimuth and an elevation angle equal to 45 °. For the geometry 3U, only the panels located on faces $+X_b$ and $+Y_b$ have the same size, so the optimal orientation will be achieved if the azimuth angle θ (from the x-axis and positive towards y-axis, see Figure 5.2) is 45 °. The maximum power generation is thus achieved with an elevation angle γ (from the XY_b plane and positive towards z-axis) maximizing the equation (5.2) for the 3U geometry developed in [17].

$$Q = 2A_{3U}S\eta\cos\Omega + A_{1U}S\eta\sin\gamma, \qquad \text{with } \cos\Omega = \sqrt{\frac{1-\sin^2\gamma}{2}} \tag{5.2}$$

In this relation, S is the solar constant, η is the solar cells' efficiency, A_{3U} and A_{1U} are

respectively the surface area covered by the solar cells for a 3U and a 1U face. Ω is the angle between the normal of the 3U face and the Sun rays. Finally, the elevation angle γ maximizing the power production is $\gamma = arctan(\sqrt{2}/6)$. It corresponds to the case where the Sun is located in the direction [1, 1, 1/3], in the satellite's axes presented in Figure 5.2.

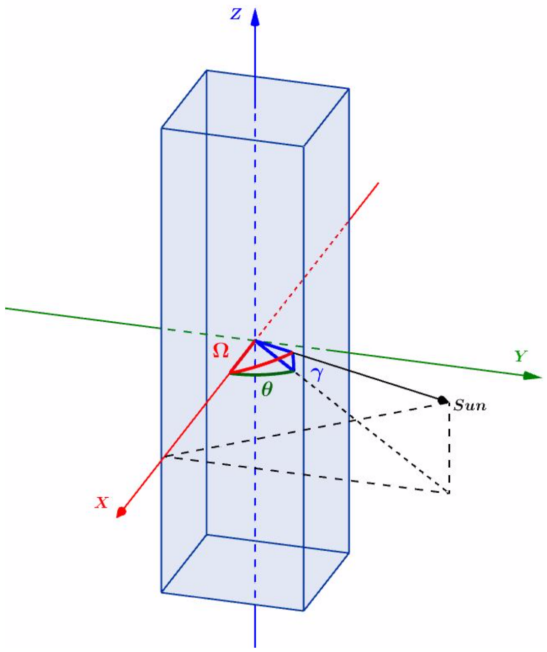

Figure 5.2: Optimal Sun Pointing of the 3U geometry [17]

On the other hand, the *tumbling* motion is obtained by defining a random rotation axis and then the consequent angular velocity vector in the body-fixed reference frame.

5.1.3. Geometries

The two geometries considered for the simulations are relatively simple. Yet, they still allow to perform the analysis of interest for this work. They have been defined by exploiting typical satellite geometries of currently operating missions. The first geometry is a cube whose sizes are $75 \times 75 \times 75\,cm$, with a mass equal to 45 kg. The second is a 3U configuration, whose sizes are therefore $10 \times 10 \times 30\,cm$, with a mass equal to 3 kg. For both geometries, either the body-mounted or the deployable configuration for the solar panels can be considered.

5.1.4. Materials

The materials used in this work are listed in Table 5.2, and they have to be considered as assumptions based on manufacturer data sheets and on other satellites, as explained in [17]. The shear panels are made of alodined aluminum. The coarsest assumption concerns the payload opening holes. Since the role of this component consists of letting light enter the satellite, its reflection coefficient must be small. It is thus chosen to represent it as a black body. Nevertheless, its surface area remains relatively small compared to the whole satellite, meaning that its influence is marginal. This means that the surface containing the payload will not be entirely covered by it. Regarding the solar cells, they are not considered placed directly on their metal support. Instead, an aluminized Kapton film is inserted between the two components, with its aluminized face pointing away from the satellite. This thin film covers entirely the face supporting the solar cells. The patch antennas refer to a GPS antenna from SkyFox Labs and to a communication device that works via S-band. For the thermal analysis, they are considered to have the same properties.

Component	Material	α	ε	Reference
Rails	Al 7075, hard anodized	0.83	0.87	[15]
Solar cell	-	0.72	0.85	[2]
Shear panel (solar cell side)	1 mil aluminized Kapton	0.38	0.67	[8]
Shear panel (other)	Al 6061, alodined	0.44	0.14	[8]
Radiator	MAP PCBE white paint	0.27	0.88	[3]
Payload	black body	1	1	
S-band patch antenna	1 mil aluminized Kapton	0.38	0.67	[8]
GPS patch antenna	1 mil aluminized Kapton	0.38	0.67	[8]

Table 5.2: Thermo-optical properties

After these considerations it is possible to make reasonable decisions about the materials to be used for all test cases. The values reported in the following for absorptivity and emissivity will be the average one, obtained by considering the presence of all the materials on each face. For this reason, a covering factor for each component on each face has to be fixed. So, for example, the faces marked as *solar panels* will have their surface covered mainly by the solar cells and then a smaller part by shear panels and rails. For the sake of simplicity, the most important component present on each face will be used as a reference for identifying it, and the final average values of thermal properties will be given.

The choice of the components and the relative thermal properties have been made based on the orbit on which the spacecraft is placed. They are finally given in Tables 5.3 and 5.4.

Surface	Component	α	ε
+X	Solar panel	0.71	0.84
+Y	Solar panel	0.71	0.84
+Z	Payload	1	1
-X	Antenna	0.44	0.59
-Y	Radiator	0.36	0.88
-Z	Solar panel	0.71	0.84

Table 5.3: Thermo-optical properties: SMOS orbit

Surface	Component	α	ε
+X	Radiator	0.44	0.61
+Y	Antenna	0.44	0.53
+Z	Payload	0.89	0.83
-X	Solar panel	0.71	0.84
-Y	Solar panel	0.71	0.84
-Z	Solar panel	0.71	0.84

Table 5.4: Thermo-optical properties: ISS orbit

Regarding the deployable solar panels, each of them is defined as a two-surface entity. The solar cells are placed on the side exposed to the sun, while a dissipating material is placed on the other one. The thermo-optical properties are given in 5.5.

Surface	Component	α	ε
Sun	Solar panel	0.71	0.84
Anti-sun	Radiator	0.44	0.61

Table 5.5: Thermo-optical properties: solar panels

Finally, by considering the mass, dimensions and materials for the two geometries, a heat capacity equal to $45025\,J/K$ has been chosen for the cube, $3096\,J/K$ for the 3U, and

400 J/K for one solar panel.

5.2. Preliminary Analyses

Once the problem to solve has been defined and the needed data has been provided, the simulations can be run. Before moving to a deeper and more complex analysis of the simulated measurements, it is possible to extract some preliminary considerations starting from a visual analysis of the figures of some test cases. In the following, considerations about the infrared signature of the target will be given for different configurations of the variables present in the problem. The SNR is calculated with a step time equal to 1 second (value to be selected according to the working principle of the selected instrument).

5.2.1. Temperature Profile

The first step for the simulation of the measured flux of the target is the computation of the temperature evolution over one orbital period. For this reason, this variable is computed at the beginning of each simulation and is then used within the calculations of the radiometric chain. As an example of the behavior of this variable, here are reported the cases of both the orbits with each of the three attitude modes and the resulting temperature profile for the main body of a cubic geometry on the left and for a single solar panel on the right. In Figure 5.3 there is the case of the ISS orbit, while the case of the SMOS orbit is shown below in Figure 5.4.

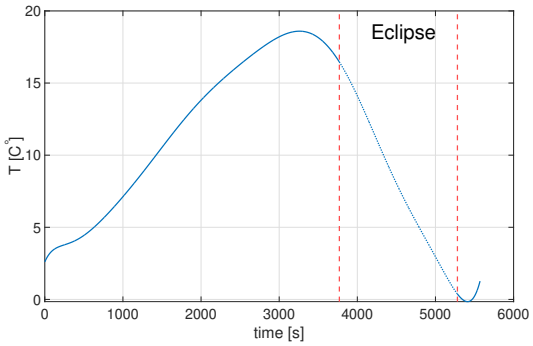

(a) Body temperature: earth-pointing

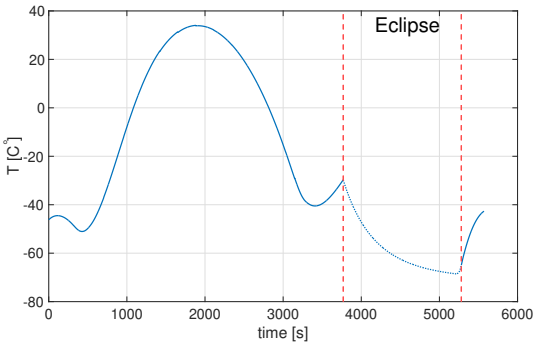

(b) Panel temperature: earth-pointing

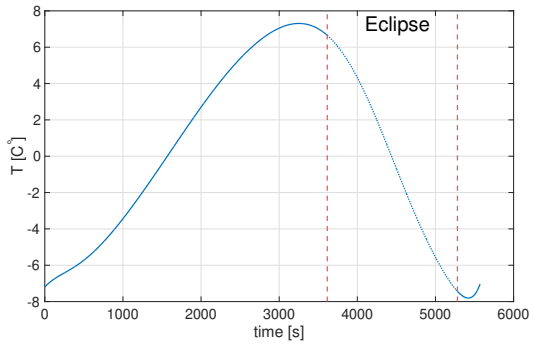

(c) Body temperature: sun-pointing

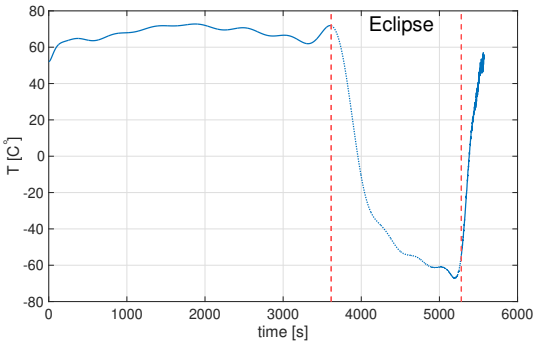

(d) Panel temperature: sun-pointing

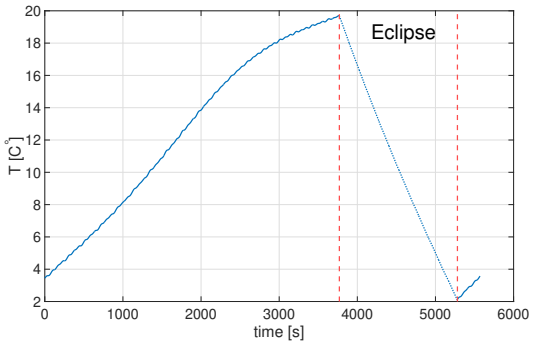

(e) Body temperature: tumbling

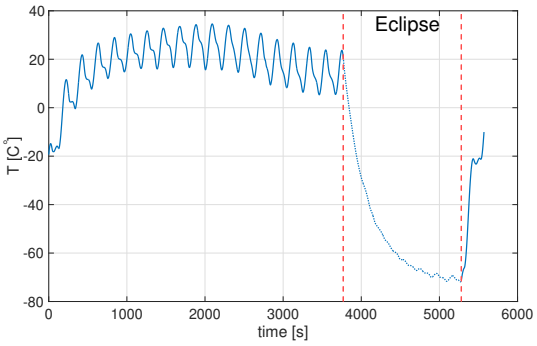

(f) Panel temperature: tumbling

Figure 5.3: Temperature profile: ISS orbit

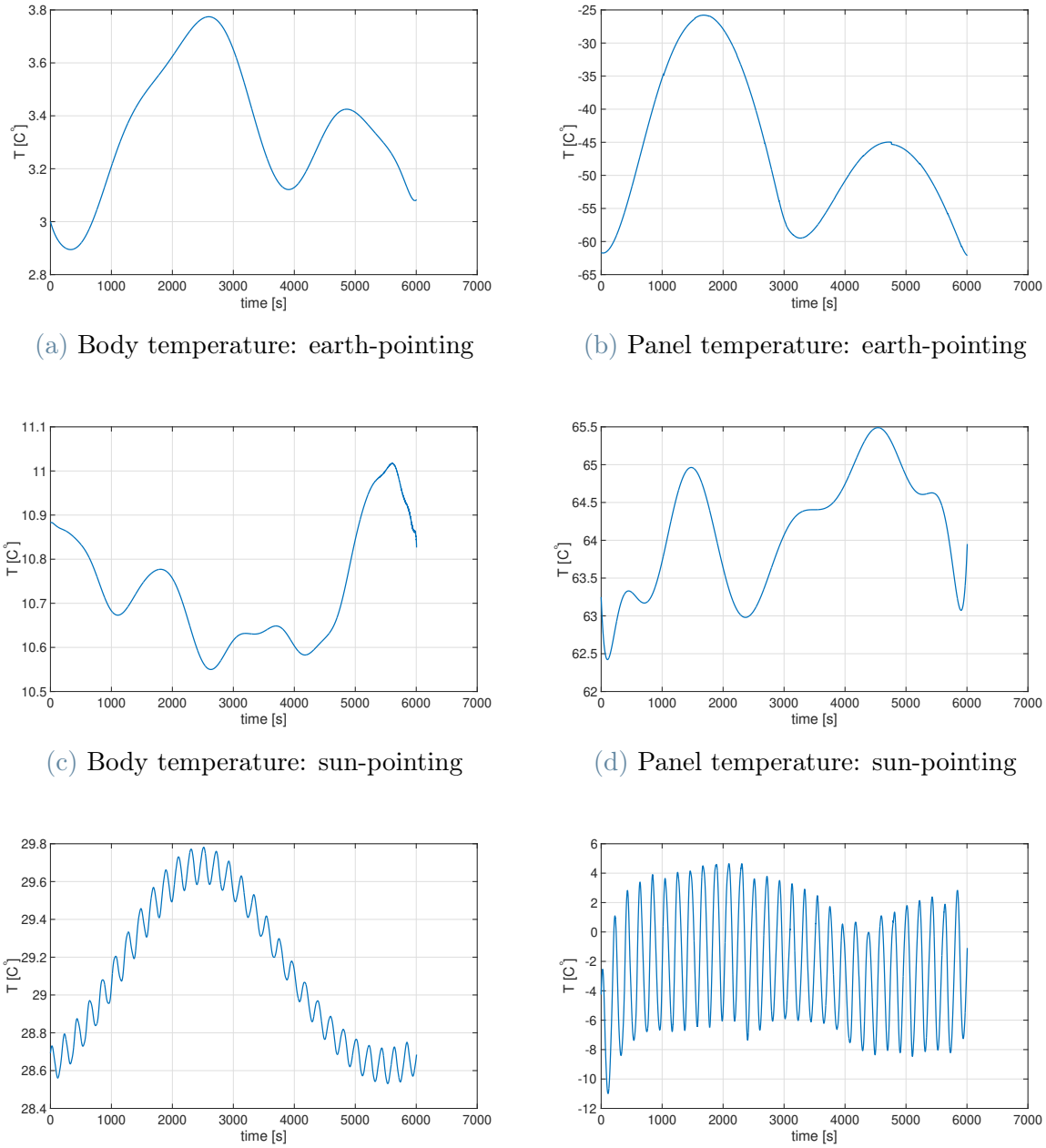

(a) Body temperature: earth-pointing

(b) Panel temperature: earth-pointing

(c) Body temperature: sun-pointing

(d) Panel temperature: sun-pointing

(e) Body temperature: tumbling

(f) Panel temperature: tumbling

Figure 5.4: Temperature profile: SMOS orbit

Concerning the temperature profile of the target on the ISS orbit, it is possible to highlight the behavior of this variable during the eclipse phase, denoted by two red dashed vertical lines. As it is possible to notice from the plots, during the eclipse phase the satellite experiences a relevant reduction of its temperature due to the absence of both solar radiation and albedo flux. In addition, it is interesting to underline that the satellite does not have the time to reach a sort of steady-state condition during the eclipse phase. This

is due to the value of the heat capacity that affects the satellite's thermal inertia and, i.e. its ability to change its temperature due to external actions.

About the temperature profile of the target placed on the SMOS orbit, one can immediately notice the slight quantitative variation of the temperature (in the order of the degree) over one orbital period. This is expected because of the sun-synchronous condition of the trajectory, which generates a constant illumination of the target by the sun. Finally, it is important to remark the presence of strong short-period oscillation generated by the tumbling motion of the satellite. This condition causes a continuous variation of the relative configuration between the satellite's surfaces and the heat sources.

5.2.2. Observations along the Orbit

The first considerations concern the differences between the measurements acquired while the satellite is in different parts of its orbit. To do so, it is necessary to place different ground-based stations on the earth's surface to be able to observe the target in correspondence with these different segments. For the purpose of this analysis, some real and non-real observatories were used, denoted as OBS1, OBS2 and OBS3. This survey is of interest for different reasons. The temperature of the target is a time-dependent variable, and therefore it will affect differently the acquired measure as a function of the time of the observation. In addition, in the case of Sys3 instrument working in the LWIR region, the quantity of interest is the infrared emission of the target, which is not dependent on the illumination condition but only on the relative configuration between the satellite and the heat sources. Therefore, the measurements can be theoretically acquired also during the eclipse region of the orbit when dealing with that sensor.

To extract the information of interest, the measure has been obtained for all the possible configurations of the problem variables, i.e. for the two orbits, the two geometries with and without the deployable solar panels, and the three attitude modes. For the sake of brevity, only some representative cases will be shown. In particular, one case for the sun-synchronous orbit and one for the orbit with eclipse are presented. In Figure 5.5 the case of the ISS orbit, with the Sys3 instrument, with the cubic geometry with deployable solar panels in the tumbling motion is shown. In Figure 5.6 the case of the SMOS orbit, with the Sys2 instrument, with the 3U geometry with deployable solar panels in sun-pointing configuration is shown. In Figure 5.7 the case of the ISS orbit, with the Sys1 instrument, with the 3U geometry with deployable solar panels in earth-pointing configuration is shown.

Looking at the first two cases, it is possible to remark that, under favorable illumination

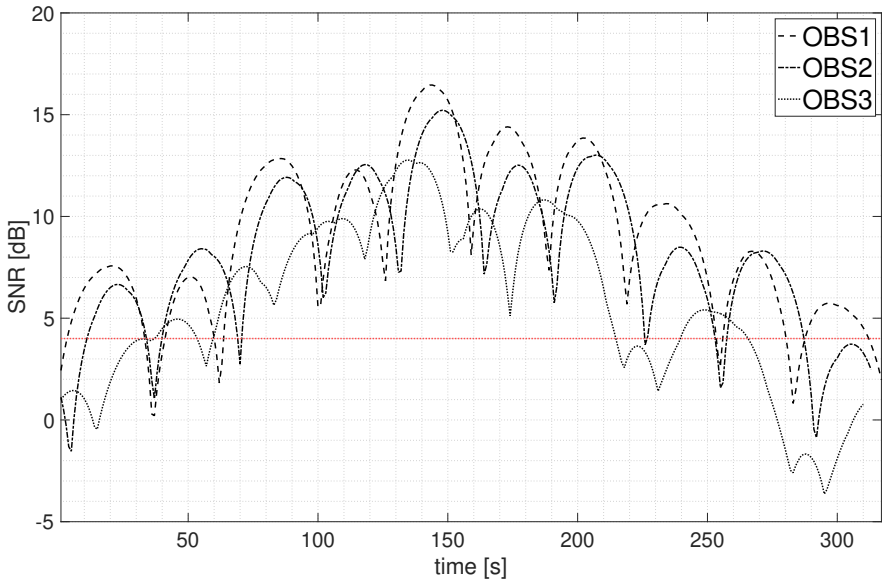

Figure 5.5: SNR from multiple observation sites with Sys3: tumbling motion

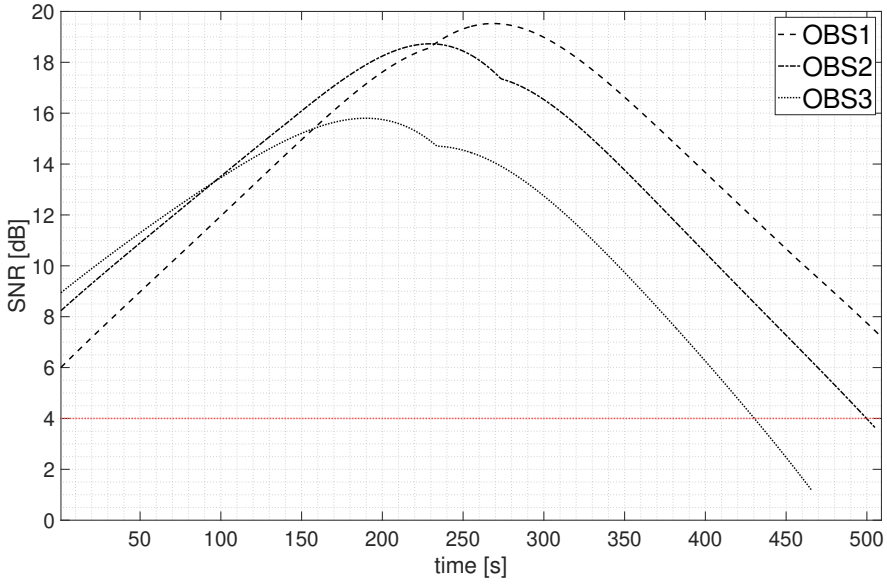

Figure 5.6: SNR from multiple observation sites with Sys2: sun-pointing

conditions, the behavior of the time evolution of the measured quantity does not show relevant differences depending on the observation point on the earth's surface. It has to be highlighted that the Sys1 and Sys2 instruments work in the visible and NIR/SWIR regions where the emitted component is negligible compared to the reflected one. In fact, in the third case, where Sys1 is used, during the passage of the target above OBS3, the satellite is in the eclipse phase and there is the lack of the reflected component of the

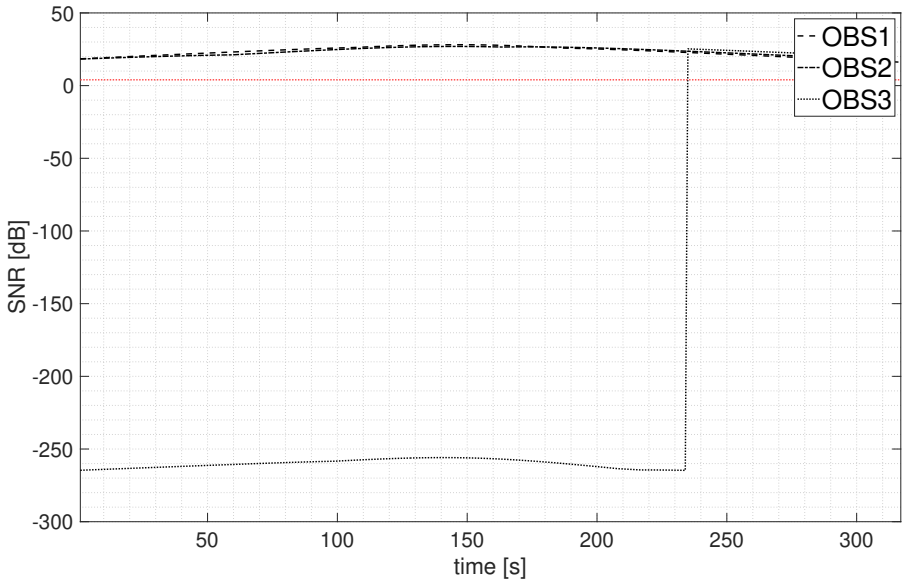

Figure 5.7: SNR from multiple observation sites with Sys1: sun-pointing

acquired measure that makes the SNR significantly decrease. Only at the end of the passage the eclipse region ends and the satellite is again lit by sun rays that allows the acquisition of the reflected component of radiation.

Always regarding the eclipse phase, it is possible to notice that the curve acquired during the eclipse region of the orbit, does not show relevant differences for the case of Sys3 instrument show in Figure 5.5. This leads to the first remark that this measurement can be acquired also in this non-illuminated phase since the intensity of the measured emitted component in this wavelength range is high enough to allow a SNR higher than the detectability threshold.

5.2.3. Comparison of Attitude Modes

Once the behavior of the simulated measurements along the orbit has been analyzed, it is now possible to focus on the shape of the SNR evolution over time when different attitude modes are simulated. In particular, by considering the ISS orbit and the Sys3 instrument, the cubic geometry with deployable solar panels is observed from a single observatory.

By referring to Figures from 5.8 to 5.10, an important aspect can be noted. The difference between a stable operational mode, i.e. the earth-pointing and the sun-pointing ones, and an unstable one, is already clear from the shape of the curves shown in the plots. This was one of the key points of this work. The main interest was to understand if this kind of measurements were able to convey this preliminary information. Then, to extract more

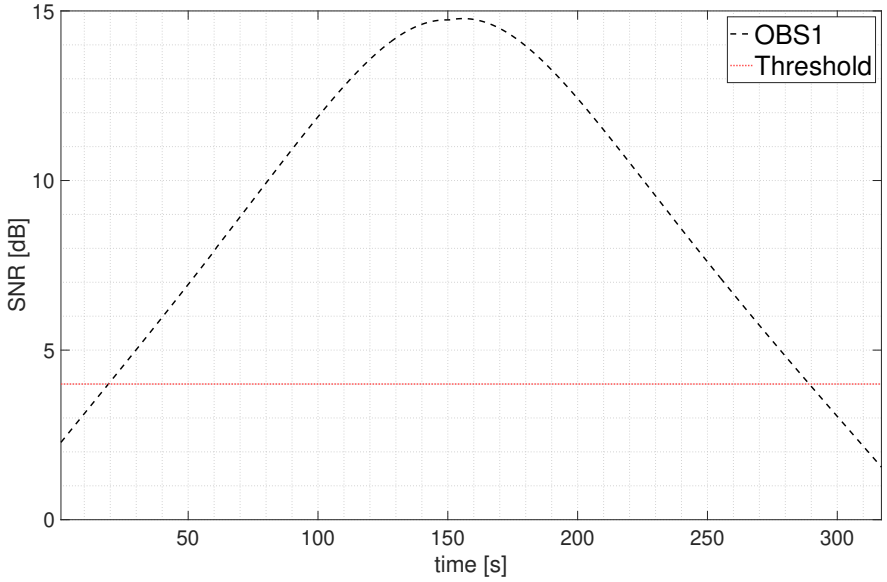

Figure 5.8: Earth-pointing

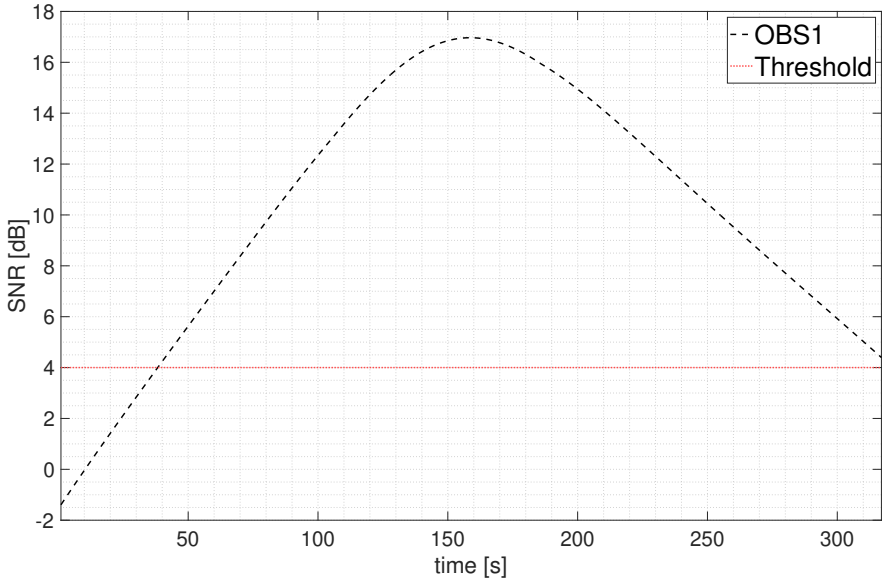

Figure 5.9: Sun-pointing

precise and interesting information from the data available, it could be useful to use some particular tools that are capable of obtaining, for instance, an estimate of the quantities related to the attitude of the target.

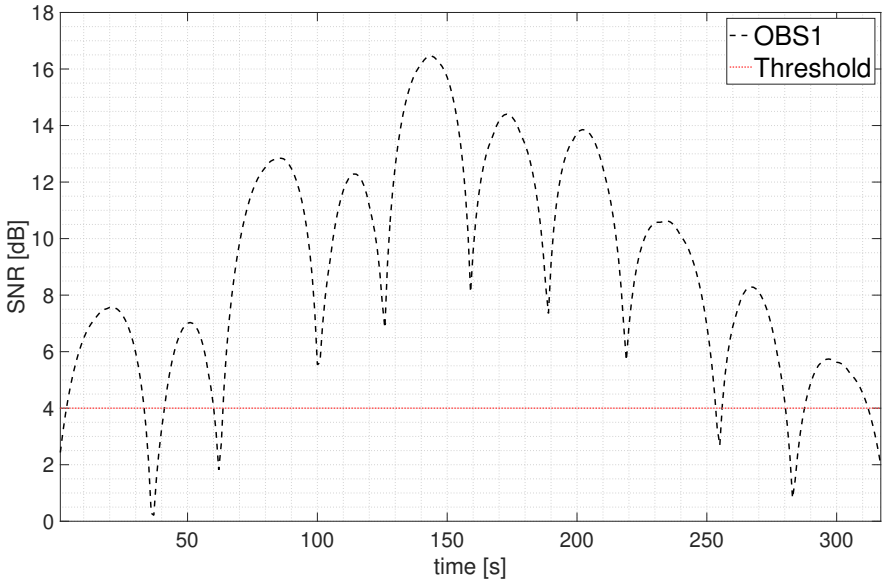

Figure 5.10: Tumbling motion

6 | Analysis of Simulated Measurements

Once the simulated measurements have been acquired, one can move forward and exploit the available data to extract more information and make more reliable considerations about the state of the observed target. This is a fundamental part to understand the potential of this observation strategy and therefore the role it could play in the context of SST.

In order to pursue the objective of these analyses, the simulated measurements were modified by adding some noise to better represent a realistic case, whereas in previous cases they were presented without the noisy part. More specifically, once the SNR is calculated according to the radiometric chain equations, the noisy part was modelled as a white noise and thus was considered as a Gaussian random variable with zero mean and a standard deviation equal to 0.1.

6.1. Estimation Methods

As already anticipated at the beginning of this document, the aim is to retrieve information related to the attitude variables and the thermo-optical properties of the materials of the observed target. For this purpose, two different methods have been exploited and they both need the definition of the independent variables to be optimized in order to find a estimate of the variables of interest. The first is the non-linear least-squares algorithm and the second is the MultiStart algorithm implemented in MATLAB.

In order to simulate a realistic context, one must distinguish between known and unknown quantities. To make this distinction, it is necessary to consider a possible application of the problem and to identify the information available to the user when the measurements are acquired. More specifically, considering the system of equations in (4.13), satellite position and velocity are considered as known variables of the problem, even if affected by uncertainties compared to their actual values, while the unknowns are the attitude

variables, i.e. the angular velocity and the Euler angles, the emissivity and reflectivity of the materials and a temperature for each thermal node considered constant for the observation time. All other parameters in the simulation, such as the constants needed to calculate the heat fluxes, are considered known.

Regarding the temperature, it is a fundamental variable in the simulation of measurements in the case in which the emitted component of the incoming radiation is much larger than the reflected one. It will be considered as an unknown of the problem, but one has to consider the specific role it plays in the calculations to decide how to deal with it. In fact, the temperature is used in the radiometric chain to recover the radiance, i.e. the radiation emitted by the target as in (3.6). The time-varying information contained in this variable is then integrated, and its contribution does not affect significantly the resulting measured flux in a qualitative sense. Furthermore, in the short duration of the observation intervals, its range of variation is limited and the integral over the wavelength of interest does not preserve the time-varying behaviour. In practice, this means that one can consider a value of the temperature for each thermal node that is maintained constant for the entire observation time as an additional unknown. This will clearly lead to errors in the estimation of the variables of interest, but this is justified by the reasonable assumptions that considerably simplify the calculations compared to the possibility of considering the entire time evolution of the temperature as an unknown to estimate.

A more realistic application is to simultaneously research the satellite's attitude and the composition of its materials in terms of emissivity and reflectivity. This is the fundamental information one wants to extract from ground-based observations of the space objects. In fact, for the operating satellites, the orbital knowledge can be considered available with high precision, while the data related to the attitude and the material properties can be unknown. The satellite attitude motion can vary over time because of external perturbation and can no more be aligned with the initial requirements. Precise information about the thermo-optical properties of the materials composing the satellite surfaces is not always available since the coatings can be subjected to degradation and erosion. These phenomena can vary the properties of the satellite's surfaces leading to different thermal conditions of the target. For this reason, based on the existing relationship between these quantities and the available measurements, one can try to apply the selected methods to retrieve this information, thus augmenting the vector of the unknowns.

The independent variable that will be optimized to find the best fit with the provided measurements is the composition of a six-element vector containing the initial conditions of the six attitude variables, together with 2 temperatures for the two thermal nodes for each observation time considered, the 8 emissivity values and the 8 reflectivity values (6

faces of the main body plus 2 faces of one solar panel). The terms "initial" refers to the first time instant of the first observation.

The vector containing the unknowns is defined in three different ways depending on the specific application. In fact, for a first and easier test case, only the attitude variables and temperatures will be considered unknown, thus resulting in the vector shown in (6.1), where the subscript 0 refers to the first time instant of the observations. In the case of multiple measurements acquired from multiple observation sites, which will be later explained, there will be six unknown temperatures: one for the main body and one for a solar panel for each of the three observation interval.

For the estimation of the thermo-optical properties, when a single instrument is considered, the measurements will be acquired with Sys3. As a consequence, those measurements will be almost independent on the reflectivity values because the reflected component of the incoming radiation is negligible compared to the emitted one, and therefore the vector is the one presented in (6.2). When Sys1 and Sys2 are used, the reflectivity values are added, as in (6.3).

$$\boldsymbol{x} = \begin{bmatrix} \omega_{0x} & \omega_{0y} & \omega_{0z} & \phi_0 & \theta_0 & \psi_0 & \bar{T}_{body} & \bar{T}_{panel} \end{bmatrix} \tag{6.1}$$

$$\boldsymbol{x} = \begin{bmatrix} \omega_{0x} & \omega_{0y} & \omega_{0z} & \phi_0 & \theta_0 & \psi_0 & \bar{T}_{body} & \bar{T}_{panel} & \boldsymbol{\varepsilon} \end{bmatrix} \tag{6.2}$$

$$\boldsymbol{x} = \begin{bmatrix} \omega_{0x} & \omega_{0y} & \omega_{0z} & \phi_0 & \theta_0 & \psi_0 & \bar{T}_{body} & \bar{T}_{panel} & \boldsymbol{\varepsilon} & \boldsymbol{\rho} \end{bmatrix} \tag{6.3}$$

The attitude variables at the first time instant of observation will then be used to perform a numerical integration by assuming a non-perturbed attitude dynamics of the target. Once the time evolution of all the state variables is available, the operations of the radiometric chain can be performed and the estimated curve is recovered. This is compared with the measured curve by the algorithm, which then evaluates a cost function and updates the value of the independent variable to find a better fit.

In the following, the use of the algorithm is analyzed in the case of the three attitude modes, and the performances are evaluated both qualitatively and quantitatively.

6.1.1. Non-linear least-squares

For the problem at hand, the non-linear least-squares method (LS) could be a valid tool to process the available measurements to retrieve specific information. There is a set of m observations that one can try to fit to reconstruct the time evolution of the satellite attitude by exploiting the vector of unknowns previously defined. The algorithm will take an initial guess of the solution and will refine it trying to obtain the best fit with the provided measurements.

The choice of the first guess to start the calculations is very important and therefore it has to be chosen such that it is as close as possible to the final solution. In some cases, the first guess can be chosen according to some information of the problem to be solved. In particular, for the cases of this work, there is a net distinction between the curves associated with a stable or an unstable attitude motion. Consequently, for the stable case, it is possible to wisely choose the first guess. Specific details about this concept will be given in the section dedicated to each attitude mode.

In the presentation of the results, the uncertainties defined at the start time of the observations and related to the estimated attitude variables will be shown in tables in terms of standard deviation. Once the covariance matrix is calculated as shown in Chapter 2, the standard deviations associated to the attitude variables are extracted from its diagonal terms.

$$\sigma_i = \sqrt{C_{ii}} \tag{6.4}$$

6.1.2. MultiStart Algorithm

This method could help to overcome the need of providing a valid initial solution at the beginning of the optimization routine. In this way, one does not have to make strong assumptions to find an acceptable first guess. The MultiStart procedure, capable of running optimisation algorithms in parallel using a large number of different starting points, is therefore exploited to better explore the solution space and find a valid solution. In this way, a more realistic situation could be analysed and it is also possible to make interesting comparison between two different methods.

6.2. Estimation Strategies

Once the methods to identify an estimate of the variables of interest have been chosen, it is possible to define a possible strategy to decide how to exploit the information contained in the simulated measurements. As anticipated in the introduction, there an increasing interest in the use of combined measurements to try to retrieve more precise estimate of specific quantities. For this reason, two strategies will be analysed. The first involves the use of multiple observation sites in order to combine the information coming from different time intervals. The second will make use of a single observation point where all the three instruments have been placed in order to combine measurements coming from sensors that work in different wavelength bands. For each strategy there will be a comparison with the case of a single observatory that uses a single instrument.

6.2.1. Strategy 1: Multiple Observations

Two different applications have been tested and their performance in the estimation of the satellite attitude has been evaluated. More specifically, three observatories referred to as 1, 2, and 3, have been placed such that the target would be visible from all of them during one orbital period, as shown in Figure 6.1. The instrument Sys3 has been used for all the observatories.

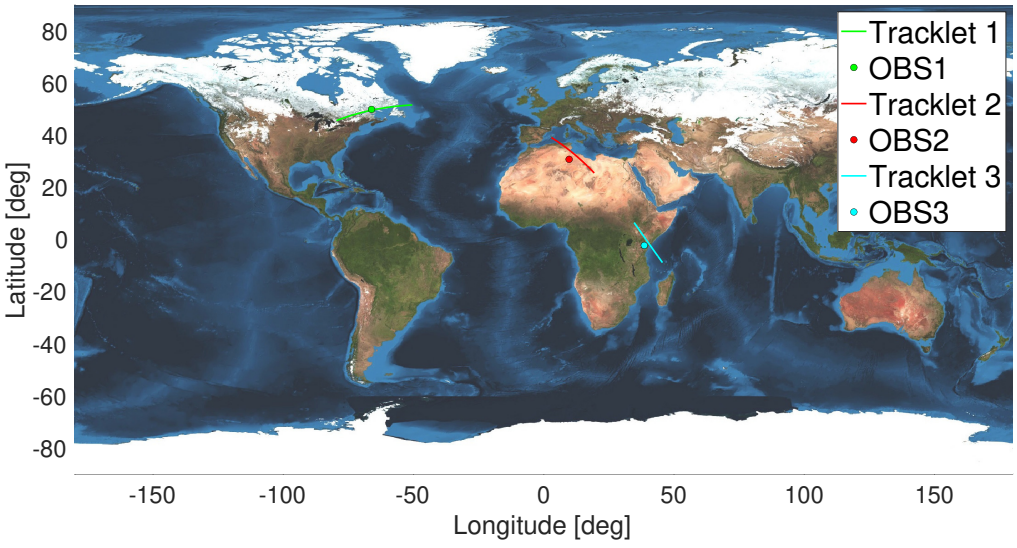

Figure 6.1: Observatories 1, 2 and 3

Then, one use case, called single observation (SO), consists in considering only the measurement acquired by Observatory 1 to use the non-linear least squares method and to find a solution for the satellite attitude. The idea of the other use case is based on the use of multiple observations (MO) to better constrain the problem and try to improve the convergence of the algorithm towards a more precise solution. This is based on the idea that the algorithm is forced to consider a solution for the attitude variables that minimizes also the deviation from the other measurements, acquired by Observatory 2 and 3. For this reason, in the first case, the equation of the satellite dynamics is integrated over the observation period of the first curve, while in the second case it starts at the first time instant of the first observation and ends at the last time instant of the last observation. These two time spans are therefore defined in the following way:

$$\Delta t_{SO} = \left[t_i^{OBS1}; t_f^{OBS1}\right] \tag{6.5}$$

$$\Delta t_{MO} = \left[t_i^{OBS1}; t_f^{OBS3}\right] \tag{6.6}$$

To graphically evaluate the results found by the two applications, the solution, i.e. the initial condition of the attitude variables, is used in both cases to calculate the estimated curves in correspondence with the visibility intervals of the three observatories and then plotted together with the simulated measurements. To quantify the goodness of the results for the two cases, the percentage errors in the estimation of the variables of interest and the MSE are used and reported in tables. In the MO case, MSE is obtained directly from the objective function of the used procedure, as all three curves are used to find an optimal solution. In the SO case, only the first curve is used to fit the data, but the resulting solution is then used to calculate the estimated curves for the three observation time intervals, and thus the distance between the three curves can be calculated providing the sum of the residuals and therefore the MSE.

6.2.2. Strategy 2: Multiple Instruments

In the second strategy only Observatory 2 is used as observation point being that it is outside of the eclipse region. In this way, the instruments Sys1 and Sys2, which are more sensitive to the reflected component of the incoming radiation, can acquire useful measurements. The Multiple Instruments (MI) applications simulates the presence of the three sensors in the same observatory, while the Single Instrument (SI) makes use of only Sys3. In the MI case, the measurements acquired by the three sensors are given to the

LS algorithm to find a solution for the attitude variables and the material properties. On the other hand, the SI application uses only the information coming from Sys3, but the solution found by the algorithm is used to calculate the estimated measurements as if they were acquired by Sys1 and Sys2 to make a comparison similar to that shown for the first strategy.

An important difference with respect to the previous strategy is the change of the vector of unknowns. First of all, only one observatory and one time interval are considered and, therefore, only one value for the temperature for each thermal node is present among the unknowns. Previously, in the MO application, the temperature of each thermal node was added as an unkonwn for each of the three time intervals, thus leading to six unknown temperature values. In addition, for the estimation of the material properties, in strategy 1 there was not the need to estimate the values of reflectivity, being that the reflected component of the incoming radiation was negligible for Sys3, and therfore those variables did not give a contribution to the objective function. In fact, for the SI application, it is still not possible to obtain an estimate for the reflectivity values. However, they will be added to the vector of the unknowns leading to a total of 24 variables for the materials properties case.

The results will be presented in the same way as for strategy 1, with tables reporting percentage errors and MSE. Also, the considerations about the first guess to provide to the algorithm are still valid.

6.3. Test Cases and Results

The strategies to recover and then analyse the simulated measurements have been defined and will be used for the case of the cubic satellite placed on the ISS orbit in the three attitude configurations. As anticipated, for each test case, two applications have been considered. For the first one, only the attitude variables have been considered unknown, while for the second one the thermo-optical properties have been added. For the sake of conciseness, only one test case is shown for each attitude motion this chapter, i.e. one strategy and one method are selected to analyse the curves and retrieve an estimate of the variables. All the possible combinations of strategies and methods have been examined and a complete version of the results are reported in appendix.

6.3.1. Earth-pointing Curves

For what concerns a possible first guess in the earth-pointing case, one can start from the orbital knowledge to recover the attitude configuration corresponding to pointing towards the center of the earth. In this way, the initial solution given to the algorithm should be very close to the real one and, consequently, the time needed for the optimization routine should be reduced and the quality of the final solution increased. To find this initial guess, one can easily start from the position $\boldsymbol{r}_0$ and velocity $\boldsymbol{v}_0$ of the satellite at the initial time of observation and use them to calculate the orbital angular momentum $\boldsymbol{h}$ through their cross product. Then, these two vectors can also be used to recover the rotation matrix of an earth-pointing reference frame, such as the LVLH or the TNW, which has been previously defined. Finally, from the rotation matrix, one can extract the corresponding Euler angles, and then one can use it to rotate the orbital angular momentum vector in the body-fixed reference frame to get the body angular velocity. These six elements will describe a pointing of one face of the satellite towards the center of the earth for that precise time instant and will be used as the first solution for the algorithm.

In practice, once the measurements are available, the user can identify the stable nature of the motion of the observed target and therefore try to use a reasonable first guess for the selected algorithm. Clearly, this first step would make the search of a good estimation of the attitude variables slower but even more reliable. For brevity reasons, a valid initial solution has been used for the application of the LS algorithm.

For this attitude configuration, the case of strategy 1 with the use of the LS method is reported. In Figure 6.2 the results for the SO case are compared to the MO case for each observatory. One can immediately notice that the quality of the results is quite high for both applications in the case of Observatory 1. It is evident that, in the MO case, the estimated curves have a better match with the measured ones and this, therefore, highlights the importance of combining this information to get a better estimate of the attitude variables. This good match also led to quite satisfying results in terms of attitude determination, especially for the MO case. This means that, given the quality of the initial solution provided to the LS algorithm, the information of interest is recovered with good accuracy and a relatively reduced computational effort thanks to this well-validated tool.

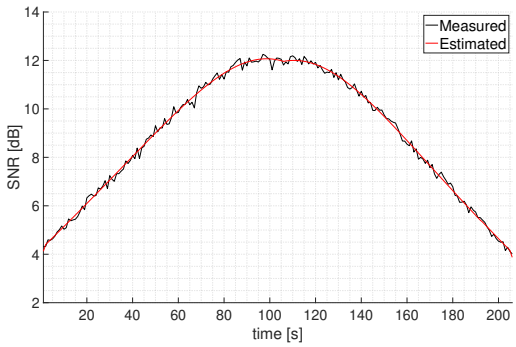

(a) SO: Observatory 1

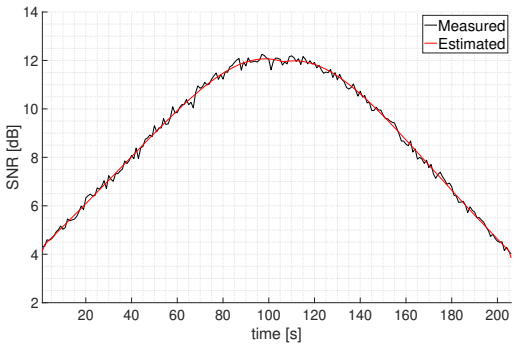

(b) MO: Observatory 1

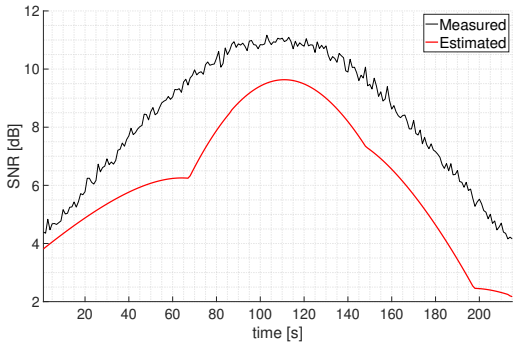

(c) SO: Observatory 2

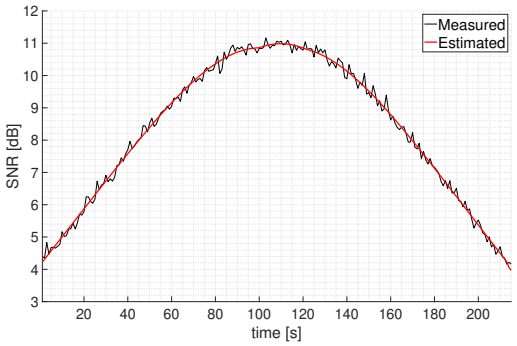

(d) MO: Observatory 2

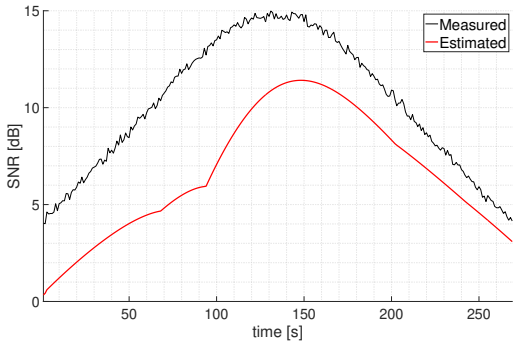

(e) SO: Observatory 3

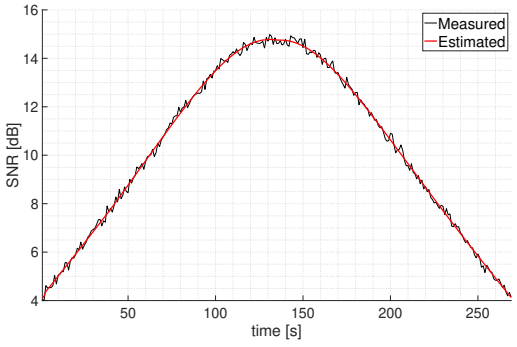

(f) MO: Observatory 3

Figure 6.2: Comparison SO - MO: earth-pointing

Variable	True	Estimate SO	Err% SO	Estimate MO	Err% MO
ω_x	0	$\sim$0	-	$\sim$0	-
ω_y	-0.0647	-0.166	158.45	-0.0573	10.69
ω_z	0	$\sim$0	-	$\sim$0	-
ϕ	133.50	125.48	6.03	141.52	5.69
θ	136.94	99.69	27.05	130.06	4.89
ψ	155.27	171.31	10.47	178.76	15.06

Table 6.1: LS - S1 - Percentage error on attitude variables: earth-pointing

Uncertainty	SO	MO
σ_{ω_x} [deg/s]	9.763×10^{-2}	4.215×10^{-3}
σ_{ω_y} [deg/s]	8.170×10^{-2}	1.150×10^{-3}
σ_{ω_z} [deg/s]	3.537×10^{-1}	6.140×10^{-4}
σ_ϕ [deg]	26.91	4.43
σ_θ [deg]	23.40	1.41
σ_ψ [deg]	30.30	1.91

Table 6.2: LS - S1 - Uncertainties on attitude variables: earth-pointing

Variable	True	Estimate SO	Err% SO	Estimate MO	Err% MO
$\bar{T}_b$ 1	275.25	289.83	5.30	283.43	2.97
$\bar{T}_p$ 1	205.18	243.08	18.47	231.78	12.96
$\bar{T}_b$ 2	275.62	289.83	5.15	293.57	6.51
$\bar{T}_p$ 2	222.47	243.08	9.26	246.69	10.89
$\bar{T}_b$ 3	279.57	289.83	3.67	293.51	4.99
$\bar{T}_p$ 3	276.79	243.08	12.18	300.69	8.64

Table 6.3: Percentage error on temperatures: earth-pointing

Surface	SO	MO
+X	41.91	0.23
+Y	89.39	0.43
+Z	39.62	1.70
-X	8.68	0.12
-Y	99.99	0.44
-Z	40.16	40.16
Sun	40.16	40.16
Anti-sun	17.83	1.94

Table 6.4: LS - S1 - Percentage error on emissivity: earth-pointing

	SO	MO
Attitude	7.518	2.452×10^{-3}
Materials	8.043	2.810×10^{-3}

Table 6.5: LS - S1 - MSE earth-pointing

An interesting remark can be made by looking at the values of the percentage errors in Table 6.4. Firstly, the surfaces -Z and the one called "Sun" are covered by solar cells. The interesting aspect that could be highlighted is that, in both SO and MO cases, the errors given by the difference between the real value and the estimated one are the same. This is because these two surfaces are not visible to the ground-based observer for the entire observation time, since in the earth-pointing case the +Z face is supposed to carry the instrumentation that has to point to the surface of the earth, and therefore the opposite faces never enter into visibility. This means that, during the computations performed inside the LS routine, these two values are never used because they do not contribute to the emission of the target towards the sensor, and therefore they were never modified to try to reach a better fit with respect to the initial solution provided to the algorithm. In other words, the algorithm does not find a benefit from varying these emissivity values because they do not lead to a variation in the objective function.

From this first application of the LS method, it is already possible to highlight the importance of combining the measurements coming from different observatories to obtain a more accurate estimate of both the attitude variables and the emissivity values. As already stated, the algorithm is forced to find a solution that fits the curves acquired in

the three time intervals and therefore it is able to find a solution that leads to a lower value of the MSE metric.

Another point to remark concerns the temperature, since it is important to notice that Observatory 1 sees the target during its eclipse phase. This means that the temperature of each thermal node is lower compared to the values reached in the illuminated region. This condition leads to an higher error in the case of SO application because the algorithm does not try to find a value for the temperatures that could allow a better fit with the measurements of Observatory 2 and 3. The values of the temperatures found for Observatory 1 are then considered the same for the other two observation intervals, thus leading to a larger distance between the estimated and the measured curves being that the Sys3 instrument works in the wavelength band where the emitted component is more important than the reflected one. With the use of one of the other two instruments, it would not have been possible to acquire the measurement during the eclipse phase and, in addition, the temperature of the target would not have played an important role. This means that an incorrect estimate of this variable would not have significantly affected the quality of the results.

Finally, an interesting consideration can be made by observing the results of the SO case. It is possible to notice that the match of the estimated curve with the measured one is very accurate for observatory 1. Despite this, the accuracy of the estimated variables is low and it has been highlighted thanks to their propagation in the visibility intervals of observatories 2 and 3. This condition could lead to the conclusion that, with the addition of other variables to optimize, i.e. the thermo-optical properties, the algorithm is looking for a solution in a larger solution space where ambiguous curves, i.e. very similar to the measured ones, could be found.

6.3.2. Sun-pointing Curves

For the sun-pointing case, it is possible to assume that the target has a zero angular velocity in the body-fixed reference frame since it has to point in the fixed direction of the sun. On the other hand, nothing can be said about the Euler angles starting from the knowledge of the satellite position and velocity. For this case, the attitude of the satellite is driven by the need of pointing the solar panels towards the direction of the sun and, therefore, one cannot suppose a particular value for the Euler angles since the observer could not know on which of the satellite surfaces these components are placed.

For all these reasons, the initial guess provided to the algorithm has three zeros for the components of the angular velocity, while to identify a good initial value for the three

Euler angles it is possible to follow a different strategy. One can exploit the fact that three of the six unknowns have already been fixed and therefore search a value for the three Euler angles that minimize an objective function. In particular, it is not possible nor worthwhile to fully explore the solution space, i.e. all the possible combinations of these three variables, therefore, a grid of values has been selected, in order not to increase the computational time of the operations. The selected values are given by the possible configuration of a cubic geometry with deployable solar panels or with body-mounted panels, while pointing towards the sun direction. In other words, the sun position is known so one can suppose that the solar panels are placed in each of the six faces and extract the resulting Euler angles. This procedure results in six combinations for the case of deployable solar panels configuration and eight for the body-mounted one. These calculations are performed through the use of a "*for*" loop. The objective function of the LS routine provides the residuals and so the sum of their squares has been used as a quantity to minimize in a grid search procedure. For what concerns the values of the temperature for the two thermal nodes, a fixed value of 300 K has been used, while 0.5 is used for the emissivity and 0.3 for the reflectivity.

For this attitude configuration, the case of strategy 2 with the use of the LS method is reported. In an very short time span, a first guess has been identified and has been used to start the algorithm. The results for the SI and MI cases are compared both graphically and quantitatively through the MSE. Thanks to the plots of Figure **??** one can immediately notice that the quality of the estimated curves is satisfying for Sys3 for both the MI and SI applications, while, as before, only the MI gives appreciable results for Sys1 and Sys2, and the MSE presented in the following table confirm this result.

As already stated, the estimate of the reflectivity values in the case of SI application is not possible since this thermo-optical property does not affect the simulated measurements in the working wavelength band of Sys3. For this reason, the initial value of 0.3 remained constant after the calculations performed by the algorithm. On the other hand, when sensor Sys1 or Sys2 are used, it is possible to recover a better estimate for these values.

In the case of SI application, it is possible to notice a sudden decrease in the value of the estimated SNR. This is generated by the incorrect estimate of the attitude variables found by the algorithm. They have been used as initial condition to propagate the attitude dynamics of the target and the resulting motion led to a relative configuration between the sun, the observer and the target in which there is the absence of the contributions given by some of the surfaces for that particular time instant. For this reason, there is a net separation between the estimated and the measure curves in that point.

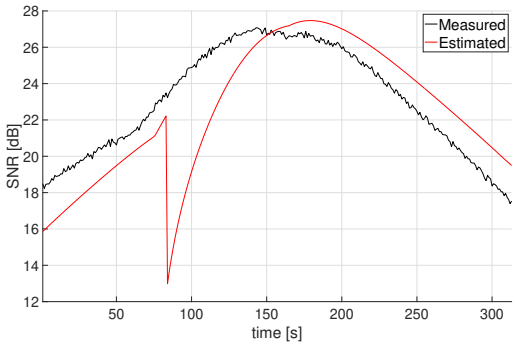

(a) SI: Sys1

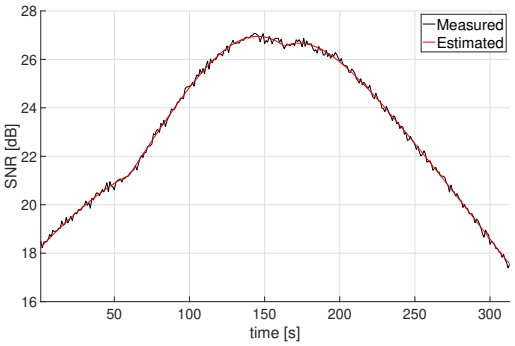

(b) MI: Sys1

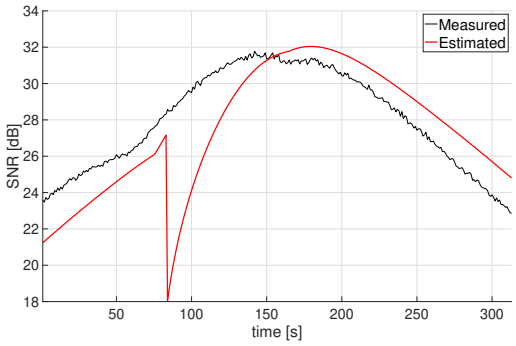

(c) SI: Sys2

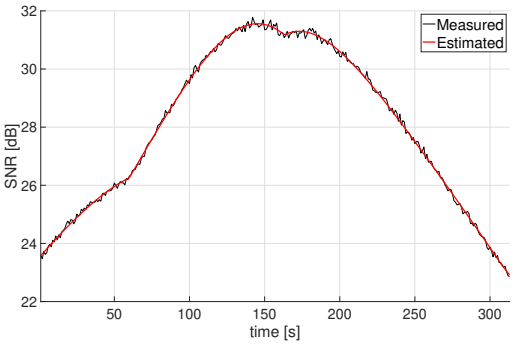

(d) MI: Sys2

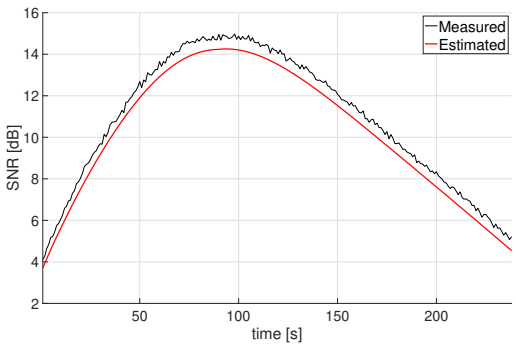

(e) SI: Sys3

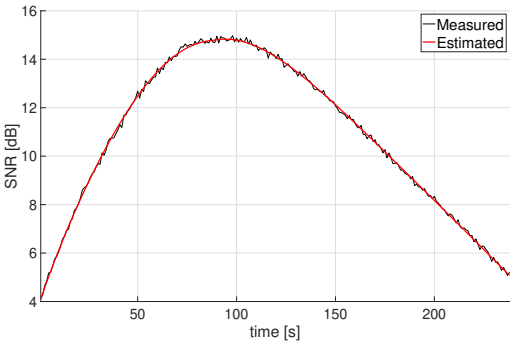

(f) MI: Sys3

Figure 6.3: Comparison SI - MI: sun-pointing

Variable	True	Estimate SI	Err% SI	Estimate MI	Err% MI
ω_x	0	-0.009	-	0.009	-
ω_y	0	0.006	-	0.009	-
ω_z	0	-0.009	-	0.002	-
ϕ	317.93	312.91	1.58	312.13	1.82
θ	107.84	104.18	3.39	107.95	0.11
ψ	42.07	48.44	15.14	42.29	0.53

Table 6.6: LS - S2 - Percentage error on attitude variables: sun-pointing

Uncertainty	SI	MI
σ_{ω_x} [deg/s]	0.148	3.398×10^{-4}
σ_{ω_y} [deg/s]	0.311	1.112×10^{-3}
σ_{ω_z} [deg/s]	0.298	6.699×10^{-4}
σ_ϕ [deg]	43.45	0.22
σ_θ [deg]	2.26	0.04
σ_ψ [deg]	37.49	0.11

Table 6.7: LS - S2 - Uncertainties on attitude variables: sun-pointing

Variable	True	Estimate SI	Err% SI	Estimate MI	Err% MI
$\bar{T}_b$	267.31	299.77	12.24	280.63	5.07
$\bar{T}_p$	337.23	321.91	4.63	321.68	4.70

Table 6.8: Percentage error on temperatures: sun-pointing

Surface	ε SI	ε MI	ρ SI	ρ MI
+X	99.59	64.43	46.15	46.15
+Y	48.69	10.31	46.14	0.77
+Z	9.28	12.90	67.86	37.45
-X	49.88	99.99	38.75	4.16
-Y	19.43	47.19	29.46	38.75
-Z	80.80	40.15	1.97	39.90
Sun	40.16	40.14	1.97	1.97
Anti-sun	17.75	19.77	46.15	6.28

Table 6.9: LS - S2 - Percentage error on emissivity and reflectivity: sun-pointing

	SI	MI
Attitude	0.054	0.069
Materials	9.842	0.010

Table 6.10: LS - S2 - MSE sun-pointing

6.3.3. Tumbling Motion Curves

An attempt to retrieve an estimate of the variables of interest in the case in which the target is experiencing a tumbling motion through the LS method has been made leading to very displeasing results, as shown in Appendix A. Consequently, it is fundamental to follow another approach. As already stated, the problem at hand could present several local minima and there is, therefore, the need to exploit the potential of the MultiStart algorithm. The lack of any information regarding possible assumptions about the first guess needed by the algorithm led to the choice of creating a set of 2000 random points that one can provide to the MultiStart routine. In this way, one can better explore the solution space to find a better result. The set of random points has been created according to lower and upper boundaries of the attitude variables. For the Euler angles, these limits are well known, while for the angular velocity components a limit of $\pm 5\, deg/s$ has been selected. This procedure clearly led to a relevant increment in the computational time.

Even in this case, the application reported is the one with the estimation of the material properties, with the use of strategy 1 and the MS algorithm. The computational effort to obtain the results for this application has considerably increased compared to the simple

estimation of the attitude variables alone. Despite this, quite accurate results have been obtained in terms of shape of the estimated curve for the SO application for observatory 1, while for observatory 2 and 3, as already highlighted for the earth-pointing case, there is not a good match between the two curves. Despite this, the match with the curve acquired by observatory 1 is very accurate. This means that, even in this case, the algorithm applied for the SO strategy found an ambiguous solution in terms of attitude variables and emissivity values. Regarding the MO application, the estimated curves provide an close match with the measured ones in some parts, but in general the quality of the estimate does not appear so accurate. These aspects could be better analysed through the values of the MSE in 6.14 and mainly through the percentage errors of the attitude variables and emissivity values. In fact, very large errors are shown for most of the variables, thus leading to the conclusion that, once again, the additional degrees of freedom present in this application gave the optimization algorithm the possibility of tuning a lot of parameters and therefore to find a better match with the measured curves, even if with an erroneous estimate of the unknowns. This possibility of retrieving a solution that produces an estimated curve very similar to the measured one is a very important aspect to underline since it could lead to an erroneous estimate of the information of interest.

Finally, it is important to stress the role of computational effort in this test case. Indeed, 2000 random points were used for the MS procedure, leading to these results which are not very accurate. This means that, perhaps, with a larger number of starting points, the algorithm could find an accurate solution at the cost of even greater computational effort. The main limitations of this methodology are therefore the time required to identify an acceptable solution and the possibility of finding a solution that produces ambiguous curves. These two aspects lead to the conclusion that this methodology may be unreliable and not very convenient.

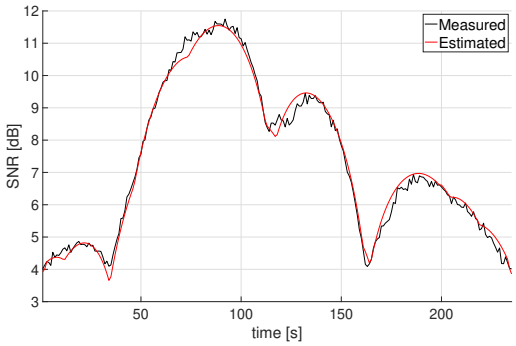

(a) SO: Observatory 1

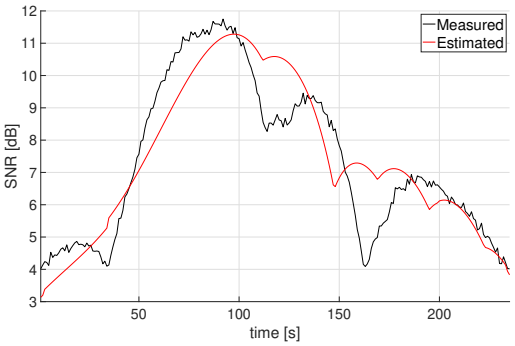

(b) MO: Observatory 1

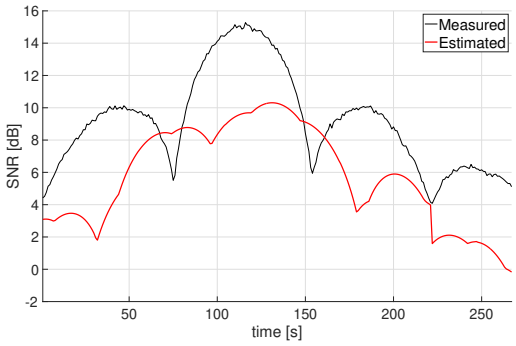

(c) SO: Observatory 2

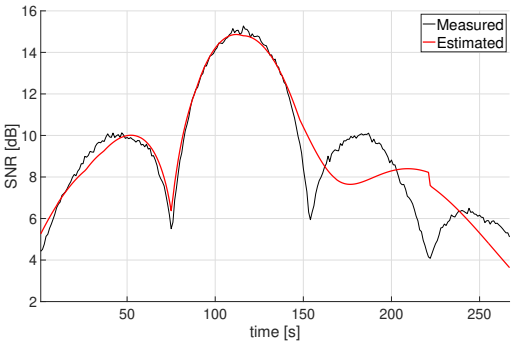

(d) MO: Observatory 2

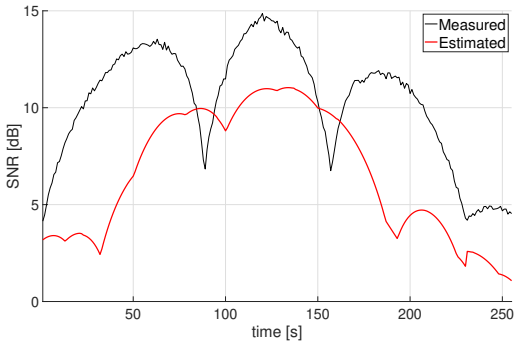

(e) SO: Observatory 3

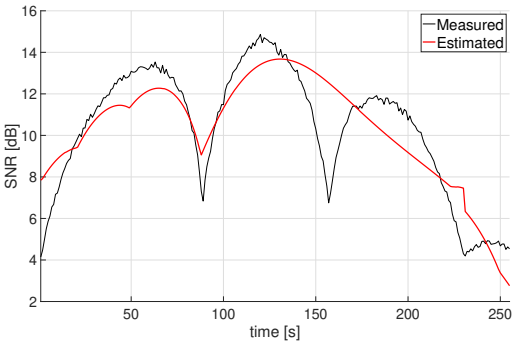

(f) MO: Observatory 3

Figure 6.4: Comparison SO - MO with MultiStart: tumbling motion

Variable	True	Estimate SO	Err% SO	Estimate MO	Err% MO
ω_x	1	-1.36	236.00	1.78	78.07
ω_y	1	-0.96	196.47	1.09	9.04
ω_z	1	1.54	54.34	2.35	135.10
ϕ	330.75	339.59	2.67	220.6	33.30
θ	82.31	57.57	30.05	87.70	6.54
ψ	302.99	332.78	9.83	130.87	56.81

Table 6.11: MS - S1 - Percentage error on attitude variables: tumbling motion

Variable	True	Estimate SO	Err% SO	Estimate MO	Err% MO
$\bar{T}_b$ 1	277.33	258.26	6.88	277.24	0.03
$\bar{T}_p$ 1	201.96	235.04	16.38	242.92	20.28
$\bar{T}_b$ 2	278.69	258.26	7.33	264.59	5.06
$\bar{T}_p$ 2	296.28	235.04	20.67	357.61	20.70
$\bar{T}_b$ 3	282.08	258.26	8.45	367.23	30.18
$\bar{T}_p$ 3	295.55	235.04	20.47	248.14	16.04

Table 6.12: Percentage error on temperatures: tumbling motion

Surface	SO	MO
+X	30.18	17.83
+Y	14.94	43.34
+Z	57.19	55.56
-X	252.94	105.22
-Y	122.50	47.79
-Z	99.89	29.49
Sun	65.98	17.70
Anti-sun	36.97	15.82

Table 6.13: MS - S1 - Percentage error on emissivity: tumbling motion

	SO	MO
Attitude	16.639	0.873
Materials	157.042	1.616

Table 6.14: MS - S1 - MSE tumbling motion

6.4. Comparison of the Results

In conclusion of this chapter, some considerations will be given regarding the results obtained with the two techniques presented above.

The methods used to estimate the variables of interest proved to be adequate under certain conditions. The knowledge of an approximate initial solution to be provided to the algorithm proved to be essential both to reduce the calculation time and to achieve greater accuracy in the results. The problems to be solved showed several local minima which required the use of appropriate techniques to overcome this obstacle. Finally, it can be noted that, from this type of measurement, the estimation of some variables is possible but the test cases highlighted also the presence of ambiguous solutions that could lead to an incorrect estimation of unknowns. For all these reasons, this type of approach to retrieve attitude variables and emissivity values of the target seems to be useful but not highly reliable.

It has to be remarked that the knowledge of a good initial guess that could be refined by the LS method, leads to an accurate solution with a reduced computational time. In fact, the MS procedure needs more time to execute the selected optimization algorithm from each start point, thus leading to hours of calculation.

The estimation of material properties turned out not to be a simple process. In fact, the percentage errors are, except for some cases, quite high. This can highlight the fact that the simultaneous estimation of a multitude of variables is a very complicated problem to solve. Trying to find the minimum of an objective function defined to obtain a good estimation of those variables could in fact be much more complicated than expected.

It is therefore possible to affirm that, to perform such an analysis, it is mandatory to analyse the problem at hand with accuracy in order to use the best methods and to be able to recognize an accurate solution.

In conclusion, from the values of the percentage errors reported in the previous tables, it is possible to notice that, in some cases, the quality of the estimated variables is higher for

strategy 1. This means that the availability of measurements acquired in different time intervals could provide more information related to the attitude state of the observed object. In fact, from the figures shown in strategy 1 it has been highlighted that a good estimate in the SO application not always led to a good matching between the estimated and the measured curves in the succesive time intervals. In the case of strategy 2, the MI application allows us to get better results with respect to the SI one, but it is not possible to extract information about the propagation in future time of the estimated variables.

From these remarks it is therefore possible to make some considerations about the two strategies. One has to consider the problem of a real application for what concerns strategy 1. In fact, there is the need of a collaboration between different sites that have to share the acquired measurements and that have all to point at the same object. On the other hand, strategy 2 involves the use of a single observation site that should have different active sensors all pointing at the same object, which could be an easier situation to manage.

7 | Conclusions

Space surveillance and tracking is a fundamental service operated today by different public and private companies in order to ensure the safety of the huge number of current and future space missions. In this context, as already stated, a fundamental part is to retrieve accurate knowledge, in the form of trajectory and attitude state, of the population of space objects present in the space environment, both LEO and GEO. Ground-based observations are still the most important way of acquiring measurements to be then used to estimate the information of interest and therefore improve the catalogue of the space objects. Among the instruments used for these purposes, there are radar, laser and optical telescopes.

The focus of this work has been the analysis of telescopes based on sensors that work in different wavelength range, for which the potential of the acquired measurements has been investigated in order to understand the role they could play in the SST scenario, especially for what concerns the infrared region. It has been shown that thermal detectors still have lower performance in therms of detectability compared to photodetectors, but they are projected to be real competitors in the near future. In addition, they can be used to detect targets also in unfavorable illumination conditions due to their sensitivity to the emitted component of radiation.

In this work, simulations and analyses have been developed. The thermal and radiometric models needed for the simulation part have been described at the beginning of this document, after a review of some theoretical notions, and they have proved to provide a reliable representation of the satellite thermal profile and the signal-to-noise ratio of the specified sensor. After this, a part devoted to the analyses of the simulated measurements has been carried out to put in evidence the information one can extract regarding the state of the observed object. For this purpose, different observing conditions have been simulated in order to give a first evaluation of the conveyed knowledge starting from the plots of the measures.

Then, different methods have been applied to obtain an estimate of some variables considered unknowns in a realistic application. The results obtained have shown good accuracy for most of the test cases but also some erroneous estimation of the variables of interest

given by the possible presence of solutions that are very similar to the real one from a point of view of the shape of the curve but very far in terms of the value of both the attitude variables and the emissivity values. This means that these kind of measurements are actually able to convey information related to the state of the target, and so that they can play a role in the SST operations. Despite this, one has to pay attention to the notion of ambiguity if the information of interest is retrieved searching for a match with an acquired measurement.

In the context of attitude and material properties estimation, this work analysed two ground-based observation strategies that showed the potential of the combination of different measurements. Data acquired from multiple observation sites, as well as data acquired from multiple instruments placed in the same observatory, have been exploited to drive the applied methods towards more precise solutions. The choice of analysing these strategy has been driven by the increasing interest in the combination of measurements coming from different instruments to exploit the different advantages they present. Some of them have work better in different scenarios and, therefore, their combined use could lead to very accurate results in terms of estimation of quantity of interest. The fusion of measurements is in fact one of the most current topics nowadays and is also the focus of the FUSMEAS group at GMV.

Finally, one has to consider the difficulties related to a practical application of such a strategy, since there is the need to link different facilities or different instruments for the same goal. For this reason, the actual potential of such a strategy has to be carefully evaluated to then justify its implementation.

7.1. Further Developments

Considering the chain that starts with the determination of the satellite temperature and ends with the calculation of the SNR through radiometric operations, the first possible development of this work consists of the following improvements. First of all, a more sophisticated geometry could be created thanks to some specific CAD software. Then, this model could be used in a well-validated thermal software capable of performing a more detailed thermal analysis of the satellite in order to recover a very precise time evolution of the temperature. After this, in the operations of the radiometric chain, a lot of constraints are present. It is possible to implement one of the numerous atmosphere models to take into account the absorption of the satellite emission by the atmospheric particles and the additional emission of those particles that will reach the ground-based instrument. Then, a comparison between a simulated curve obtained through these models and a

real one obtained by actual sensors could be fundamental to validate all the previous considerations and lead to a more accurate tool for the generation of simulated data. The validation of the simulated data would then lead to the possibility of performing very accurate simulations that could be used as a preliminary phase for a future observation survey.

For what concerns the analysis of the simulated measurements, which are necessary to estimate the state of the object, the previous results have highlighted the advantages but also the difficulties in the estimation of the variables of interest through the optimization techniques. Therefore, further developments of this work could be the use of other well-validated estimation techniques used to solve the light curve inversion problem. Their use is not straightforward since estimating either the attitude or shape of the observed target is possible using the acquired measurements under certain assumptions [10].

Bibliography

[1] B. Anderson, C. Justus, and G. Batts. Guidelines for the selection of near-earth thermal environment parameters for spacecraft design. *NASA Technical Memorandum*, 211221, 2001.

[2] L. Anikst, Z. Maassarani, J. Powe, and J. Schwartz. In-orbit performance of ultra-triple junction solar arrays. In *2013 IEEE 39th Photovoltaic Specialists Conference (PVSC)*, pages 3098–3102. IEEE, 2013.

[3] M. S. coatings. Innovative coatings for your technology. `http://www.map-space.com/12-29343-Paints.php`.

[4] R. D. Coder. *Multi-objective design of small telescopes and their application to space object characterization*. PhD thesis, Georgia Institute of Technology, 2016.

[5] A. D. Dianetti, R. Weisman, and J. L. Crassidis. Observability analysis for improved space object characterization. *Journal of Guidance, Control, and Dynamics*, 41(1): 137–148, 2018.

[6] A. Garzón and Y. A. Villanueva. Thermal analysis of satellite libertad 2: a guide to cubesat temperature prediction. *Journal of Aerospace Technology and Management*, 10, 2018.

[7] G. Gaussorgues and S. Chomet. *Infrared thermography*, volume 5. Springer Science & Business Media, 1993.

[8] D. G. Gilmore. Spacecraft thermal control handbook, fundamental technologies, vol. i the aerospace press/american institute of aeronautics and astronautics, 2002.

[9] D. W. Hafemeister. Infrared monitoring of nuclear power in space. *Science & Global Security*, 1(1-2):109–128, 1989.

[10] D. Hall, J. Africano, P. Kervin, and B. Birge. Non-imaging attitude and shape determination. In *Advanced Maui Optical and Space Surveillance Technologies Conference*, 2005.

[11] J. C. Hinks, R. Linares, and J. L. Crassidis. Attitude observability from light curve measurements. In *AIAA Guidance, Navigation, and Control (GNC) Conference*, page 5005, 2013.

[12] S. B. Howell. *Handbook of CCD astronomy*, volume 5. Cambridge University Press, 2006.

[13] C. IPAC. Infrared Windows in the Atmosphere. `http://www.icc.dur.ac.uk/~tt/Lectures/Galaxies/Images/Infrared/Windows/irwindows.html`.

[14] R. Karam. *Satellite thermal control for systems engineers*. American Institute of Aeronautics and Astronautics, 1998.

[15] L. Kauder. Spacecraft thermal control coatings references. *NASA, Goddard space flight center*, 2005.

[16] H. Käufl. Ground-based astronomy in the 10 and 20 mum atmospheric windows at eso-scientific potential at present and in the future. *The Messenger*, 73:8–12, 1993.

[17] A. Kellens. *Thermal design of the OUFTI-Next mission*. PhD thesis, MA thesis. University of Liege, 2018.

[18] A. Labibian, S. Pourtakdoust, A. Alikhani, and H. Fourati. Development of a radiation based heat model for satellite attitude determination. *Aerospace Science and Technology*, 82:479–486, 2018.

[19] R. Mason, A. Wong, T. Geballe, K. Volk, T. Hayward, M. Dillman, S. Fisher, and J. Radomski. Observing conditions and mid-ir data quality. In *Observatory Operations: Strategies, Processes, and Systems II*, volume 7016, page 70161Y. International Society for Optics and Photonics, 2008.

[20] MathWorks. Workflow for GlobalSearch and MultiStart. `https://it.mathworks.com/help/gads/outline-of-steps.html`.

[21] O. Montenbruck, E. Gill, and F. Lutze. Satellite orbits: models, methods, and applications. *Appl. Mech. Rev.*, 55(2):B27–B28, 2002.

[22] Nasa. The Navigation and Ancillary Information Facility. `https://naif.jpl.nasa.gov/naif/aboutspice.html`.

[23] L. Pirovano. *Cataloguing space debris: Methods for optical data association*. PhD thesis, University of Surrey, 2019.

[24] M. Planck. *The theory of heat radiation*. Courier Corporation, 2013.

[25] M. F. Rashman, I. A. Steele, S. D. Bates, J. H. Knapen, and D. Copley. Microbolometer arrays for ground-based infrared imaging. In *Ground-based and Airborne Instrumentation for Astronomy VIII*, volume 11447, page 1144796. International Society for Optics and Photonics, 2020.

[26] C. Ringqvist, G. Mele, H. Carlsson, M. B. S. Marta, O. Runborg, P. Enqvist, and U. Wallgren. Flir project-modeling noise in bolometer signal. 2018.

[27] A. Rogalski. Infrared detectors: an overview. *Infrared physics & technology*, 43(3-5): 187–210, 2002.

[28] A. Rogalski. History of infrared detectors. *Opto-Electronics Review*, 20(3):279–308, 2012.

[29] SAIC. Space-track.org. `https://www.space-track.org/`. Accessed: 2021-05-23.

[30] SatCen. Space Situational Awareness (SSA). `https://www.satcen.europa.eu/page/ssa`.

[31] J. R. Shell. Optimizing orbital debris monitoring with optical telescopes. Technical report, AIR FORCE SPACE INNOVATION AND DEVELOPMENT CENTER SCHRIEVER AFB CO, 2010.

[32] Teledyne. How a Charge Coupled Device (CCD) Image Sensor Works. `https://www.teledyneimaging.com/media/1300/2020-01-22_e2v_how-a-charge-coupled-device-works_web.pdf`.

[33] A. Thomson et al. Astronomy on the personal computer. o. montenbruck and t. pfleger (english translation by s. dunlop) springer-verlag, berlin, dm 79.00, isbn 3-540-52754-0, 255 pages. *Vistas in Astronomy*, 34:iii–iv, 1991.

[34] D. A. Vallado. *Fundamentals of astrodynamics and applications*, volume 12. Springer Science & Business Media, 2001.

[35] M. E. Van Valkenburg. *Reference data for engineers: radio, electronics, computers and communications*. Elsevier, 2001.

[36] J. Vilaboa Perez et al. Master thesis: Multi-band ir sensor for earth observation. 2019.

[37] K. Vugrin, L. Swiler, R. Roberts, N. Stucky-Mack, and S. Sullivan. Confidence region estimation techniques for nonlinear regression in groundwater flow: Three case studies. *Water Resources Research*, 43(3), 2007.

[38] C. J. Wetterer and M. Jah. Attitude determination from light curves. *Journal of Guidance, Control, and Dynamics*, 32(5):1648–1651, 2009.

[39] C. J. Wetterer, B. Hunt, K. Hamada, J. L. Crassidis, and P. Kervin. Shape, surface parameter, and attitude profile estimation using a multiple hypothesis unscented kalman filter. *Adv. Astronaut. Sci.*, 152:1475–1484, 2014.

[40] Wikipedia. Signal-to-noise ratio. `https://en.wikipedia.org/wiki/Signal-to-noise_ratio`, .

[41] Wikipedia. Space Situational Awareness Programme. `https://en.wikipedia.org/wiki/Space_Situational_Awareness_Programme`, .

[42] Ö. Yılmaz, N. Aouf, E. Checa, L. Majewski, and M. Sanchez-Gestido. Thermal analysis of space debris for infrared-based active debris removal. *Proceedings of the Institution of Mechanical Engineers, Part G: Journal of Aerospace Engineering*, 233 (3):811–822, 2019.

A | Appendix

In this appendix of the document, the results of all the test cases are reported. Two strategies, two methods and three attitude configurations have been considered in this work, thus resulting in 12 test cases for the simple attitude variables estimation case and other 12 for the estimation of both the attitude variables and materials properties.

A.1. Matching through Non-linear Least Squares

A.1.1. Strategy 1: Multiple Observatories

Earth-pointing Curves: attitude estimation

Variable	True	Estimate SO	Err% SO	Estimate MO	Err% MO
ω_x	0	$\sim$0	-	$\sim$0	-
ω_y	-0.0647	-0.0143	77.92	-0.0561	12.96
ω_z	0	$\sim$0	-	$\sim$0	-
ϕ	133.50	167.88	25.31	149.54	11.61
θ	136.94	44.12	67.78	85.94	37.20
ψ	155.27	126.05	18.87	168.45	8.36

Table A.1: LS - S1 - Percentage error on attitude variables: earth-pointing

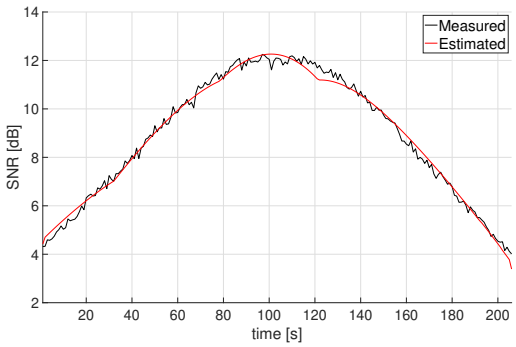

(a) SO: Observatory 1

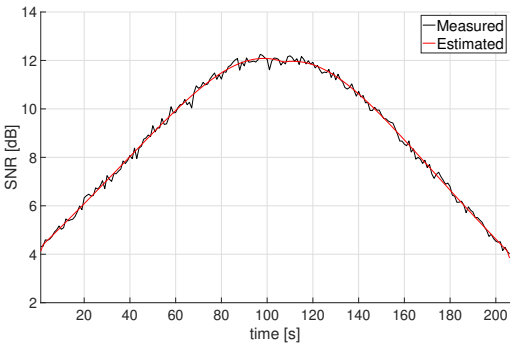

(b) MO: Observatory 1

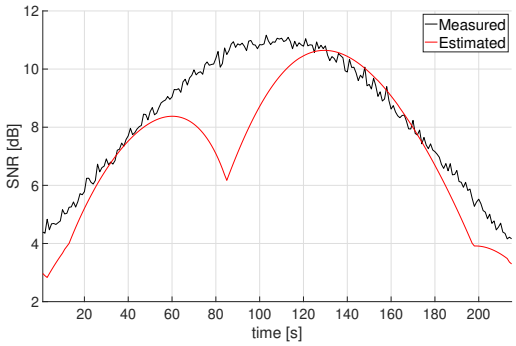

(c) SO: Observatory 2

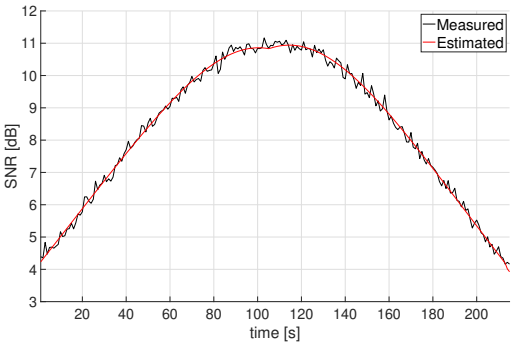

(d) MO: Observatory 2

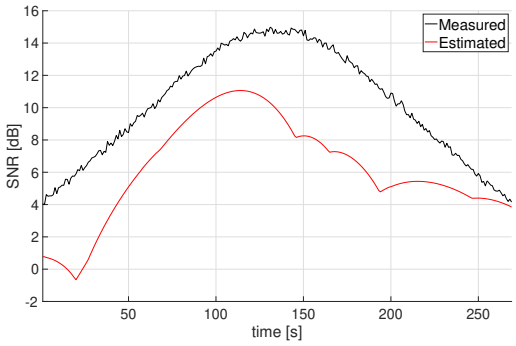

(e) SO: Observatory 3

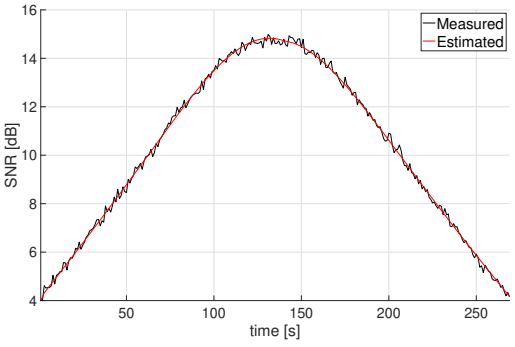

(f) MO: Observatory 3

Figure A.1: Comparison SO - MO: earth-pointing

Uncertainty	SO	MO
σ_{ω_x} [deg/s]	1.191×10^{-1}	7.280×10^{-4}
σ_{ω_y} [deg/s]	2.490×10^{-2}	5.510×10^{-5}
σ_{ω_z} [deg/s]	3.360×10^{-2}	1.060×10^{-4}
σ_ϕ [deg]	36.30	0.81
σ_θ [deg]	6.95	0.12
σ_ψ [deg]	11.87	0.33

Table A.2: LS - S1 - Uncertainties on attitude variables: earth-pointing

Earth-pointing Curves: attitude and material estimation

Variable	True	Estimate SO	Err% SO	Estimate MO	Err% MO
ω_x	0	$\sim$0	-	$\sim$0	-
ω_y	-0.0647	-0.166	158.45	-0.0573	10.69
ω_z	0	$\sim$0	-	$\sim$0	-
ϕ	133.50	125.48	6.03	141.52	5.69
θ	136.94	99.69	27.05	130.06	4.89
ψ	155.27	171.31	10.47	178.76	15.06

Table A.3: LS - S1 - Percentage error on attitude variables: earth-pointing (materials)

Uncertainty	SO	MO
σ_{ω_x} [deg/s]	9.763×10^{-2}	4.215×10^{-3}
σ_{ω_y} [deg/s]	8.170×10^{-2}	1.150×10^{-3}
σ_{ω_z} [deg/s]	3.537×10^{-1}	6.140×10^{-4}
σ_ϕ [deg]	26.91	4.43
σ_θ [deg]	23.40	1.41
σ_ψ [deg]	30.30	1.91

Table A.4: LS - S1 - Uncertainties on attitude variables: earth-pointing (materials)

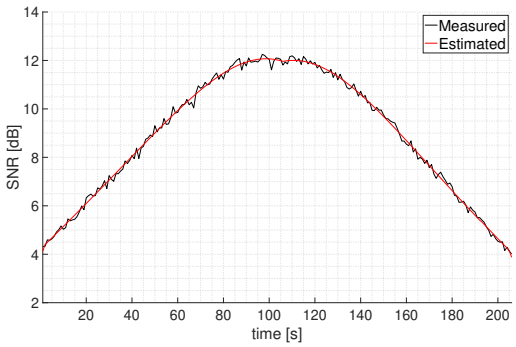

(a) SO: Observatory 1

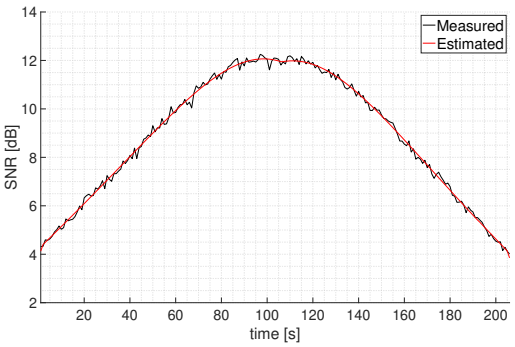

(b) MO: Observatory 1

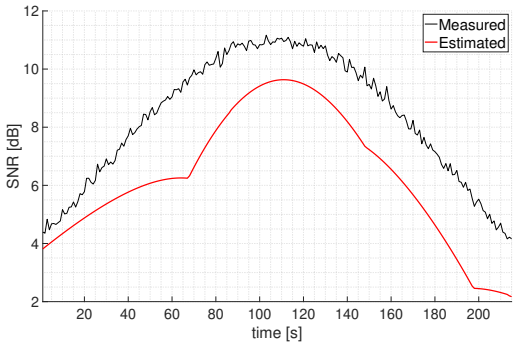

(c) SO: Observatory 2

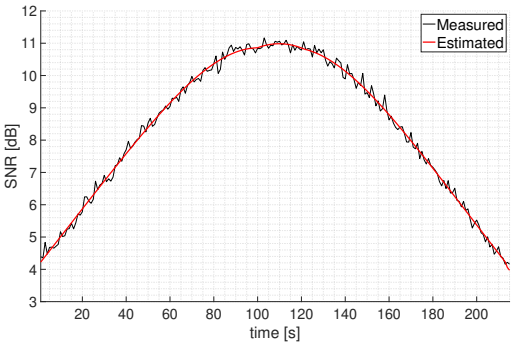

(d) MO: Observatory 2

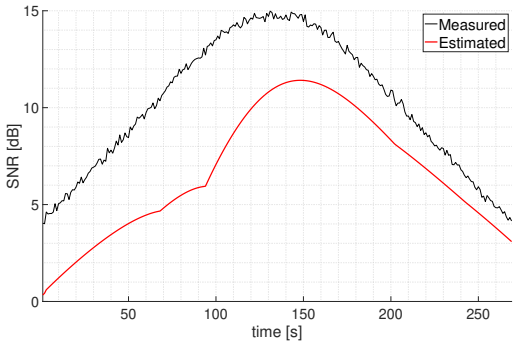

(e) SO: Observatory 3

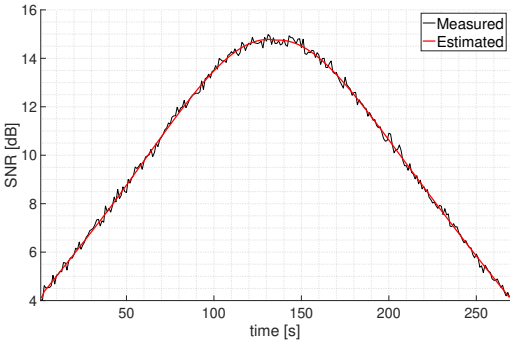

(f) MO: Observatory 3

Figure A.2: Comparison SO - MO: earth-pointing (materials)

Surface	SO	MO
+X	41.91	0.23
+Y	89.39	0.43
+Z	39.62	1.70
-X	8.68	0.12
-Y	99.99	0.44
-Z	40.16	40.16
Sun	40.16	40.16
Anti-sun	17.83	1.94

Table A.5: LS - S1 - Percentage error on emissivity: earth-pointing

	SO	MO
Attitude	7.518	2.452×10^{-3}
Materials	8.043	2.810×10^{-3}

Table A.6: LS - S1 - MSE earth-pointing

Sun-pointing Curves: attitude estimation

Variable	True	Estimate SO	Err% SO	Estimate MO	Err% MO
ω_x	0	$\sim$0	-	$\sim$0	-
ω_y	0	$\sim$0	-	$\sim$0	-
ω_z	0	$\sim$0	-	$\sim$0	-
ϕ	317.93	26.15	91.77	327.21	2.92
θ	107.84	106.89	0.88	105.48	2.19
ψ	42.06	32.23	23.38	25.84	38.58

Table A.7: LS - S1 - Percentage error on attitude variables: sun-pointing

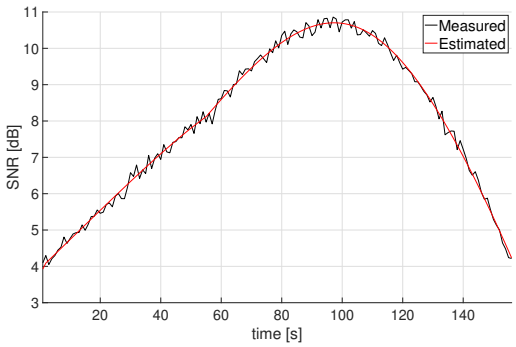

(a) SO: Observatory 1

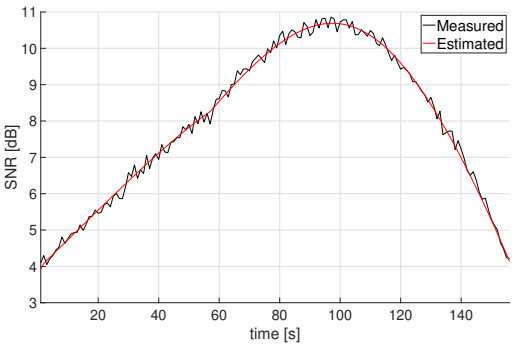

(b) MO: Observatory 1

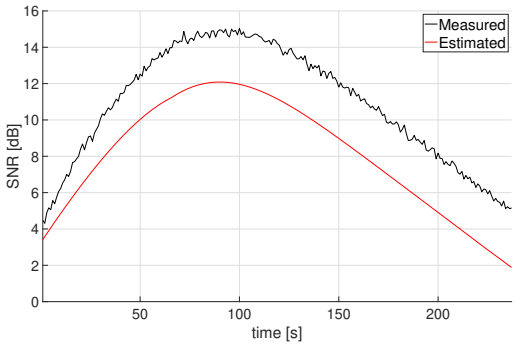

(c) SO: Observatory 2

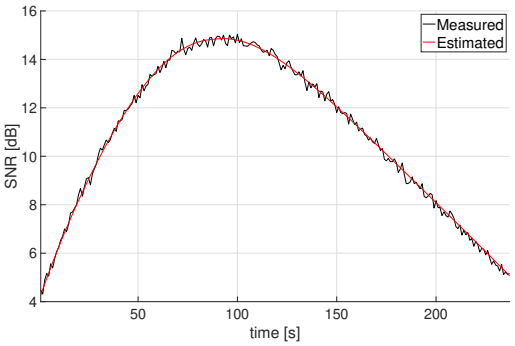

(d) MO: Observatory 2

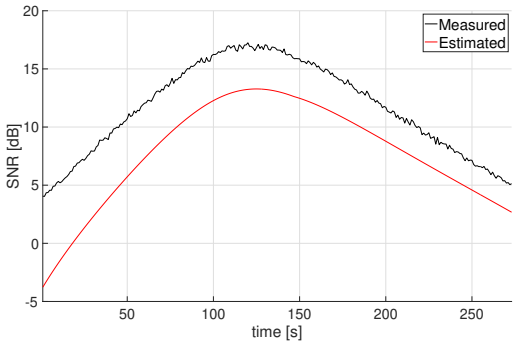

(e) SO: Observatory 3

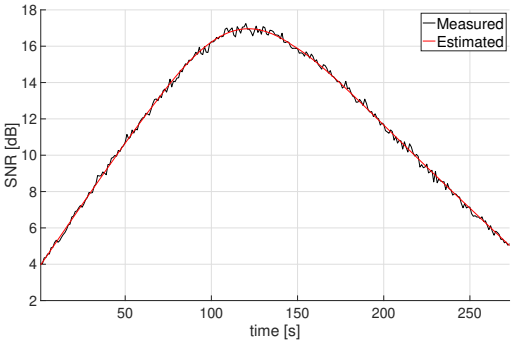

(f) MO: Observatory 3

Figure A.3: Comparison SO - MO: sun-pointing

Uncertainty	SO	MO
σ_{ω_x} [deg/s]	4.739×10^{-2}	6.840×10^{-5}
σ_{ω_y} [deg/s]	1.219×10^{-2}	3.840×10^{-5}
σ_{ω_z} [deg/s]	6.526×10^{-2}	2.899×10^{-3}
σ_ϕ [deg]	14.15	0.06
σ_θ [deg]	3.22	0.08
σ_ψ [deg]	20.64	0.33

Table A.8: LS - S1 - Uncertainties on attitude variables: sun-pointing

Matching without grid search

To validate the choice of performing a preliminary grid search to identify an acceptable initial solution, a common first guess with the three Euler angles set to zero degrees has been tested. The results obtained are not at all accurate, as it can be noted from Figure A.4. This means that, if the initial solution given to the algorithm is not sufficiently close to the real one, the LS method cannot provide a valid estimation of the quantities of interest for this problem. The need for a strategy to identify a valid initial solution for the LS algorithm, like the grid search, has driven the interest of this work towards other methods that could better manage this problem.

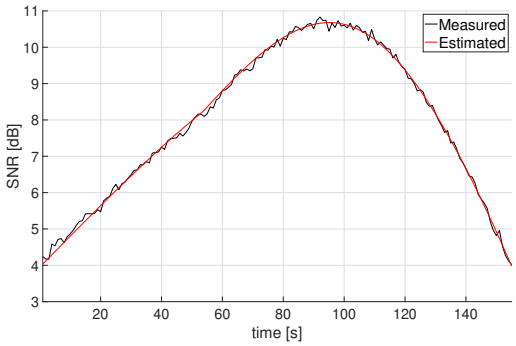

(a) SO: Observatory 1

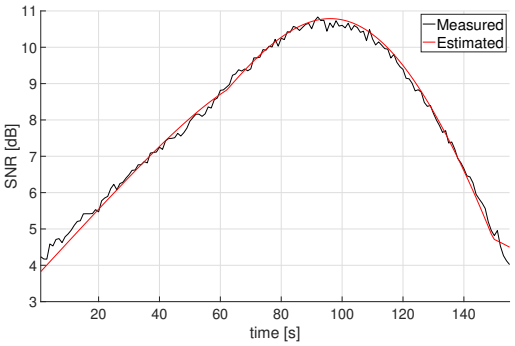

(b) MO: Observatory 1

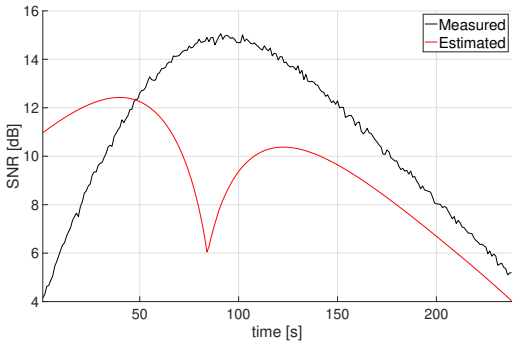

(c) SO: Observatory 2

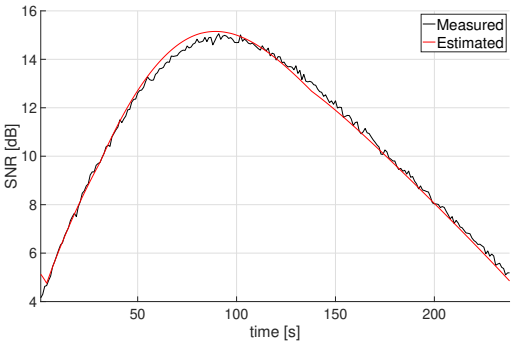

(d) MO: Observatory 2

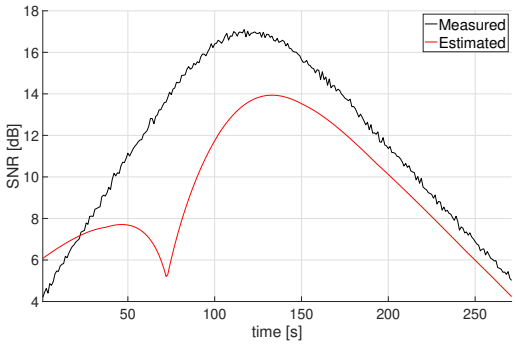

(e) SO: Observatory 3

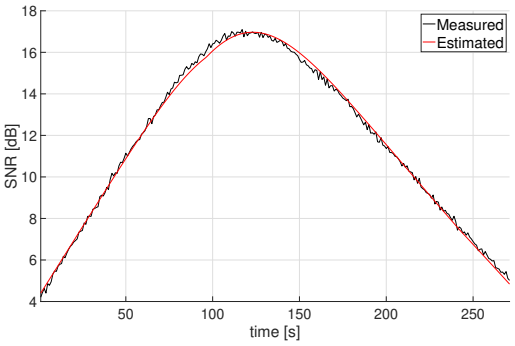

(f) MO: Observatory 3

Figure A.4: Comparison SO - MO: sun-pointing (without grid search)

Variable	True	Estimate SO	Err% SO	Estimate MO	Err% MO
ω_x	0	∼0	-	∼0	-
ω_y	0	∼0	-	∼0	-
ω_z	0	∼0	-	∼0	-
ϕ	317.93	287.22	9.66	191.94	39.63
θ	107.84	68.60	36.39	40.04	62.87
ψ	42.06	59.54	41.53	110.60	162.89

Table A.9: LS - S1 - Percentage error on attitude variables: sun-pointing (without grid search)

Sun-pointing Curves: attitude and material estimation

Variable	True	Estimate SO	Err% SO	Estimate MO	Err% MO
ω_x	0	∼0	-	∼0	-
ω_y	0	∼0	-	∼0	-
ω_z	0	∼0	-	∼0	-
ϕ	317.93	301.7	5.10	295.39	7.09
θ	107.84	70.03	35.06	105.25	2.40
ψ	42.06	143.64	241.51	20.87	50.40

Table A.10: LS - S1 - Percentage error on attitude variables: sun-pointing (materials)

Uncertainty	SO	MO
σ_{ω_x} [deg/s]	2.898×10^{-1}	3.134×10^{-3}
σ_{ω_y} [deg/s]	3.862×10^{-1}	3.117×10^{-3}
σ_{ω_z} [deg/s]	1.232×10^{-1}	6.297×10^{-3}
σ_ϕ [deg]	42.55	0.32
σ_θ [deg]	30.18	0.31
σ_ψ [deg]	50.84	0.72

Table A.11: LS - S1 - Uncertainties on attitude variables: sun-pointing (materials)

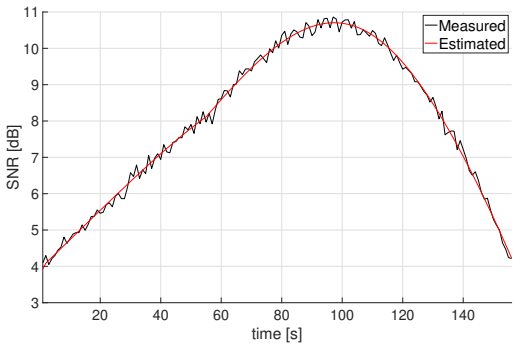

(a) SO: Observatory 1

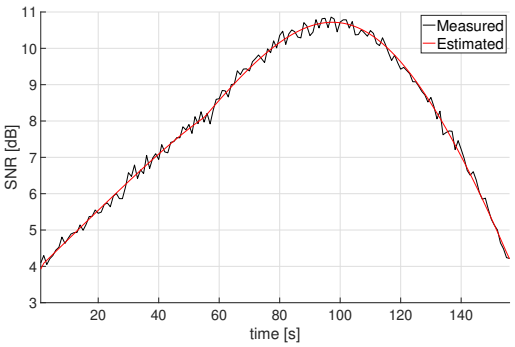

(b) MO: Observatory 1

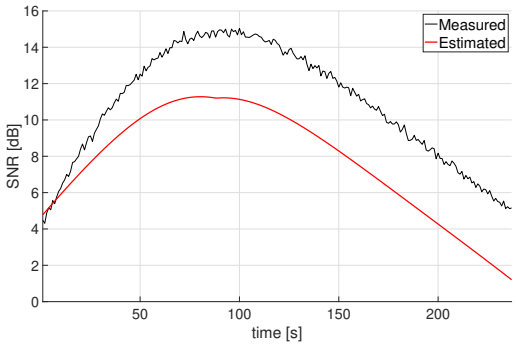

(c) SO: Observatory 2

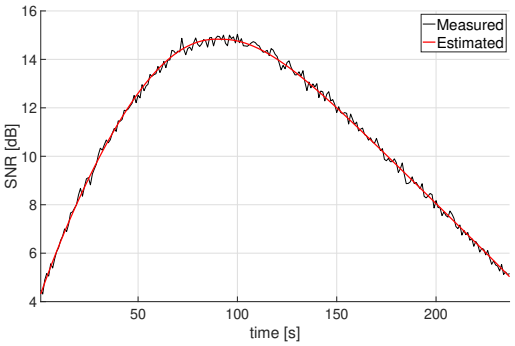

(d) MO: Observatory 2

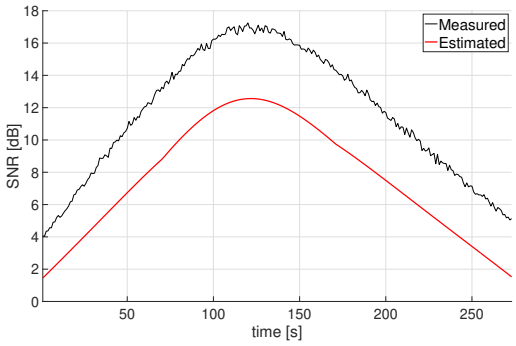

(e) SO: Observatory 3

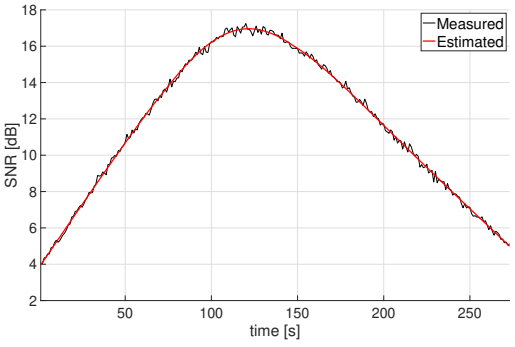

(f) MO: Observatory 3

Figure A.5: Comparison SO - MO: sun-pointing (materials)

Surface	SO	MO
+X	74.88	1.31
+Y	77.68	1.08
+Z	40.35	20.77
-X	8.61	0.25
-Y	99.99	1.20
-Z	3.97	19.67
Sun	0.31	0.99
Anti-sun	16.83	1.17

Table A.12: LS - S1 - Percentage error on emissivity: sun-pointing

	SO	MO
Attitude	34.08	4.996×10^{-2}
Materials	71.80	3.425×10^{-2}

Table A.13: LS - S1 - MSE sun-pointing

Tumbling Motion Curves: attitude estimation

For the sake of completeness, the LS method has been applied also to the tumbling motion case. The initial solution for the algorithm cannot be chosen following a precise strategy, and, therefore, a grid search procedure is exploited also here, trying not to significantly increase the computational time.

Once an initial solution is available, it can be given to the algorithm to perform the calculations. As one can clearly deduce from the plots of Figure A.6, the results are not satisfying. The algorithm is not able to retrieve a good estimate of the satellite attitude because of its high dependence on the initial solution. The procedure has been run several times, trying to change the value of the initial solution, but the conclusion has always been unsuccessful. During the operations, it has been noted that the results coming from the application of the LS algorithm did not move far from the initial solution provided by the user. This could mean that the problem at hand presents several local minima where the algorithm stops the computations. For this reason, a different strategy has to be applied, in order to better explore the solution space and trying not to stop at a local minimum. Given the displeasing results, the LS method has not been applied for the estimation of the emissivity values.

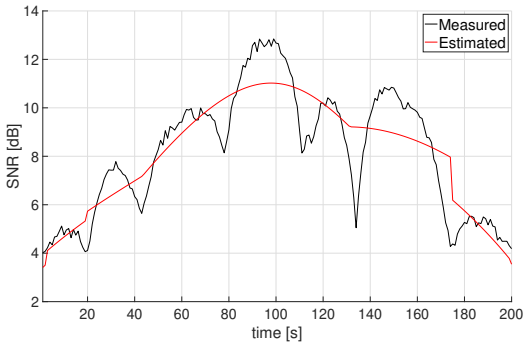

(a) SO: Observatory 1

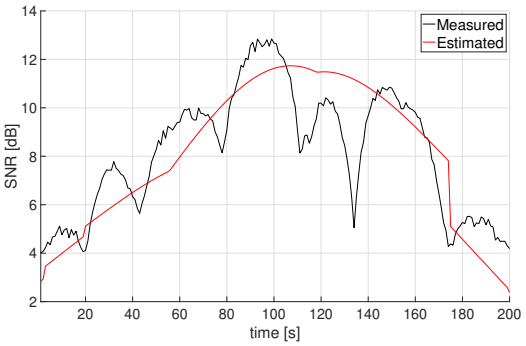

(b) MO: Observatory 1

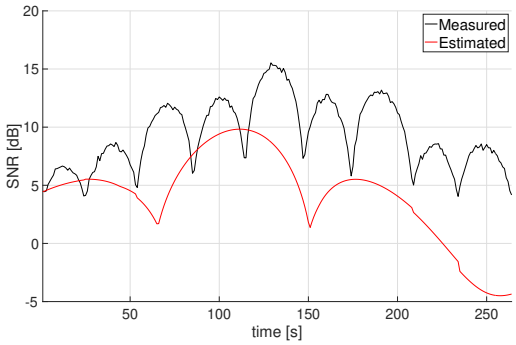

(c) SO: Observatory 2

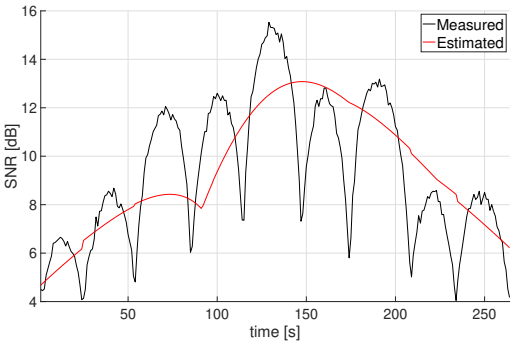

(d) MO: Observatory 2

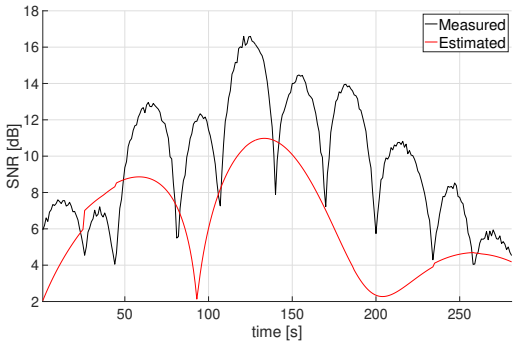

(e) SO: Observatory 3

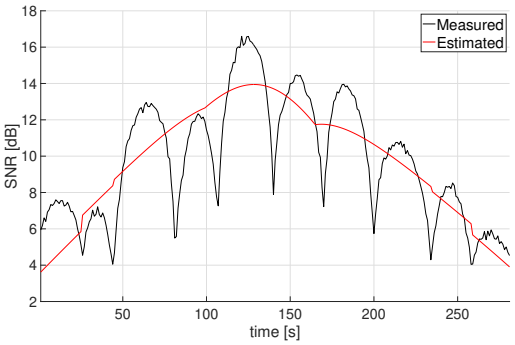

(f) MO: Observatory 3

Figure A.6: Comparison SO - MO: tumbling

	SO	MO
Attitude	14.663	3.662

Table A.14: LS - S1 - MSE tumbling motion

A.1.2. Strategy 2: Multiple Instruments

Earth-pointing Curves: attitude estimation

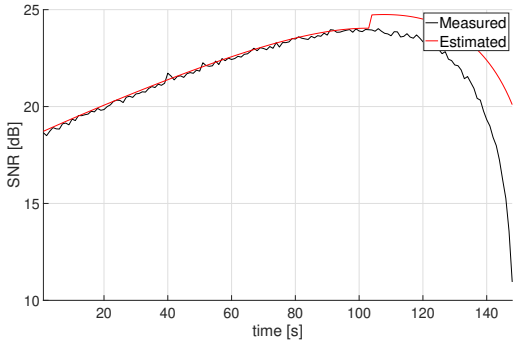

(a) SI: Sys1

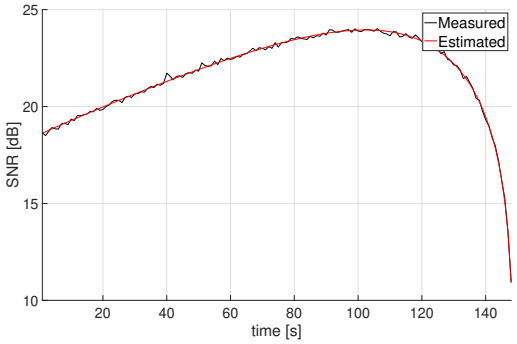

(b) MI: Sys1

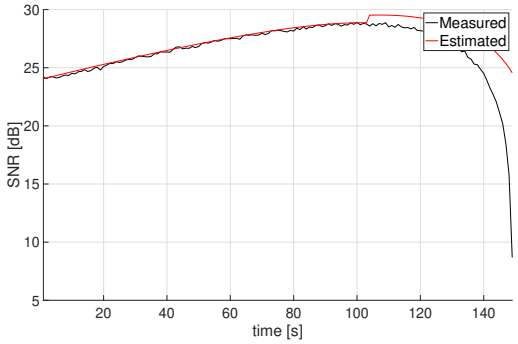

(c) SI: Sys2

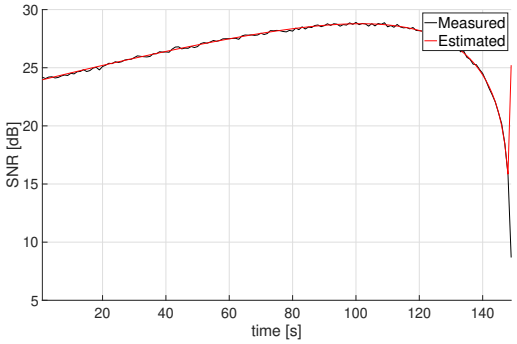

(d) MI: Sys2

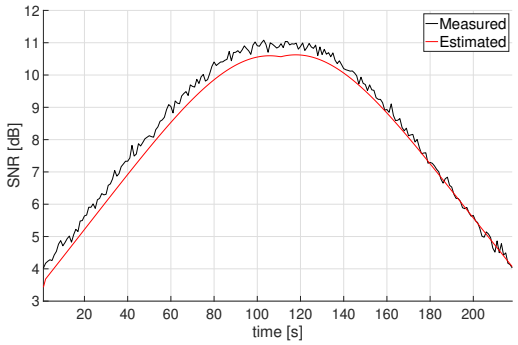

(e) SI: Sys3

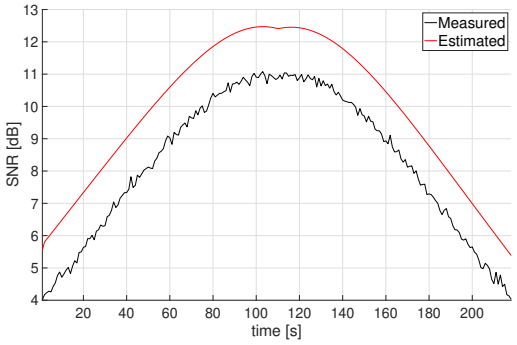

(f) MI: Sys3

Figure A.7: Comparison SI - MI: earth-pointing

Variable	True	Estimate SI	Err% SI	Estimate MI	Err% MI
ω_x	0	0.148	-	0.0647	-
ω_y	-0.0647	-0.0719	11.29	-0.0706	9.24
ω_z	0	-0.025	-	-0.0017	-
ϕ	216.25	224.98	4.04	216.93	0.32
θ	128.72	124.39	3.37	127.38	1.05
ψ	217.33	116.86	0.21	216.19	0.52

Table A.15: LS - S2 - Percentage error on attitude variables: earth-pointing

Uncertainty	SI	MI
σ_{ω_x} [deg/s]	3.596	0.239
σ_{ω_y} [deg/s]	1.085	0.034
σ_{ω_z} [deg/s]	0.629	0.082
σ_ϕ [deg]	5.49	9.42
σ_θ [deg]	31.28	1.96
σ_ψ [deg]	22.81	1.71

Table A.16: LS - S2 - Uncertainties on attitude variables: earth-pointing

Earth-pointing Curves: attitude and materials estimation

Variable	True	Estimate SI	Err% SI	Estimate MI	Err% MI
ω_x	0	0.318	-	0.318	-
ω_y	-0.0647	-0.115	78.30	-0.024	62.90
ω_z	0	-0.018	-	0.087	-
ϕ	216.25	205.52	4.96	219.03	1.29
θ	128.72	133.13	3.42	123.74	3.87
ψ	217.33	215.48	0.85	224.16	3.14

Table A.17: LS - S2 - Percentage error on attitude variables: earth-pointing (materials)

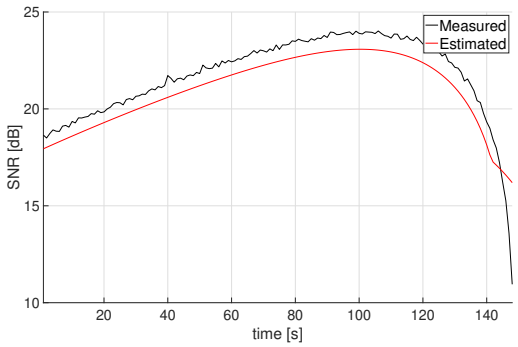

(a) SI: Sys1

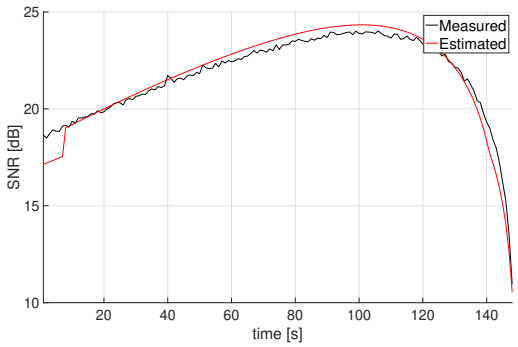

(b) MI: Sys1

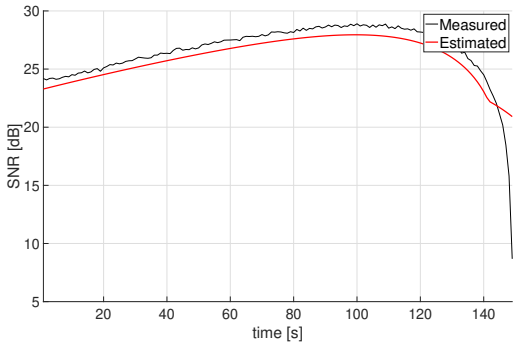

(c) SI: Sys2

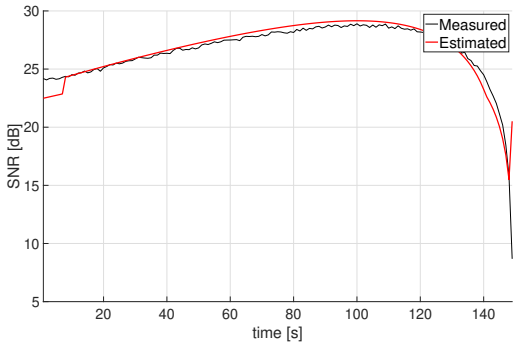

(d) MI: Sys2

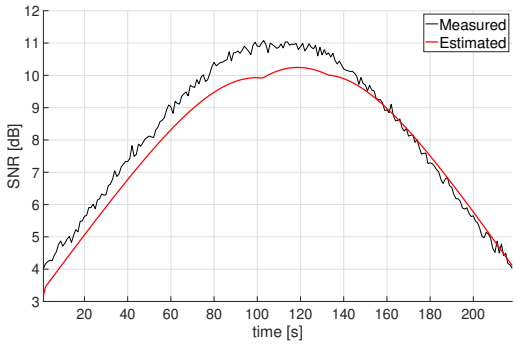

(e) SI: Sys3

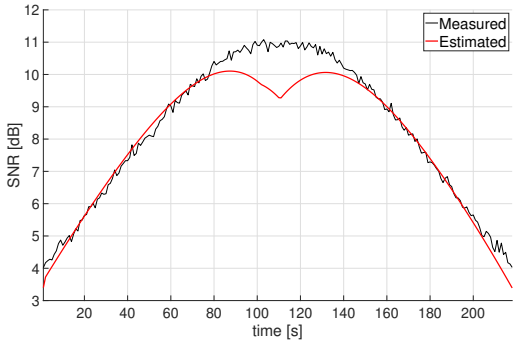

(f) MI: Sys3

Figure A.8: Comparison SI - MI: earth-pointing (materials)

Uncertainty	SI	MI
σ_{ω_x} [deg/s]	0.096	0.009
σ_{ω_y} [deg/s]	0.021	0.002
σ_{ω_z} [deg/s]	0.014	0.005
σ_ϕ [deg]	12.35	1.54
σ_θ [deg]	4.12	0.85
σ_ψ [deg]	1.43	0.18

Table A.18: LS - S2 - Uncertainties on attitude variables: earth-pointing (materials)

Surface	ε SI	ε MI	ρ SI	ρ MI
+X	86.83	85.96	46.15	33.72
+Y	27.55	16.42	46.14	46.14
+Z	73.47	36.96	67.86	7.23
-X	92.47	69.94	38.75	38.75
-Y	81.58	2.91	29.46	47.53
-Z	40.16	40.16	1.97	1.97
Sun	40.16	40.16	1.97	1.97
Anti-sun	17.75	14.12	46.15	35.14

Table A.19: LS - S2 - Percentage error on emissivity and reflectivity: earth-pointing

	SI	MI
Attitude	1.845	1.041
Materials	0.940	0.265

Table A.20: LS - S2 - MSE earth-pointing

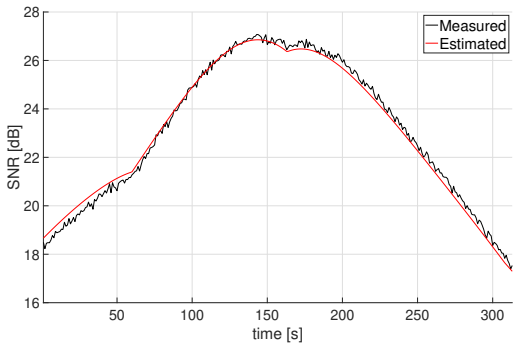

(a) SI: Sys1

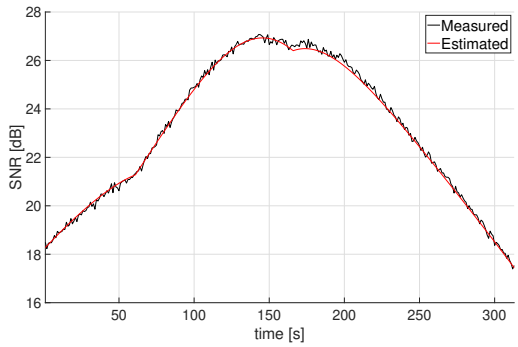

(b) MI: Sys1

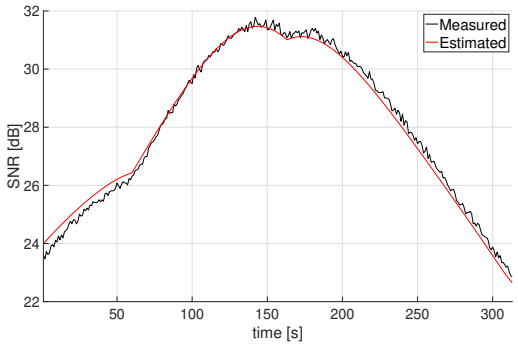

(c) SI: Sys2

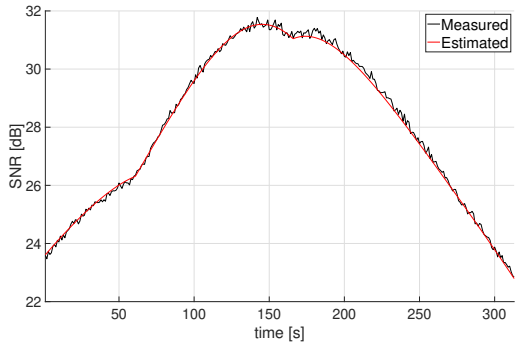

(d) MI: Sys2

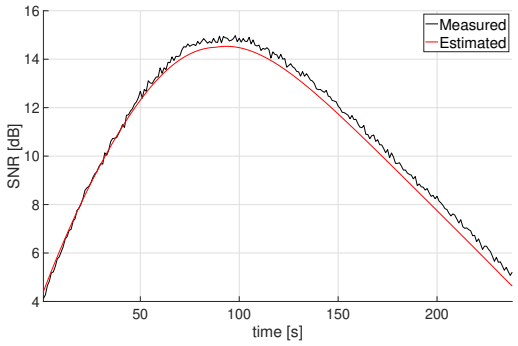

(e) SI: Sys3

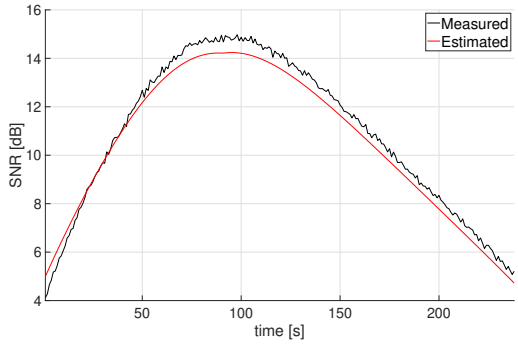

(f) MI: Sys3

Figure A.9: Comparison SI - MI: sun-pointing

Sun-pointing Curves: attitude estimation

Variable	True	Estimate SI	Err% SI	Estimate MI	Err% MI
ω_x	0	-0.009	-	-0.008	-
ω_y	0	~ 0	-	~ 0	-
ω_z	0	-0.001	-	-0.007	-
ϕ	317.93	316.55	0.43	317.96	0.01
θ	107.83	108.25	0.39	107.82	0.02
ψ	42.07	43.61	3.66	42.24	0.41

Table A.21: LS - S2 - Percentage error on attitude variables: sun-pointing

Uncertainty	SI	MI
σ_{ω_x} [deg/s]	3.699×10^{-2}	8.767×10^{-4}
σ_{ω_y} [deg/s]	7.553×10^{-2}	4.323×10^{-3}
σ_{ω_z} [deg/s]	4.829×10^{-1}	2.301×10^{-3}
σ_ϕ [deg]	36.25	0.82
σ_θ [deg]	1.32	0.18
σ_ψ [deg]	59.28	0.38

Table A.22: LS - S2 - Uncertainties on attitude variables: sun-pointing

Sun-pointing Curves: attitude and materials estimation

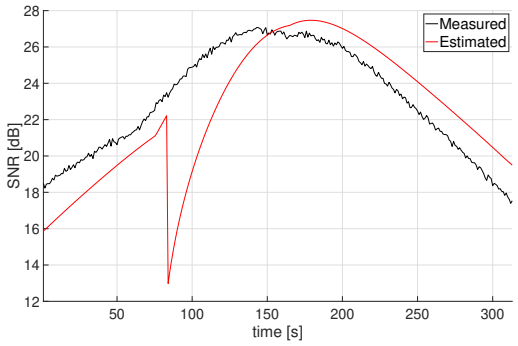

(a) SI: Sys1

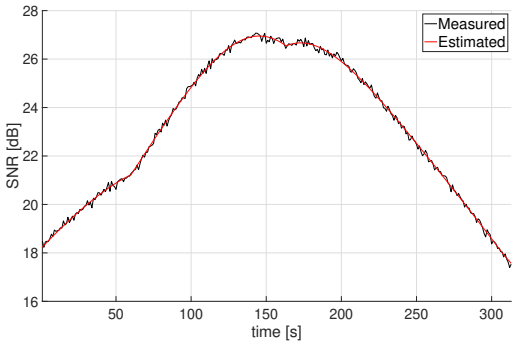

(b) MI: Sys1

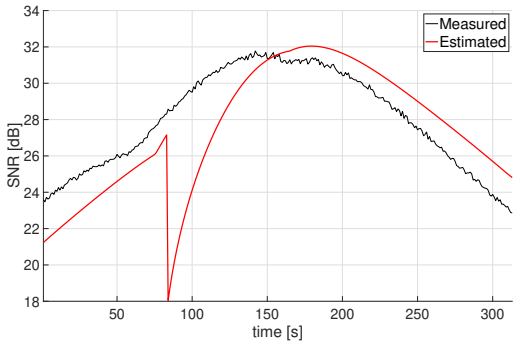

(c) SI: Sys2

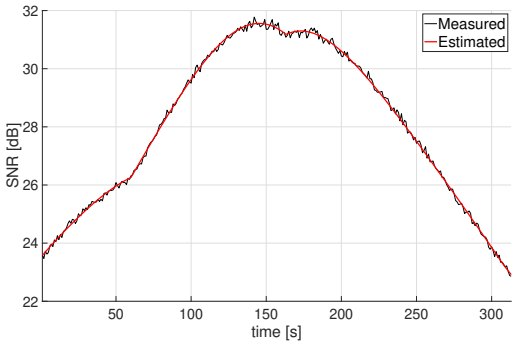

(d) MI: Sys2

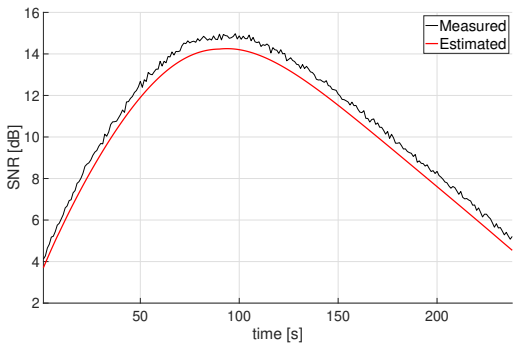

(e) SI: Sys3

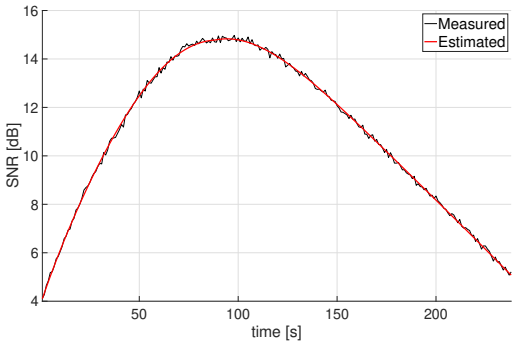

(f) MI: Sys3

Figure A.10: Comparison SI - MI: sun-pointing (materials)

Variable	True	Estimate SI	Err% SI	Estimate MI	Err% MI
ω_x	0	-0.009	-	0.009	-
ω_y	0	0.006	-	0.009	-
ω_z	0	-0.009	-	0.002	-
ϕ	317.93	312.91	1.58	312.13	1.82
θ	107.83	104.18	3.39	107.95	0.11
ψ	42.07	48.44	15.14	42.29	0.53

Table A.23: LS - S2 - Percentage error on attitude variables: sun-pointing (materials)

Uncertainty	SI	MI
σ_{ω_x} [deg/s]	0.148	3.398×10^{-4}
σ_{ω_y} [deg/s]	0.311	1.112×10^{-3}
σ_{ω_z} [deg/s]	0.298	6.699×10^{-4}
σ_ϕ [deg]	43.45	0.22
σ_θ [deg]	2.26	0.04
σ_ψ [deg]	37.49	0.11

Table A.24: LS - S2 - Uncertainties on attitude variables: sun-pointing (materials)

Surface	ε SI	ε MI	ρ SI	ρ MI
+X	99.59	64.43	46.15	46.15
+Y	48.69	10.31	46.14	0.77
+Z	9.28	12.90	67.86	37.45
-X	49.88	99.99	38.75	4.16
-Y	19.43	47.19	29.46	38.75
-Z	80.80	40.15	1.97	39.90
Sun	40.16	40.14	1.97	1.97
Anti-sun	17.75	19.77	46.15	6.28

Table A.25: LS - S2 - Percentage error on emissivity and reflectivity: sun-pointing

	SI	MI
Attitude	0.054	0.069
Materials	9.842	0.010

Table A.26: LS - S2 - MSE sun-pointing

A.2. Matching through MultiStart Algorithm

A.2.1. Strategy 1: Multiple Observations

Earth-pointing Curves: attitude estimation

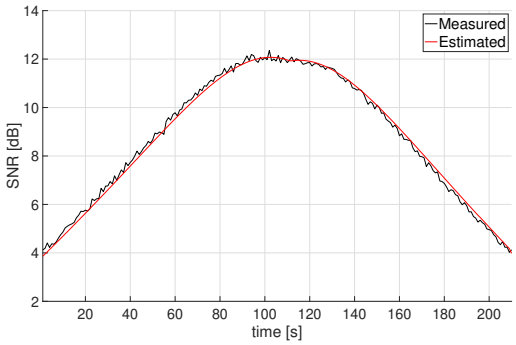

(a) SO: Observatory 1

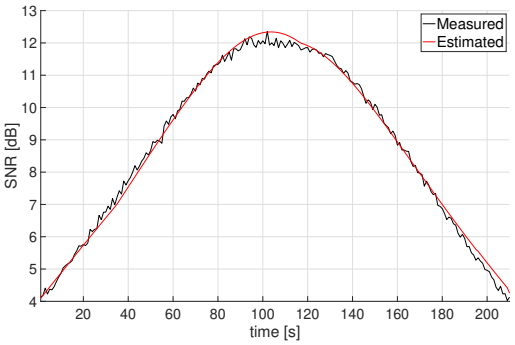

(b) MO: Observatory 1

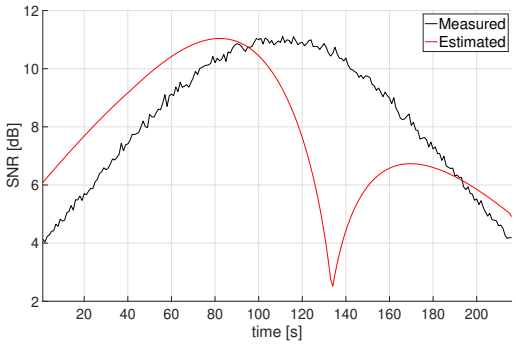

(c) SO: Observatory 2

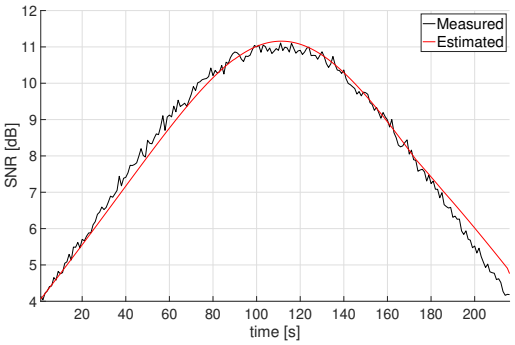

(d) MO: Observatory 2

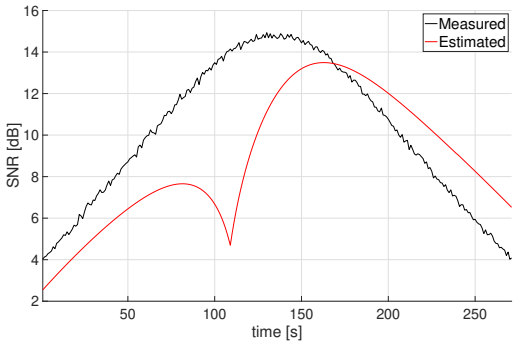

(e) SO: Observatory 3

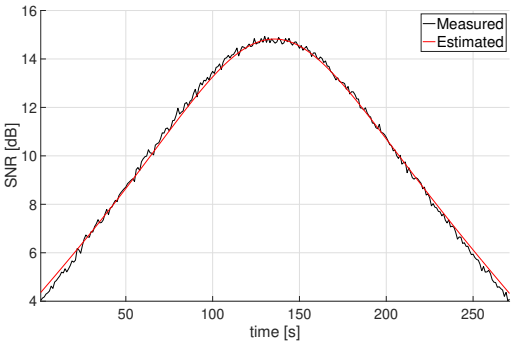

(f) MO: Observatory 3

Figure A.11: Comparison SO - MO with MultiStart: earth-pointing

Variable	True	Estimate SO	Err% SO	Estimate MO	Err% MO
ω_x	0	-0.2693	-	0.2947	-
ω_y	-0.0647	0.0005	100.80	0.0109	116.87
ω_z	0	0.0108	-	0.0057	-
ϕ	133.50	147.68	10.47	90.01	32.67
θ	136.94	23.21	83.06	110.21	19.56
ψ	155.27	178.85	15.03	341.58	119.68

Table A.27: MS - S1 - Percentage error on attitude variables: earth-pointing

Earth-pointing Curves: attitude and material estimation

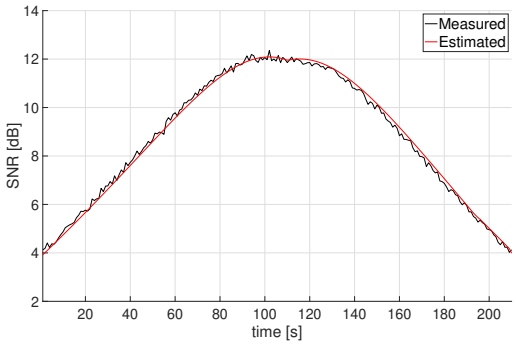

(a) SO: Observatory 1

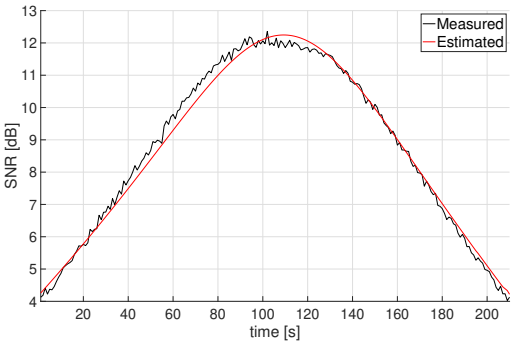

(b) MO: Observatory 1

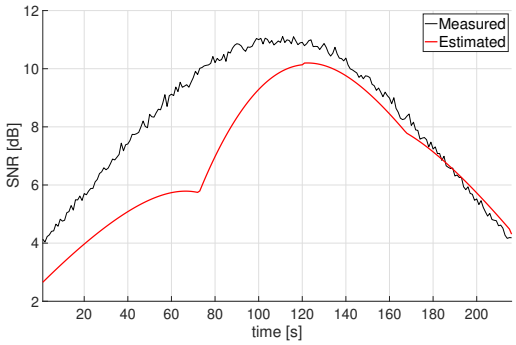

(c) SO: Observatory 2

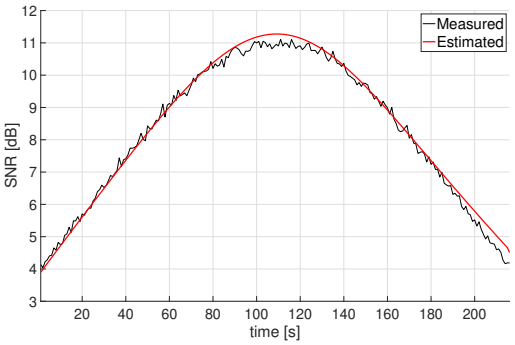

(d) MO: Observatory 2

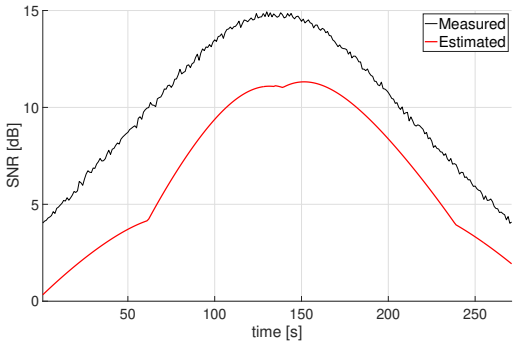

(e) SO: Observatory 3

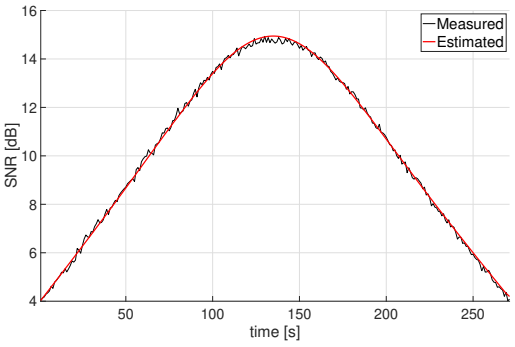

(f) MO: Observatory 3

Figure A.12: Comparison SO - MO with MultiStart: earth-pointing (materials)

Variable	True	Estimate SO	Err% SO	Estimate MO	Err% MO
ω_x	0	0.3431	-	0.4381	-
ω_y	-0.0647	-0.015	76.76	0.0738	214.11
ω_z	0	-0.3997	-	0.1235	-
ϕ	133.50	312.57	133.82	55.92	58.17
θ	136.94	97.30	28.98	59.35	56.68
ψ	155.27	9.40	93.96	20.10	87.07

Table A.28: MS - S1 - Percentage error on attitude variables: earth-pointing (materials)

Surface	SO	MO
+X	3.32	1.50
+Y	75.59	32.96
+Z	81.92	56.31
-X	68.45	57.67
-Y	61.13	84.95
-Z	99.98	98.33
Sun	58.41	11.77
Anti-sun	83.91	84.29

Table A.29: MS - S1 - Percentage error on emissivity: earth-pointing (materials)

	SO	MO
Attitude	5.6958	0.0384
Materials	152.8957	0.0232

Table A.30: MS - S1 - MSE earth-pointing

Sun-pointing Curves: attitude estimation

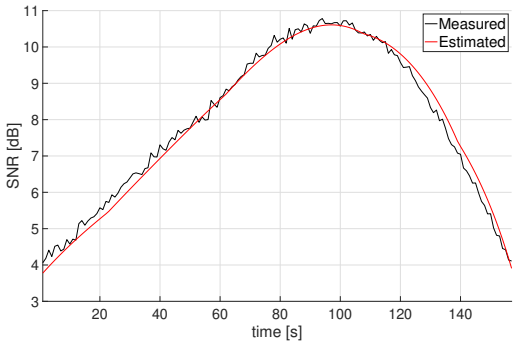

(a) SO: Observatory 1

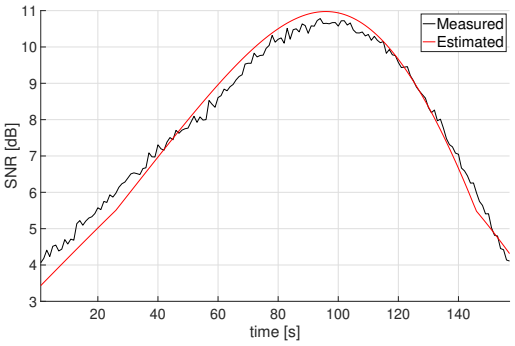

(b) MO: Observatory 1

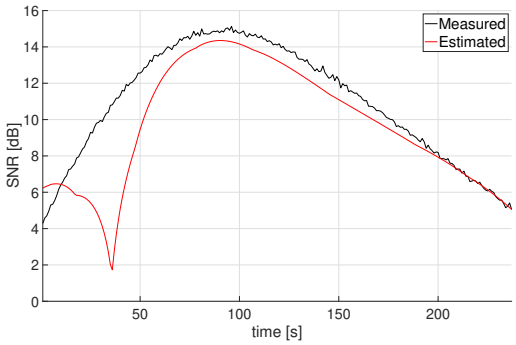

(c) SO: Observatory 2

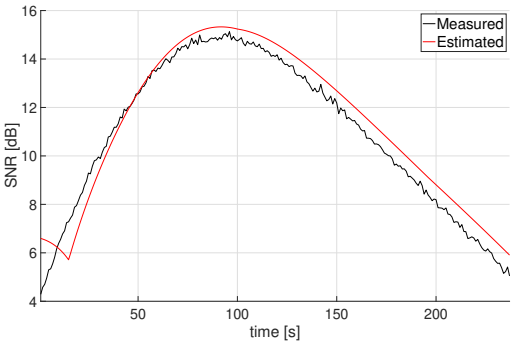

(d) MO: Observatory 2

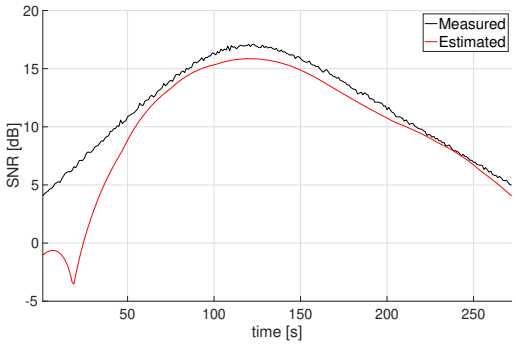

(e) SO: Observatory 3

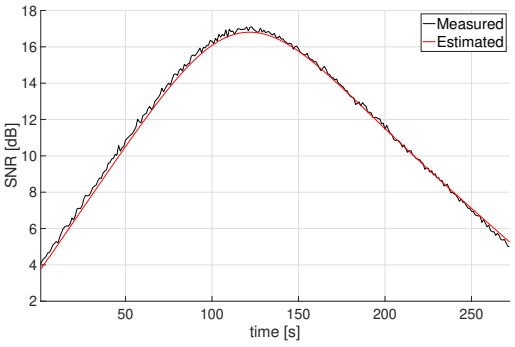

(f) MO: Observatory 3

Figure A.13: Comparison SO - MO with MultiStart: sun-pointing

Variable	True	Estimate SO	Err% SO	Estimate MO	Err% MO
ω_x	0	0.0562	-	-0.0669	78.07
ω_y	0	0.4733	-	0.0453	9.04
ω_z	0	0.3084	-	-0.0547	135.10
ϕ	317.93	119.17	62.51	307.90	3.16
θ	107.84	152.54	41.45	90.97	15.64
ψ	42.07	0.91	97.83	39.92	12.27

Table A.31: MS - S1 - Percentage error on attitude variables: sun-pointing

Sun-pointing Curves: attitude and material estimation

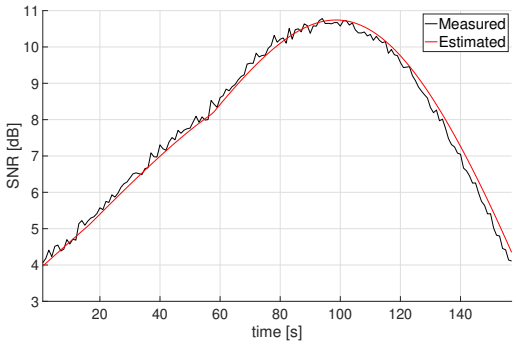

(a) SO: Observatory 1

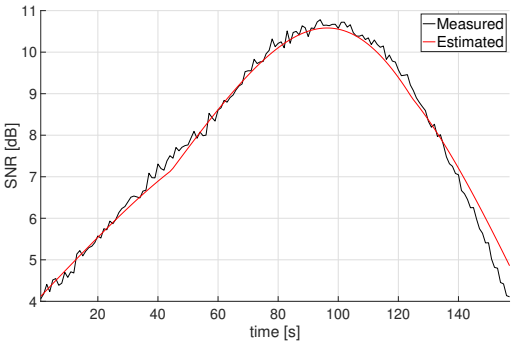

(b) MO: Observatory 1

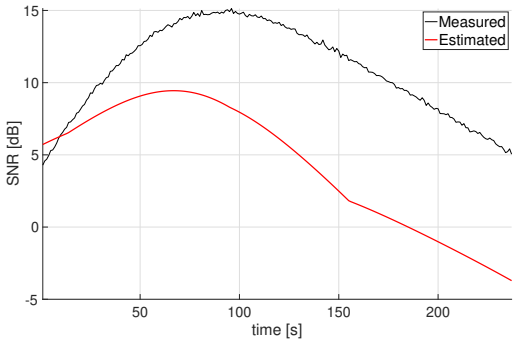

(c) SO: Observatory 2

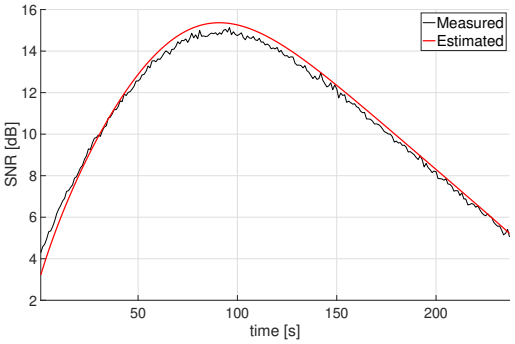

(d) MO: Observatory 2

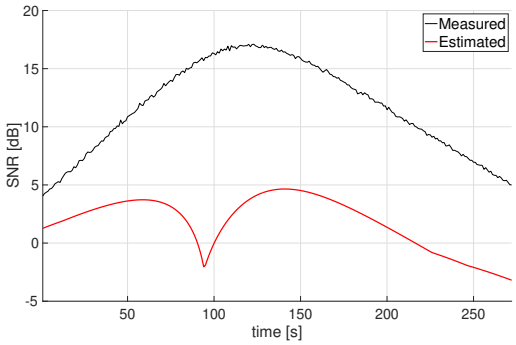

(e) SO: Observatory 3

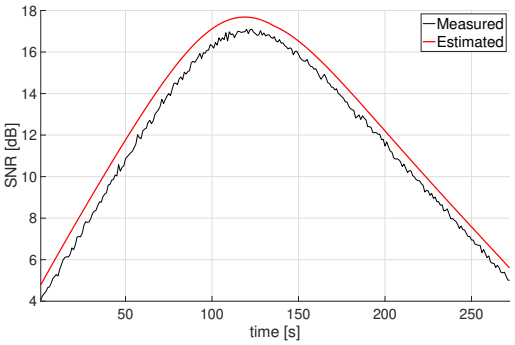

(f) MO: Observatory 3

Figure A.14: Comparison SO - MO with MultiStart: sun-pointing (materials)

Variable	True	Estimate SO	Err% SO	Estimate MO	Err% MO
ω_x	0	-0.0191	-	0.0524	-
ω_y	0	-0.1342	-	0.0329	-
ω_z	0	-0.0731	-	-0.0376	-
ϕ	330.75	56.49	82.23	44.40	86.03
θ	82.31	35.14	67.41	25.12	76.70
ψ	302.99	2.16	94.88	35.55	15.50

Table A.32: MS - S1 - Percentage error on attitude variables: sun-pointing (materials)

Surface	SO	MO
+X	99.22	13.85
+Y	6.73	27.67
+Z	19.46	19.57
-X	26.37	5.21
-Y	82.31	3.46
-Z	35.98	9.83
Sun	84.70	48.11
Anti-sun	87.57	4.17

Table A.33: MS - S1 - Percentage error on emissivity: sun-pointing (materials)

	SO	MO
Attitude	29.983	0.132
Materials	106.026	0.034

Table A.34: MS - S1 - MSE sun-pointing

Tumbling Motion Curves: attitude estimation

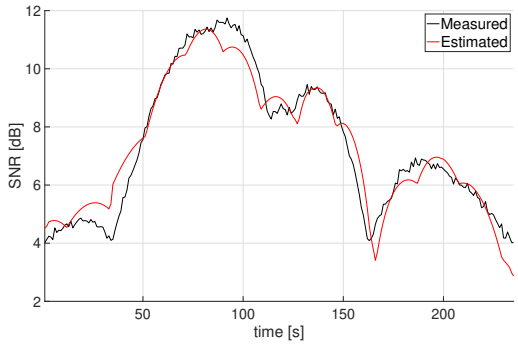

(a) SO: Observatory 1

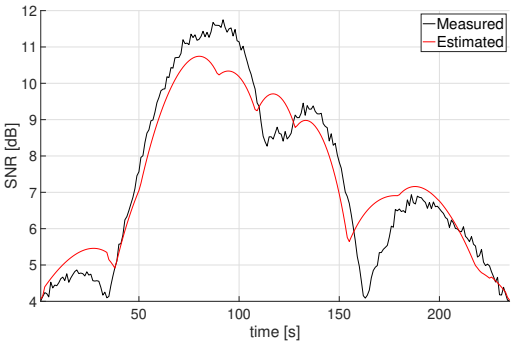

(b) MO: Observatory 1

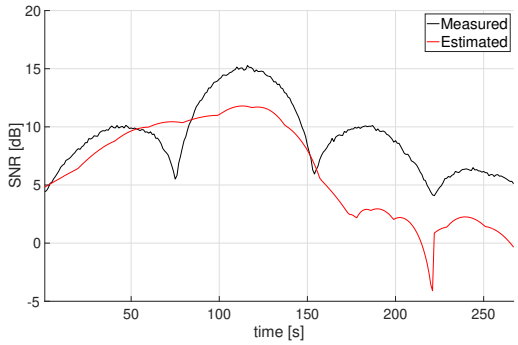

(c) SO: Observatory 2

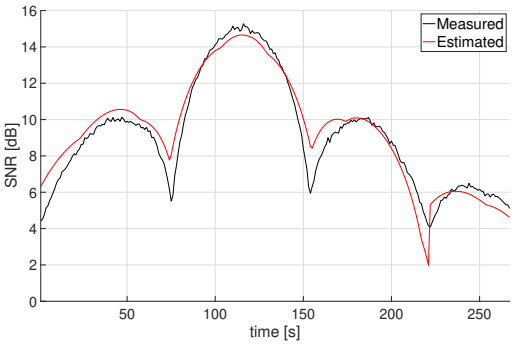

(d) MO: Observatory 2

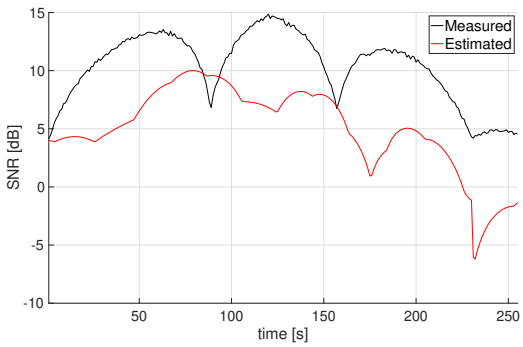

(e) SO: Observatory 3

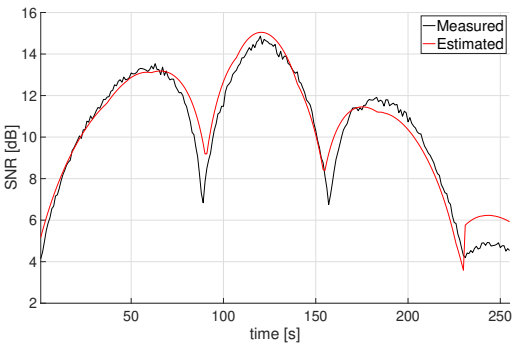

(f) MO: Observatory 3

Figure A.15: Comparison SO - MO with MultiStart: tumbling motion

Variable	True	Estimate SO	Err% SO	Estimate MO	Err% MO
ω_x	1	-0.195	119.48	$\sim$0	0.33
ω_y	1	0.311	68.87	-0.0573	43.67
ω_z	1	3.89	289.04	$\sim$0	229.58
ϕ	330.75	290.30	12.23	327.34	1.03
θ	82.31	55.62	32.42	80.45	2.26
ψ	302.99	229.15	24.37	95.99	68.32

Table A.35: MS - S1 - Percentage error on attitude variables: tumbling motion

Tumbling Motion Curves: attitude and material estimation

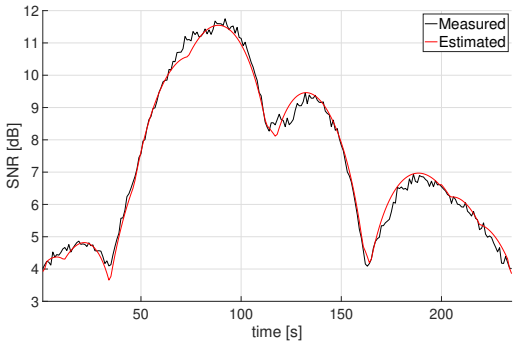

(a) SO: Observatory 1

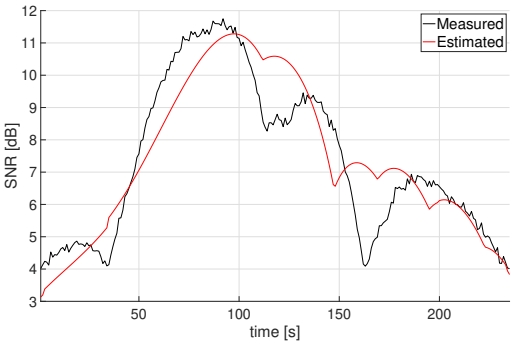

(b) MO: Observatory 1

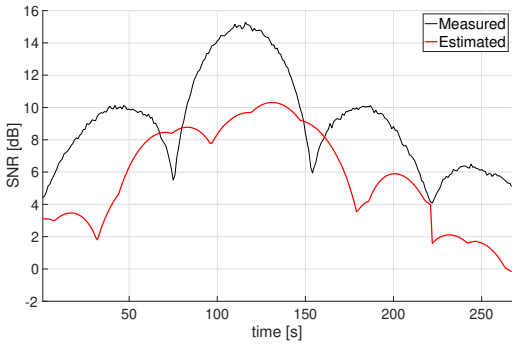

(c) SO: Observatory 2

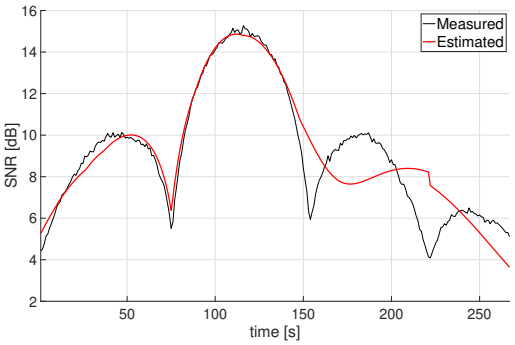

(d) MO: Observatory 2

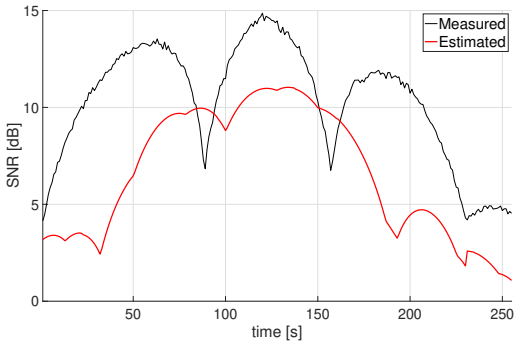

(e) SO: Observatory 3

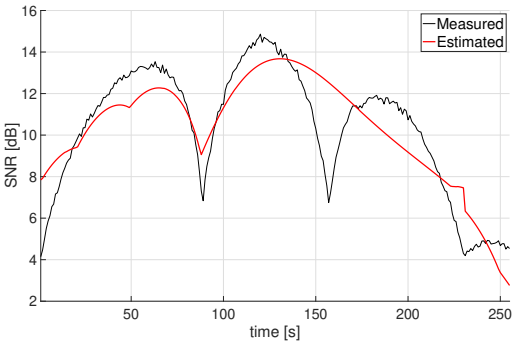

(f) MO: Observatory 3

Figure A.16: Comparison SO - MO with MultiStart: tumbling motion (materials)

Variable	True	Estimate SO	Err% SO	Estimate MO	Err% MO
ω_x	1	-1.36	236.00	1.78	78.07
ω_y	1	-0.96	196.47	1.09	9.04
ω_z	1	1.54	54.34	2.35	135.10
ϕ	330.75	339.59	2.67	220.6	33.30
θ	82.31	57.57	30.05	87.70	6.54
ψ	302.99	332.78	9.83	130.87	56.81

Table A.36: MS - S1 - Percentage error on attitude variables: tumbling motion (materials)

Surface	SO	MO
+X	30.18	17.83
+Y	14.94	43.34
+Z	57.19	55.56
-X	252.94	105.22
-Y	122.50	47.79
-Z	99.89	29.49
Sun	65.98	17.70
Anti-sun	36.97	15.82

Table A.37: MS - S1 - Percentage error on emissivity: tumbling motion (materials)

	SO	MO
Attitude	16.639	0.873
Materials	157.042	1.616

Table A.38: MS - S1 - MSE tumbling motion

A.2.2. Strategy 2: Multiple Instruments

Earth-pointing Curves: attitude estimation

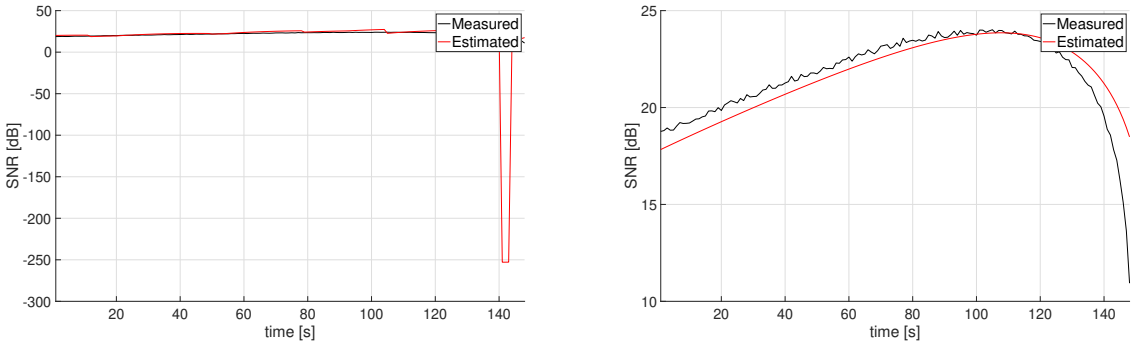

(a) SI: Sys1

(b) MI: Sys1

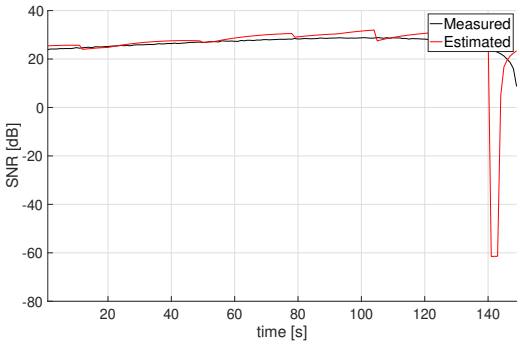

(c) SI: Sys2

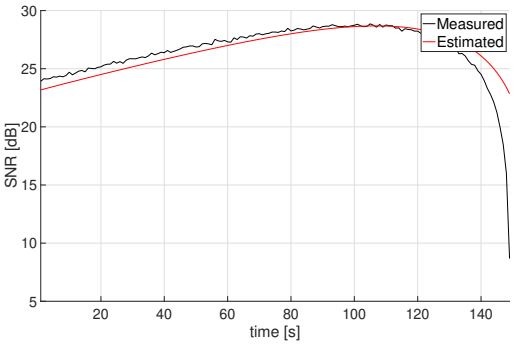

(d) MI: Sys2

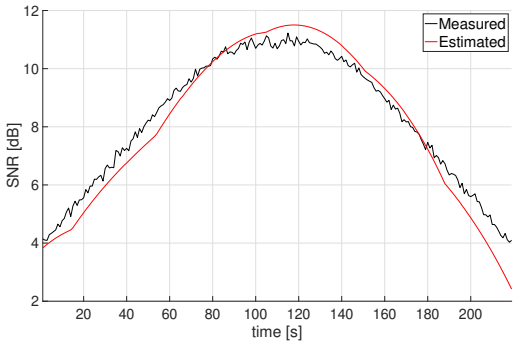

(e) SI: Sys3

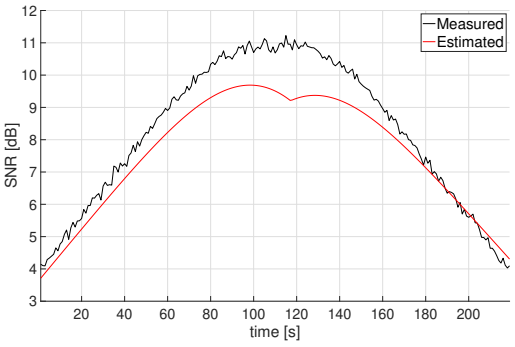

(f) MI: Sys3

Figure A.17: Comparison SI - MI with MultiStart: earth-pointing

Variable	True	Estimate SI	Err% SI	Estimate MI	Err% MI
ω_x	0	-0.3955	-	0.0027	-
ω_y	-0.0647	-0.1142	76.76	-0.0854	31.99
ω_z	0	-2.7506	-	0.0238	-
ϕ	216.25	351.31	62.45	193.79	10.38
θ	128.72	133.73	3.89	43.95	65.86
ψ	217.32	171.84	20.93	41.06	81.11

Table A.39: MS - S2 - Percentage error on attitude variables: earth-pointing

Earth-pointing Curves: attitude and material estimation

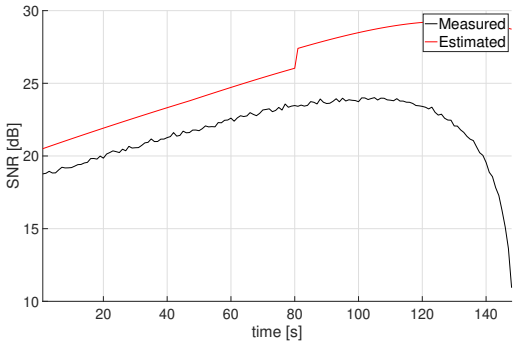

(a) SI: Sys1

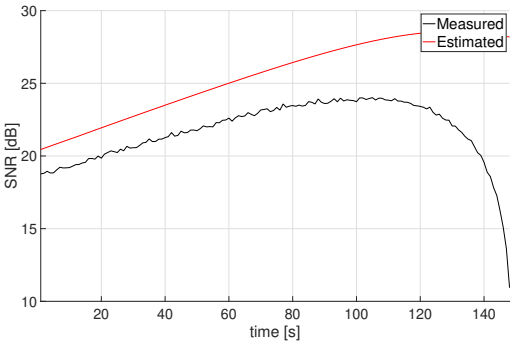

(b) MI: Sys1

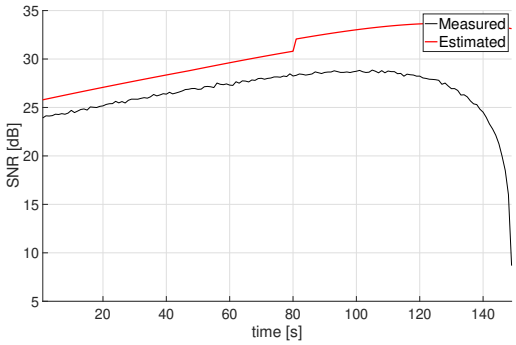

(c) SI: Sys2

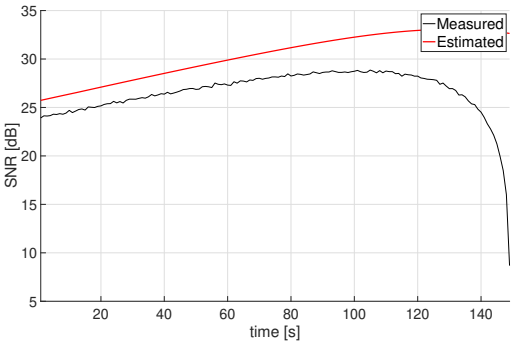

(d) MI: Sys2

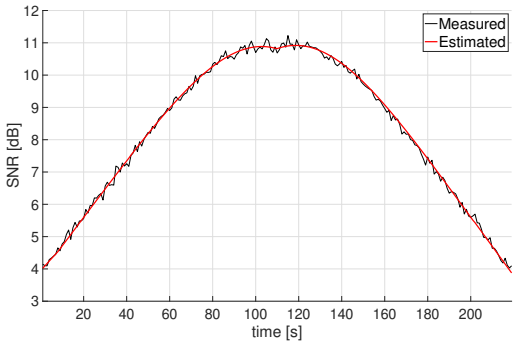

(e) SI: Sys3

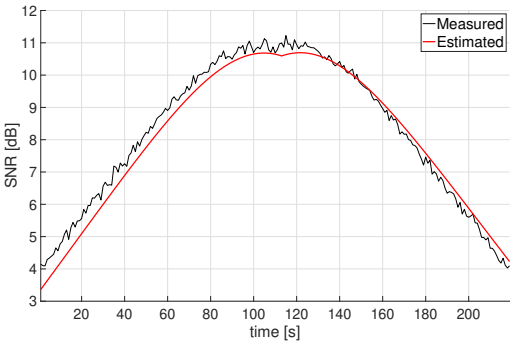

(f) MI: Sys3

Figure A.18: Comparison SI - MI with MultiStart: earth-pointing (materials)

Variable	True	Estimate SI	Err% SI	Estimate MI	Err% MI
ω_x	0	0.0773	-	0.0528	-
ω_y	-0.0647	-0.0801	23.97	-0.0558	13.71
ω_z	0	-0.0478	-	-0.0028	-
ϕ	133.50	24.53	88.65	43.28	79.99
θ	136.94	27.77	78.43	39.08	69.64
ψ	155.27	39.18	81.97	33.28	84.69

Table A.40: MS - S2 - Percentage error on attitude variables: earth-pointing (materials)

Surface	ε SI	ρ SI	ε MI	ρ MI
+X	46.28	55.88	21.66	48.82
+Y	3.98	4.96	11.17	16.69
+Z	33.53	67.85	33.74	71.59
-X	89.09	38.64	82.08	32.52
-Y	44.03	4.95	28.80	3.41
-Z	27.07	1.97	49.46	12.90
Sun	49.79	15.90	52.65	1.97
Anti-sun	40.97	98.73	0.34	62.69

Table A.41: MS - S2 - Percentage error on emissivity: earth-pointing (materials)

	SO	MO
Attitude	1473.995	1348.979
Materials	3871.706	939.443

Table A.42: MS - S2 - MSE earth-pointing

Sun-pointing Curves: attitude estimation

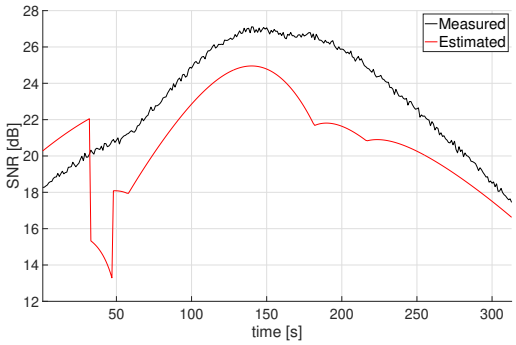

(a) SI: Sys1

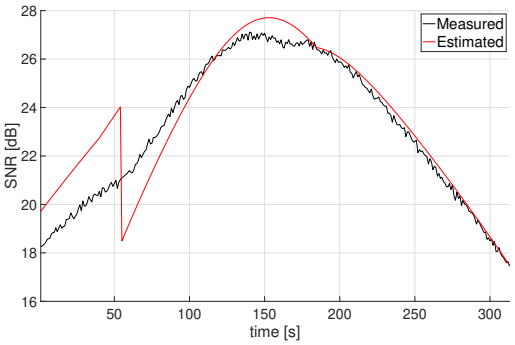

(b) MI: Sys1

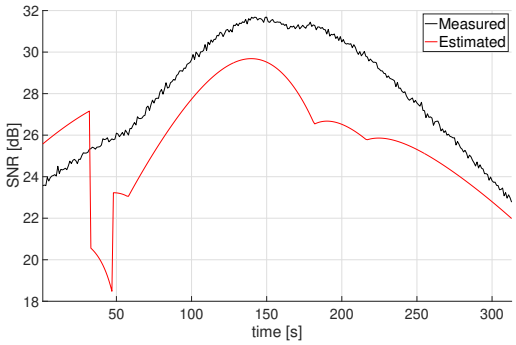

(c) SI: Sys2

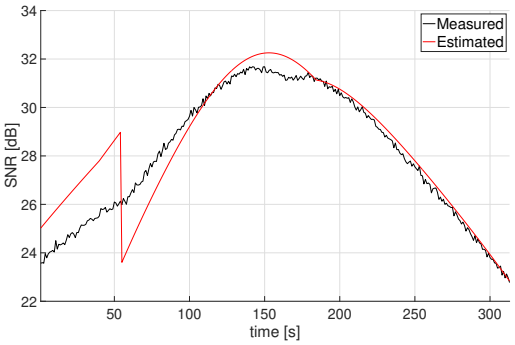

(d) MI: Sys2

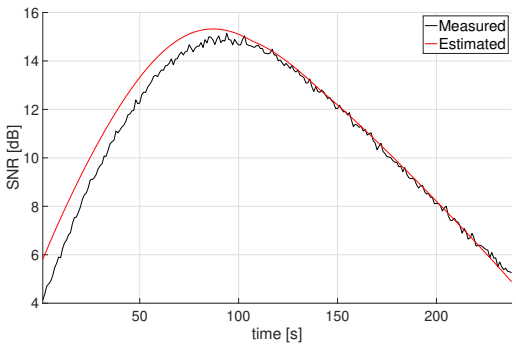

(e) SI: Sys3

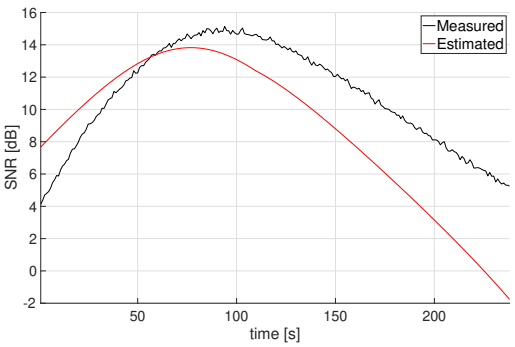

(f) MI: Sys3

Figure A.19: Comparison SI - MI with MultiStart: sun-pointing

Variable	True	Estimate SI	Err% SI	Estimate MI	Err% MI
ω_x	0	-0.0078	-	-0.0086	-
ω_y	0	-0.0033	-	0.0105	-
ω_z	0	0.0008	-	0.0015	-
ϕ	317.93	326.74	2.77	8.67	97.27
θ	107.84	104.88	2.74	94.76	12.12
ψ	42.07	21.29	49.39	21.79	48.21

Table A.43: MS - S2 - Percentage error on attitude variables: sun-pointing

Sun-pointing Curves: attitude and material estimation

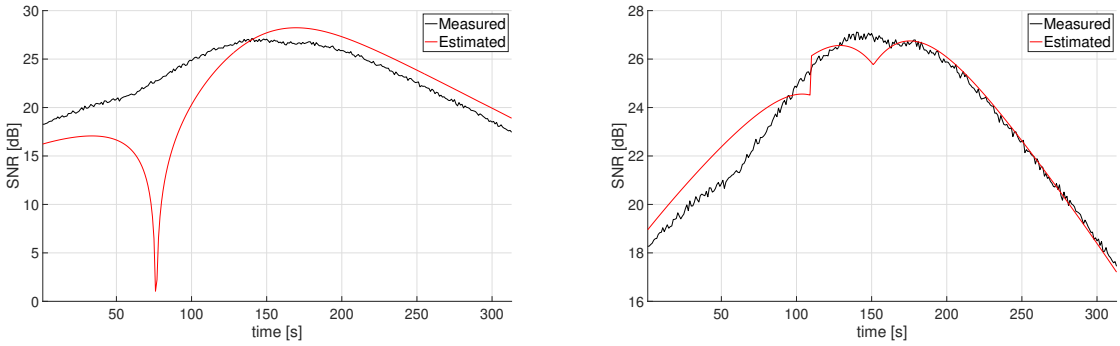

(a) SI: Sys1

(b) MI: Sys1

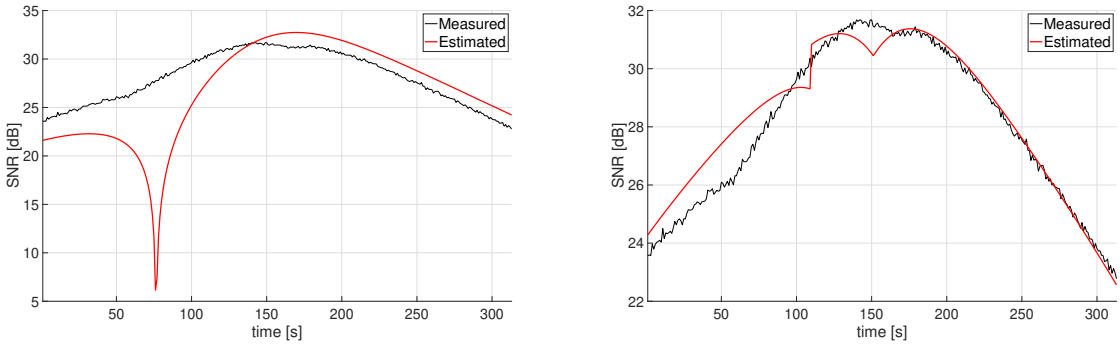

(c) SI: Sys2

(d) MI: Sys2

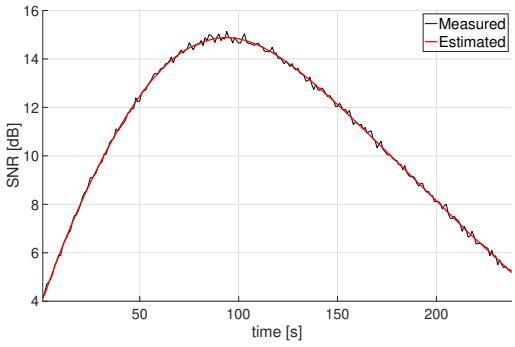

(e) SI: Sys3

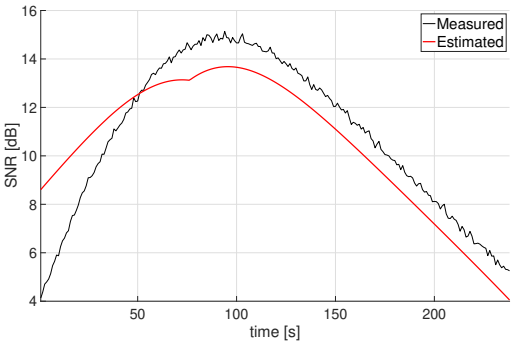

(f) MI: Sys3

Figure A.20: Comparison SI - MI with MultiStart: sun-pointing (materials)

Variable	True	Estimate SI	Err% SI	Estimate MI	Err% MI
ω_x	0	0.0013	-	-0.0106	-
ω_y	0	0.0084	-	-0.0670	-
ω_z	0	-0.0017	-	0.0205	-
ϕ	317.93	246.31	22.53	301.50	5.17
θ	107.84	94.88	12.02	61.08	43.36
ψ	42.07	108.32	157.47	23.94	43.11

Table A.44: MS - S2 - Percentage error on attitude variables: sun-pointing (materials)

Surface	ε SI	ρ SI	ε MI	ρ MI
+X	64.48	73.00	3.74	72.72
+Y	98.89	14.38	43.65	33.07
+Z	24.91	30.14	12.04	43.07
-X	64.95	37.09	9.02	19.63
-Y	99.07	8.87	43.19	18.09
-Z	25.25	20.85	88.19	31.80
Sun	99.79	17.28	59.19	64.31
Anti-sun	33.65	32.19	21.99	57.57

Table A.45: MS - S2 - Percentage error on emissivity: sun-pointing (materials)

	SO	MO
Attitude	6.052	4.044
Materials	12.043	0.867

Table A.46: MS - S2 - MSE sun-pointing

Tumbling Motion Curves: attitude estimation

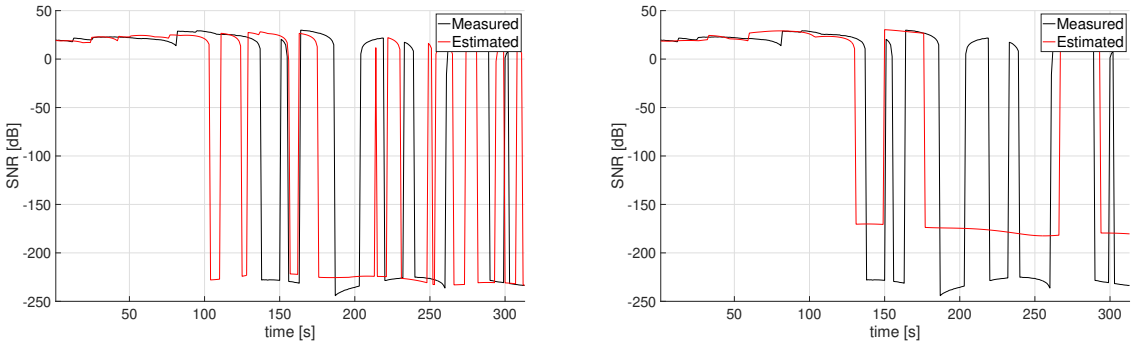

(a) SI: Sys1

(b) MI: Sys1

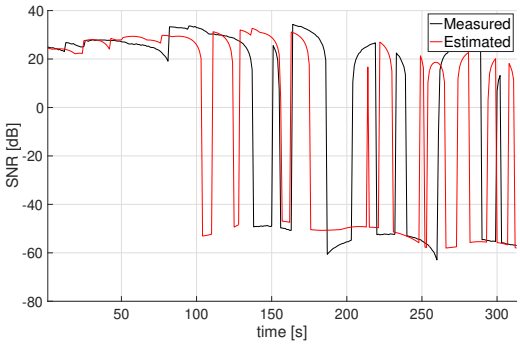

(c) SI: Sys2

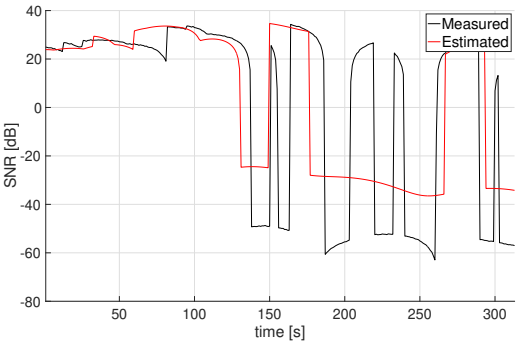

(d) MI: Sys2

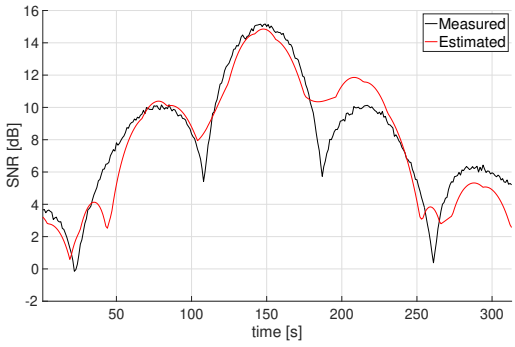

(e) SI: Sys3

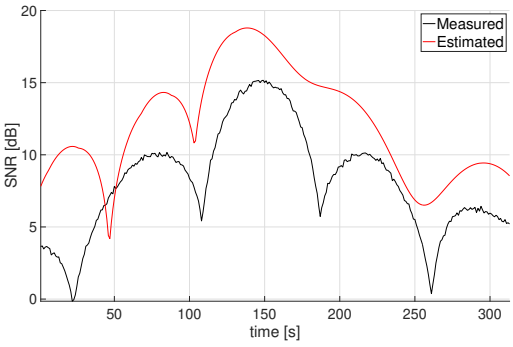

(f) MI: Sys3

Figure A.21: Comparison SI - MI with MultiStart: tumbling motion

Variable	True	Estimate SI	Err% SI	Estimate MI	Err% MI
ω_x	1	1.322	32.23	1.972	97.23
ω_y	1	0.724	27.62	-1.993	299.32
ω_z	1	-3.925	492.52	1.257	25.72
ϕ	330.75	191.83	42.00	180.34	45.58
θ	82.31	54.73	33.51	42.15	48.80
ψ	302.99	339.65	12.10	222.77	26.48

Table A.47: MS - S2 - Percentage error on attitude variables: tumbling motion

Tumbling Motion Curves: attitude and material estimation

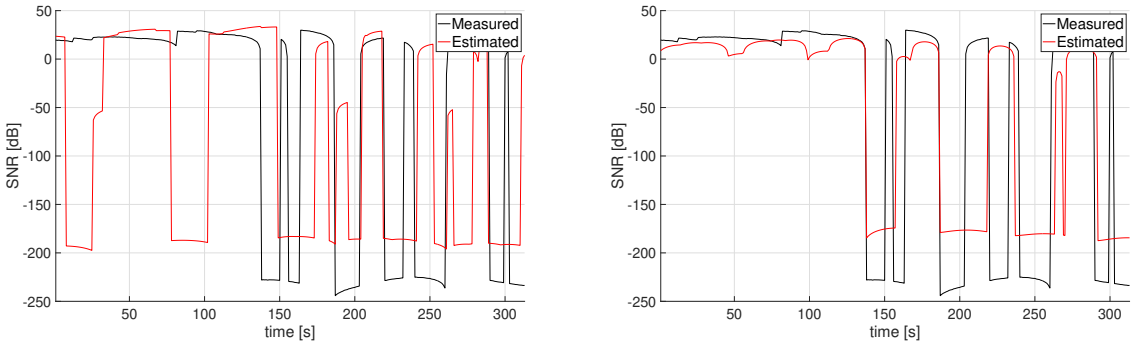

(a) SI: Sys1

(b) MI: Sys1

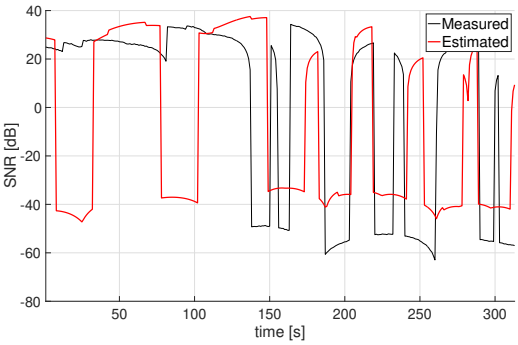

(c) SI: Sys2

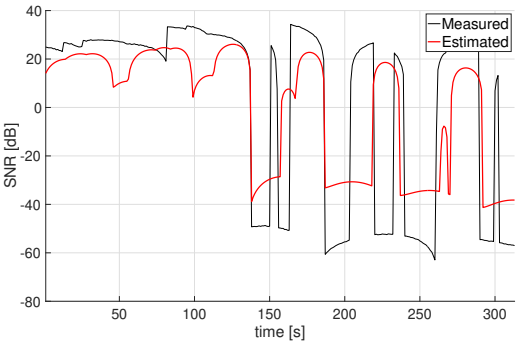

(d) MI: Sys2

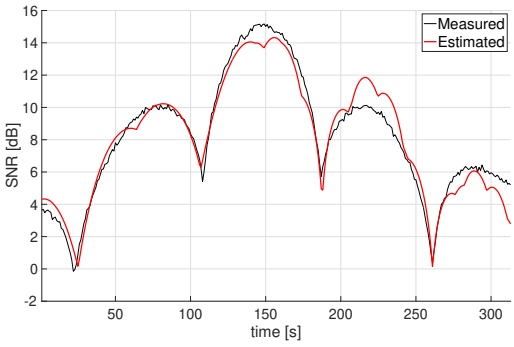

(e) SI: Sys3

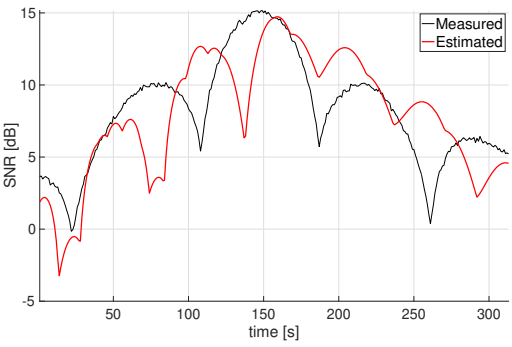

(f) MI: Sys3

Figure A.22: Comparison SI - MI with MultiStart: tumbling motion (materials)

Variable	True	Estimate SI	Err% SI	Estimate MI	Err% MI
ω_x	1	0.029	97.05	1.529	52.88
ω_y	1	3.636	263.62	4.958	395.77
ω_z	1	-3.629	462.87	-3.358	435.77
ϕ	330.75	211.51	36.05	97.12	70.64
θ	82.31	157.54	91.39	122.18	48.43
ψ	302.99	1.412	99.53	161.42	46.72

Table A.48: MS - S2 - Percentage error on attitude variables: tumbling motion (materials)

Surface	ε SI	ε MI	ρ SI	ρ MI
+X	16.91	99.99	26.53	69.80
+Y	38.19	99.98	88.30	51.42
+Z	39.13	92.86	83.36	90.65
-X	152.29	99.99	52.22	69.86
-Y	73.62	61.65	55.49	45.80
-Z	80.51	50.99	91.72	19.56
Sun	95.17	99.67	75.14	10.55
Anti-sun	13.83	79.47	77.07	61.52

Table A.49: MS - S2 - Percentage error on emissivity: tumbling motion (materials)

	SO	MO
Attitude	7616.737	3392.025
Materials	6967.476	2961.873

Table A.50: MS - S2 - MSE tumbling motion

List of Figures

List of Tables

Acknowledgements

Vorrei ringraziare il mio relatore, Prof. Pierluigi Di Lizia, per la disponibilità, la professionalità e soprattutto il sostegno che mi ha fornito in questi mesi. Nonostante il lavoro sia stato svolto esternamente al Politecnico e i presupposti non fossero i migliori, lei mi ha rassicurato fin dall'inizio e alla fine mi ha aiutato a concludere al meglio questo lavoro.

Un altro sentito ringraziamento va al Prof. Mauro Massari, che mi ha permesso di affrontare al meglio gli argomenti trattati in questo lavoro che non erano perfettamente in linea con le mie conoscenze maturate negli ultimi anni di studi. Le sue correzioni e i suoi suggerimenti mi hanno consentito di consolidare il lavoro svolto.

Je tiens à remercier Javier Carro et Ivan Llamas de m'avoir donné l'occasion d'effectuer mon stage de fin d'études chez GMV sous leur supervision. À GMV, j'ai trouvé un environnement stimulant et accueillant, comme dans une grande famille. Merci à William, David, Mafer et Laura pour la compagnie pendant les jours passés au bureau.

Grazie al Prof. Roberto Armellin e Laura Pirovano per avermi guidato passo dopo passo, con pazienza e gentilezza, nello sviluppo di un progetto che è stato fondamentale per la mia crescita professionale e che mi ha fornito le basi per condurre questo lavoro di tesi.

Grazie alla mia famiglia, un sostegno unico e non scontato per cui sarò sempre grato. Grazie a mamma e papi, per le infinite possibilità che mi avete regalato, per essere stati sempre al mio fianco nonostante la distanza e per tutti i valori e gli insegnamenti che continuate a trasmettermi. Grazie a mio fratello, per essere il mio punto di riferimento ogni volta che ne ho bisogno, per la pazienza e la dolcezza che mi riservi ogni volta che ti prendi cura di me. Grazie ai miei zii, Piero e Marcello, per avermi donato il vostro amore e il vostro tempo per aiutarmi ad affrontare qualunque situazione si presentasse.

Grazie ai miei amici per gli infiniti momenti di felicità che mi avete fatto vivere, per farmi capire che il rapporto che abbiamo è ciò che più conta nella vita e per quei piccoli grandi particolari che ci rendono simili, che mi fanno percepire una connessione vera e sincera e che mi fanno capire di non essere da solo. Grazie per i momenti in cui abbiamo condiviso soddisfazioni, insicurezze e riflessioni che mi hanno fatto crescere e capire tanto. Grazie

per avermi sempre permesso di ascoltarvi ed essere ascoltato. Grazie per insultarmi, per dirmi la verità e prendermi a schiaffi. Grazie per farmi ridere, sognare e accompagnarmi in ogni momento.

Grazie ai miei fratielli Ciccio, Giampaolo e Corrado, a Noemi, Marta, Aurora e Federica, a Giovanni e Vittorio, a Ciccio, Giorgio, Claudia, Salvo, Antonio, Silvia e Ludovica, a Sergio, Tommaso, Franco, Nino, Andrea e Simone, a Vincenzo, Fabrizio, Andrea e Federico, a Mario ed Enrico, a Giuse, Fra, Gio, Michi, Tizi, Barilla, Emi, Lore, Barte, Luca e Ale, ad Antonio, a Gaia, Daniele, Alice, Enzo, Marzio e Salvo, a Riccardo, Billal, Antonio, Nicola, Emanuele, Matteo, Michele e Thea.